VILNIUS UNIVERSITY

CENTER FOR PHYSICAL SCIENCES AND TECHNOLOGY

LINA PAVASARYTĖ

INVESTIGATION OF LUMINESCENT AND STRUCTURAL PROPERTIES OF LANTHANIDE ALUMINIUM GARNETS SYNTHESIZED BY SOL-GEL METHOD

Doctoral dissertation

Physical Sciences, Chemistry (03 P)

Vilnius, 2018

The dissertation was carried out from 2013 to 2017 at Vilnius University.

Scientific supervisors:

Prof. Dr. Aldona Beganskienė (Vilnius University, Physical Sciences, Chemistry - 03 P). (From 2013-10-01 to 2016-10-03)

Prof. Habil. Dr. Aivaras Kareiva (Vilnius University, Physical Sciences, Chemistry - 03 P). (From 2016-10-01 to 2017-09-30)

CONTENTS

LIST OF ABBREVIATIONS

YAG - Ytrium aluminium garnet

CRT - Cathode ray tubes

FEDs - Field-emission displays

PDPs - Plasma display panels

NIR - Near infrared

YAG:Nd - Nd^{3+} doped ytrium aluminium garnet

YAG:Sm,Eu - Sm^{3+} and Eu^{3+} co-doped ytrium aluminium garnet

CN - Coordination number

RE - Rare earth element

YAG:Yb - Yb^{3+} doped yttrium aluminium garnet

YGG - Yttrium gallium garnet

YIG - Yttrium iron garnet

AHC - Ammonium hydrogen carbonate

TEOS - Tetraethoxysilane

LuAG:Nd - Nd^{3+} doped lutetium aluminium garnet

LuAG - lutetium aluminium garnet

HIP - Hot isostatic pressing

SP - Spray pyrolysis

YAG:Ce - Ce^{3+} doped yttrium aluminium garnet

CP-LTSP - Co-precipitation and low temperature spray pyrolysis

LCS - Low temperature combustion synthesis

Cz - Czochralski method

ICF - Inertial confinement fusion

UV - Ultraviolet

IR - Infrared

YAG:Ce,Eu - Ce^{3+} and Eu^{3+} co-doped yttrium aluminium garnet

LEDs - Light-emitting diodes

EDTA - Ethylenediamine-tetraacetic acid

XRD - X-ray diffraction

FTIR - Fourier transform infrared

SEM - Scanning electron microscopy

TEM - Transmission electron microscopy

NMR - Nuclear magnetic resonance

^{27}Al MAS - Magic-Angle Spinning

INTRODUCTION

$Y_3Al_5O_{12}$ is commonly called yttrium aluminium garnet (YAG) adopts the cubic garnet structure[1] and doped with a transition metal or lanthanide ions is an important solid-state laser material widely used in luminescence systems, window materials for a variety of light sources. Rare earth (RE) doped YAG has been thoroughly investigated for application in various fields, such as lasers, scintillators, cathode ray tubes (CRT), field-emission displays (FEDs), plasma display panels (PDPs,) and optical windows, due to its attractive optical properties, outstanding chemical stability, low creep rate and high thermal resistance[2,3,4,5,6]. Luminescent materials based on YAG are stable under conditions of high irradiation with an electron beam[7,8].

The phosphors host materials have proven to be of great importance for the optical function. The matrix should possess good chemical, mechanical, thermal and optical characteristics. It is well known that physical properties of crystalline materials are very dependent on the host material, phase purity, distribution of the grains size and crystalline homogeneity[9,10,11]. For example, transition metal and rare-earth element ions have demonstrated lasing action in a wide variety of host crystals. Among the compounds which can incorporate transition metals or lanthanides several scandium and gallium based materials were elaborated[12,13,14,15,16,17,18,19.] In the YAG all aluminium ions may be substituted by gallium or iron ions, while pure yttrium indium or yttrium scandium garnet is not obtained. Besides, rare-earth aluminium garnets have also attracted considerable attention as host crystals for near-infrared solid-state lasers as well as for optoelectronics devices, including computer memories, microwave optical elements and as laser active media with applications in medical surgery, optical communications and coherent laser radar[20,21,22].

In rare earth containing compounds, fluorescence efficiency is the most important and significant parameter for their optical applications. In single rare earth ion doped systems, the fluorescence efficiency increases with increasing the dopant concentration. At particular concentration the emission intensity might be decreased due to the concentration quenching effect. However, by co-doping with another suitable rare earth ion the fluorescence efficiency of the single rare earth ion doped matrix could be significantly enhanced by the energy transfer process. In co-doped materials, energy transfer from one ion (sensitizer) to another ion (activator) may occur. Such energy transfer processes have been attracting a significant attention for its practical utility in optical devices. Possible energy transfer among rare earth combinations in various materials have been reported earlier, especially $Ce^{3+} \rightarrow Tb^{3+}$, $Dy^{3+} \rightarrow Sm^{3+}$, $Tb^{3+} \rightarrow Sm^{3+}$, $Sm^{3+} \rightarrow Eu^{3+}$ and $Tb^{3+} \rightarrow Eu^{3+}$. To increase the emission performance of activator ions, generally the concentration of the sensitizer ions is increased. At higher concentration of sensitizer the quenching effect will not be observed, however, the ionic aggregation will be observed, and these aggregates act as quenching centers[23,24,25]

The motivation of this work was to synthesize new mixed-metal garnets by sol-gel method and to study the substitution effects on their structural properties. The investigation of the luminescence properties of new doped garnet crystal structure compounds was also in the field of interest. Finally, the research was focused on the correlation between the structure and the luminescence properties of europium- and samarium-doped garnets which are the potential candidates for the NIR laser or optical imaging applications. The following tasks were set in order to achieve these objectives:

- to prepare $Tb_3Al_5O_{12}$:Eu, $Dy_3Al_5O_{12}$:Eu, $Ho_3Al_5O_{12}$:Eu, $Er_3Al_5O_{12}:Eu^{3+}$, $Tm_3Al_5O_{12}$:Eu, $Yb_3Al_5O_{12}$:Eu and $Lu_3Al_5O_{12}$:Eu garnets using sol-gel technique and investigate the luminescent properties of these Eu^{3+}-doped compounds;
- to synthesize and characterize the $Ho_3Al_5O_{12}$:Eu by solvothermal method at low temperature;
- to prepare YAG samples co-doped with different amount of Nd^{3+} and YAG:Nd garnets with various doping levels of europium by sol-gel method and investigate their structural and luminescence properties;

- to prepare YAG samples doped with different amount of Sm^{3+} and YAG:Sm garnets with various doping levels of europium by sol-gel method and investigate their structural and luminescence properties.

1. LITERATURE OVERVIEW

1.1. Characterisation of Metal Oxide Garnets

1.1.1. Structural features

Natural garnet is the common name of minerals belonging to the orthosilicate group, which contain isolated $[SiO_4]^{4-}$ ions, and formula can be written as $C_3A_2[SiO_4]_3$. The general chemical formula of garnets is $C_3A_2Si_3O_{12}$. The garnet group is divided into two series comprising the six more common terms: pyralspite, where A = Al^{3+} and C = Mg^{2+}, Fe^{2+}, Mn^{2+} (pyrope $Mg_3Al_2Si_3O_{12}$, almandine $Fe_3Al_2Si_3O_{12}$, spessartine $Mn_3Al_2Si_3O_{12}$) and ugrandite, where C = Ca^{2+} and A = Cr^{3+}, Al^{3+}, Fe^{3+} (uvarovite $Ca_3Cr_2Si_3O_{12}$, grossular $Ca_3Al_2Si_3O_{12}$, andradite $Ca_3Fe_2Si_3O_{12}$)[26] (see Table 1).

Table 1. Samples of the natural garnets.

Sample			C_3 dodekahedral	A_2 oktahedral	D_3 tetrahedral	O
Natural garnets	pyralspite	Pyrope	Mg_3^{2+}	Al_2^{3+}	Si_3^{4+}	O_{12}
		Almandine	Fe_3^{2+}	Al_2^{3+}	Si_3^{4+}	O_{12}
		Spessartine	Mn_3^{2+}	Al_2^{3+}	Si_3^{4+}	O_{12}
	ugrandite	Uvarovite	Ca_3^{2+}	Cr_2^{3+}	Si_3^{4+}	O_{12}
		Grossular	Ca_3^{2+}	Al_2^{3+}	Si_3^{4+}	O_{12}
		Andradite	Ca_3^{2+}	Fe_2^{3+}	Si_3^{4+}	O_{12}

Hundreds of works have been published since ytrium-aluminium garnet (YAG) was prepared for the first time by Yoder and Keith in 1951[27], and particularly after discovery by D. Jusis in 1964 of garnet with neodymium addition. The high refractive index, hardness, good polishing capacity, have given rise to extensive propagation of YAG as one of the synthetic replacements for diamond. Use of YAG crystals, activated by some elements, in a series of branches of electronic technology, for example in solid-state lasers, is promising[28].

Garnets crystallize in the most symmetric space group, Ia3-d, of the cubic crystal system. In the garnet structure C denotes a large ion located at dodecahedral sites (coordination number (CN) = 8), A stands for a medium size ion at octahedral sites (CN = 6), and D denotes a relatively small ion located at tetrahedral sites (CN = 4; see Fig. 1)[26,29].

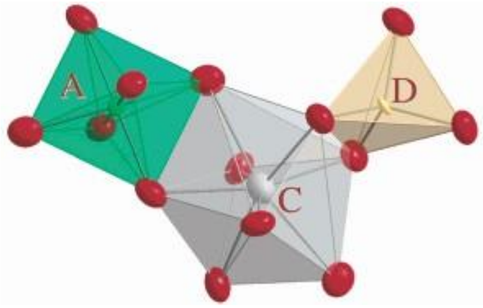

Fig. 1. Coordination polyhedra in the garnet structure presented as threedimensional atomic displacement ellipsoids of ions in YAG:Yb crystal at 295 K.

Since the lattice parameters of yttria and rare-earth oxides are very close, because of similar ionic radii, an important question that arises is if the mixed oxide forms a solid solution or not. The formation of a solid solution could avoid the seggregation of elements during the sintering process. Also, it is important to know if the crystal structure of the YAG prepared using RE_2O_3 is similar to that produced using pure Y_2O_3, because since the discovery of stimulated emission in Nd-doped yttrium–aluminum garnet (YAG) crystal, the rare earth doped YAG crystals have been the most widely used solid-state laser materials[30].

YAG ceramics have many potential advantages, which have been described extensively in the literature[31]. Since YAG is a stoichiometric crystal with very precise ratio Y/Al = 3/5, preparation of the YAG ceramics is quite difficult due to many factors, which can cause non-stoichiometry of the material through the preparation process. For this reason, many studies were aimed at finding the effect of Y/Al ratio variance on the phase composition and quality of the ceramics[32].

In the reference[33], the authors prepared completely transparent YAG ceramics from powders. The optical and mechanical properties of YAG ceramics are very sensitive to point defects. The authors report the effect of doping on oxygen diffusivity in several YAG ceramics, doped with various elements. Although Nd doping slightly increases the oxygen diffusion coefficient and the number of oxygen vacancies increases with increasing Nd concentration in as sintered materials, the variation of the oxygen diffusion coefficient in well annealed samples is small.

Eu^{3+}, Tb^{3+} and Ce^{3+} ions are known to emit visible radiation in the red, green and blue regions. They are also interesting due to their homogeneous incorporation only into one site (D_{2h} symmetry) of the YAG lattice. It decreases the energy transfers among dopants occurring in multi-site hosts and causing non-radiative transitions and decrease of the luminescence efficiency. It leads also to improving physical and chemical properties of the material such as temperature characteristics, resistance to brightness saturation and matrices resistance to high intensity electron beams[34].

1.1.2. Synthesis routes for garnets

Many different synthesis methods for the garnets are described in the literature. The solid-state reaction route is a widely used method for the preparation of powders from a mixture of the starting oxides or carbonates. Various wet-chemical methods, which include combustion, co-precipitation, hydrothermal, spray pyrolysis, sol-gel, solvothermal and emulsion synthesis method have been developed and successfully used for a low-temperature production of phase-pure YAG, yttrium gallium garnet (YGG), yttrium iron garnet (YIG) powders and related systems[5,35, 36, 37].

To achieve well fabricated YAG ceramics, it is important to prepare powdered material with well sintering property as a first step. The sinterability of a powders mostly depends on the particle size, shape, size distribution, chemical composition, degree of agglomeration and purity. These characteristics depend strongly on the method used to synthesize the powders. Some wet-chemical methods have been successfully used for the formation of pure YAG phase at lower temperatures compared to the solid-reaction method[38]. Usually, two source powders are utilized to make YAG transparent ceramics: (i) mixtures of Y_2O_3 and Al_2O_3, which form YAG in situ during solid-state reactive sintering[39,40,41] and (ii) wet-chemical synthesized YAG powders. Solid-state reactive sintering is a relatively simple way to fabricate YAG transparent ceramics and a range of compositions is easy to implement by changing the amount of reactant during batching[42,43]. However, the incorporation of some impurities is unavoidable during ball milling. Wet chemical approaches such as precipitation[31,44] spray pyrolysis[45,46], hydrothermal (or solvothermal) synthesis[47,48,49] sol–gel[18] and combustion synthesis[50,51] have many advantages such as atomic level mixing of high-purity precursors and low processing temperature. Among the wet chemical methods, precipitation is a relatively simple way to synthesize YAG powder with compositional homogeneity, good crystallinity and pure phase at low temperature. And fully dense and transparent ceramics can be fabricated by vacuum sintering of YAG powders with high sinterability. Jiang Li et. al.[52] have synthesyzed YAG using carbonate precursors via a co-precipitation method using ammonium hydrogen carbonate (AHC) as the precipitant. Nanosized YAG powders with high sinterability were obtained at 1200 °C and transparent YAG ceramics were fabricated by vacuum sintering at 1730–1790 °C with a considerable amount of additives of tetraethoxysilane (TEOS) and MgO.

The wet chemical methods are superior to physical methods and reactions in solid phase, because in water solution diffusion proceeds easily and homogeneity at the molecular level is achievable effortlessly. Each of wet methods allows obtaining homogenous and amorphous or nanocrystalline materials, and each of them can be disadvantageous. For eg. the cryochemical methods require expensive equipment, the co-precipitation methods are very sensitive to pH variations, and the sol-gel method is time consuming[53,54].

Loiko et al.[53] described that the precursors of the yttrium aluminum garnet can be obtained by three main ways. The first is based on a reaction in the solid phase and proceeds through sintering of the size-reduced and well-mixed yttrium oxide and aluminum oxide powders at 1750 ^{0}C. The other two methods are wet chemical methods that are based either on co-precipitation or sol-gel formation. In the co-precipitation method, the grains of the YAG are obtained by dissolution of water-soluble salts, which next are alkalized for the pH enables entire transformation of the metal ions to yttrium and aluminum hydroxides. After removing of the anions adsorbed at the surface of deposit, it was calcinated at 1000-1200 °C[53,55,56].

Hussain et al.[57], Wu et al.[58] and Yi et al.[59] also clasified well-known preparation methods of rare-earth doped phosphors into two main categories: solid-state reaction and wet-chemical method. For solid-state reaction, the rare earth doped oxide phosphor bulk ceramics can be prepared by calcining mixed oxides at high temperature and then grinding into microparticles to obtain more active emission sites. Generally, the crystallization degree of the phosphors synthesized by the solid-state reaction is high, which favors the luminescent properties. However, their luminescent properties are unsatisfactory due to the formation of large aggregated particles with limited surface area. Although these particles can be crushed by different methods, the size of the particles is still larger than phosphors synthesized by wet-chemical methods. In addition, the surface of crushed or milled phosphor particles is full of defects, which lower the fluorescent efficiency due to the surface quenching effect[60,61]. In contrast, nanostructured phosphors obtained through wet-chemical methods are favored to obtain high light efficiency because of their small size and large surface area. However, the low crystallization degree of wet-chemical synthesized nanoparticles normally results in particles with low luminescent properties due to the serious quenching effect caused by the surface and inside defect in the nanoparticles. Until now, the synthesis of nanosized phosphor particles with a high crystallization degree has been a challenge for the manufacturing of phosphors. In addition, the morphology of phosphor nanoparticles is also a very important factor to determine the phosphor properties[61].

LuAG:Nd ceramic is attractive because of its high thermal conductivity, suitable emission cross-section, long life time and easy to get large scale. To achieve high quality transparent polycrystalline LuAG, the synthesis of pure and well dispersed lutetium aluminum garnet (LuAG) powders is crucial and important. Co-precipitation method using AHC as the precipitant is a relatively simple way to synthesize powders with excellent dispersion and sintering properties[62,63,64]. In the co-precipitation process, parameters such as reaction temperature, dripping speed, aging time, pH value, species and dosage of precipitant, species and dosage of dispersant, etc., are very important. Because most of these parameters are all interdependent during the formation and evolution of the precursor, they need to be optimized carefully. However, the synthesis of LuAG powder using AHC as the precipitant is rarely studied in detail, especially for the influences of pH values, aging time, dropping speed, and the amount of solution[43,65]. Jiang Li et all[52] presented a wet-chemical synthesis route to produce nanosized YAG powders, employing $Al(NO_3)_3 \cdot 9H_2O$ and Y_2O_3 as the starting materials.

Zhand et. all[62] reported about Nd doped LuAG prepared by hot isostatic pressing (HIP). It is critical to eliminate all the remaining porosity in order to get a transparent ceramics with good quality[66,67]. Hot isostatic pressing is a very effective method in reaching full densification of ceramics. The driving force for densification is ~50 times greater during HIP than during normal sintering. Unfortunately, the obvious deterioration occurred in HIPed LuAG:Nd ceramics after annealing. However, annealing is one of the key steps in preparing laser ceramics[62,68,69]. It is reported about high quality LuAG:Nd laser ceramics produced using either vacuum sintering or vacuum sintering with additional HIP treatment. reference[62] demonstrates that it is possible to eliminate the remaining micro pores by HIP approach. The porosity of

LuAG:Nd laser ceramics sharply declined from $7 \cdot 10^{-6}$ to $5.6 \cdot 10^{-7}$ after additional HIP.

The spray pyrolysis (SP) method, which has been applied in the preparation of phosphor materials[70,71] is recommended as a promising method for preparing particles with spherical shape, narrow size distribution and agglomerate-free characteristic. Shenghia et al.[72] co-precipitation process at first introduced as spray suspension to take the place of spray solution. Agglomerate-free YAG:Ce phosphor particles were obtained via spray suspension under co-precipitation and low temperature spray pyrolysis (CP-LTSP). Thermal properties of as-prepared particles, effects of the doping concentration of Ce^{3+}, annealing temperature on morphology and the emission intensity of YAG:Ce phosphor particles were investigated[72]. The drawback is that high-heating rates and short residence time inherent to spray pyrolysis process lead to the formation of kinetically stable phases rather than the thermodynamically stable target YAG phase[73]. Since spray pyrolysis offers different approaches for controlling of the particle morphology and composition, Mancic et al.[71] obtained the YAG:Ce particles with spherical and filled morphology through introduction of polymeric precursor solutions.

The low temperature combustion synthesis (LCS), firstly used by Pechini in 1967 to synthesize capacitor ceramics, is one of the simplest methods for synthesizing ceramic nano-sized powders[74]. A very porous sponge-like compound is formed due to the release of a large amount of gaseous products formed in low temperature combustion reaction between metal nitrates used as oxidizer and citric acid used as chelating agent, reducer and fuel in the reactant system. The homogenous microscopy of ceramic can be obtained with good crystallization, so the transparency can be increased. In reference[75] the $(Nd_{0.01}Y_{0.99})_3Al_5O_{12}$ nanosized powders were produced by the LCS. The pure cubic YAG crystal phase was obtained at the temperature as low as 1100 °C.

Gel combustion methods for synthesizing fine powders are of significant interest, primary due to the overall simplicity of the technique. Also the method can guarantee a precise control of cationic stoichiometry and homogeneous mixture of metal ions at the atomic level. Fagui Qui et al.[76] prepared pure YAG powders by the gel combustion method. In pa[77] the same authors report the preparation of YAG:Nd powders with different doping concentrations from a mixed-metal citrate–nitrate precursor by a simple sol-gel combustion method at a relatively low temperature. The thermal behavior of the precursor, the phase transformation of the calcined powders, the micrographs of the precursor and the calcined powders, the lattice constant and the photoluminescence spectra of the gained YAG:Nd powders with different doping concentrations are investigated in this reference.

Nanopowders of YAG may be prepared by cryochemical synthesis, when aqueous solutions of the starting substances are rapidly frozen, and ice from a cryogranule is removed by sublimation from the obtained cryogranules. In order to implement the method French scientists[78] took aluminum lactate, yttrium and neodymium acetates, dissolved in boiling water and citric acid was added in order to maintain a pH level of 4. Then the boiling solution was atomized into liquid nitrogen and the powders obtained were placed in a vacuum sublimator. The precursor obtained was then heat treated at 800–1200 °C. The size of agglomerates of synthesized powders was from 0.2 to 4 μm. An advantage of this method is obtained very fine YAG powders and a disadvantage is organic compounds of starting components, a requirement for rigid control of the medium pH, a requirement of a considerable amount of liquid nitrogen, and special equipment[28,79,80].

Proposed by Jan Czochralski method[81] of crystal pulling from melt in 1918, becomes one of the most widely used methods for growth of dielectric and semiconductor crystals. Today Czochralski technique continues to progress and get replenished[82]. It should be noted that this method of crystal growth is continuously improved and developed with regard to the technical level of process automation and including thermodynamic considerations of growth processes even today. It permits to prepare a high quality bulk single crystals, among them silicon, as well as a multitude of oxides, fluorides, metals and alloys, multicomponent compounds and solid solutions[81,83]. Now, the main advantages of the Czochralski method are growing single crystals in defined crystallographic orientations with different sizes, shapes which are mainly limited by a design of crystal puller[81]. Kusuma et al.[83] represented data, that YAG:Nd crystal has been successfully grown by Czochralski method using automatic diameter control – crystal growth system.

1.1.3. Application

Yttrium aluminium garnet transparent ceramics have been suggested as suitable host materials for laser applications over the last few years thanks to their good optical and thermo-mechanical properties[84,85,86]. In comparison with single crystals, YAG transparent ceramics can be produced in larger volumes and lower cost, and can be heavily and homogeneously doped with laser-active ions. Some works have demonstrated that rare-earth-doped YAG ceramics have optical properties and laser performance equivalent to or even better than single crystals[41,52,87].

Improvements in powder synthesis and ceramic sintering as well as novel ideas have led to notable achievements. These include the first YAG:Nd ceramic laser in 1995, breaking the 1 KW mark in 2002 and then the remarkable demonstration of more than 100 KW output power from a YAG ceramic laser system in 2009. Additional developments have included highly doped microchip lasers, ultrashort pulse lasers, novel materials such as sesquioxides, fluoride ceramic lasers, selenide ceramic lasers in the 2 to 3 μm region, composite ceramic lasers for better thermal management, and single crystal lasers derived from polycrystalline ceramics. Reference[88] highlights some of these notable achievements.

Nd^{3+} doped YAG is currently the most widely employed solid-state laser material for micromachining, medical operations, materials processing and many other industrial and defense applications. Flash lamp is commonly used as a pumping source for YAG:Nd laser. Although it has low electro-optical conversion efficiency, high peak power and high energy lamp light can be applied directly on the laser media[89,90]. YAG:Nd lasers are based on single crystals, that are restricted to a maximum concentration of 1.4 at.% Nd^{3+}, as well as to centimeters in dimensions. This relatively low concentration level leads to a moderate Nd^{3+} pump absorption, strongly limiting the development of lasers of compact size, high power and efficiency. Furthermore, up to 9 at.% Nd^{3+} doped YAG ceramics were achieved without any deterioration in the achievable sample size or the optical quality. Since then, because of the significant potential for a new era of laser materials that are not single crystals, in addition to the obvious advantages in scaling, processing speed and cost, ceramic lasers gain media has become a highly active area of research worldwide[84].

When YAG is doped with Nd^{3+}, it is reported that the near-infrared laser output with high power and high slope efficiency was obtained in single crystals and polycrystalline transparent ceramic[91,92,93,94,95]. Nd^{3+} in YAG has a unique metastable level, placed in the region of 11500 cm^{-1}, able to provide laser emission in the 0.9 μm, 1 μm and 1.3 μm wavelength ranges on transitions to the lower $^4I_{9/2}$, $^4I_{11/2}$ and $^4I_{13/2}$ manifolds. This ion has rich structure of closely spaced energy levels above the emitting level, extending to UV, which can be used for pumping with broad-band optical sources such as lamps or solar radiation or with resonant diode lasers. The performance of the Nd^{3+} lasers under a broad-band pumping is limited by the poor overlap with the sharp and discrete absorption lines of Nd^{3+} and by the large quantum defect between the average pump quantum and the emitted radiation quantum. Since the first high quality YAG:Nd ceramic was fabricated in 1995, the ceramics have attracted much attention due to many advantages such as easy preparation of large single crystals of YAG:Nd, short fabrication time, high doping concentration and multifunctional composite structure[39,96,97,98,99,100,101]. Ceramic solid-state laser can be well matched with the transitional single crystal laser in output power and optical conversion efficiency. However, numerous approaches to YAG:Nd ceramics are focused on the $^4F_{3/2} \rightarrow {}^4I_{11/2}$ transitions at 1064 nm[102,103,104]. In recent years, the great interest in solid-state lasers operating at 266 nm, which quadruples the frequency of the 1064 nm line, was acknowledged for wide applications in the fields of industry, criminal investigation, and scientific research. For example, 266 nm laser can be used as a cleaning tool for removing copper oxide from copper and paint from aircraft[105,106,107]. Nd doped lutetium aluminum garnet have obvious advantages as high thermal conductivity, and moderate emission cross sections. This makes it’s potential applications in inertial confinement fusion (ICF) as gain material[62].

Eu^{3+} doped inorganic matrices are successfully employed as orange to red emitting phosphors. These materials are characterized by a very high quantum efficiency, sufficient absorption strength and stability. Upon excitation of the Eu^{3+} ion it emits due to the $^5D_0 \rightarrow {}^7F_J$ transitions, in particular for a high doping level and/or hosts with rather high phonon frequencies, e.g. phosphates or borates. Emission lines originating from $^5D_{1,2} \rightarrow {}^7F_J$ transitions are only present if the concentration is low and the highest phonon frequency of the host is low to prevent multiphonon or cross-relaxation of the higher excited states. Generally, the most intense emission lines originate from the $^5D_0 \rightarrow {}^7F_{1,2,4}$ transitions, which are located in the range from 580 to 720 nm[36]. The orange emission (590-600 nm) of Eu^{3+} due to the magnetic dipole transition $^5D_0 \rightarrow {}^7F_1$ is not affected much by the site symmetry, because they are partly-allowed, while the red emission (610-630 nm) due to the electric dipole transition of $^5D_0 \rightarrow {}^7F_{2,}$ being hypersensitive, is affected by the site symmetry of Eu^{3+} ion. In a crystal site inversion symmetry the electric dipole transition are strictly forbidden and the magnetic dipole transition are usually the dominant emission line. In a site without inversion symmetry the strength of electric dipole transition is higher. The $^5D_0 \rightarrow {}^7F_2$ transition is usually the strongest emission line in this case, because transition with $\Delta J = \pm 2$ are hypersensitive to small deviation from inversion symmetry[108]. The compounds doped with europium(III) have been explored for up-conversion and down-conversion of near UV and near IR radiation to improve the overall efficiency of Si solar cells[109,110,111,112]. The energy transfer between Ce^{3+} and Eu^{3+} was investigated[113]. However, it was shown that co-doped Eu^{3+} ions have the quenching effect for luminous Ce^{3+} ions in YAG[114.] Moreover, the authors[115] claimed that co-doped YAG:Ce,Eu shows separate luminescence of Ce^{3+} and Eu^{3+}. The role of RE^{3+} co-doped into the $CdSiO_3$:Mn^{2+} matrix and the possible long-lasting phosphorescence process was discussed in the reference[116]. The enhancement in emission intensity of co-doped blue nanophosphor was explained by energy transfer from the Er^{3+}/Nd^{3+} ions to the Eu^{2+} in the $BaMgAl_{10}O_{17}$[117]. The energy transfer mechanism from Ce^{3+} to Nd^{3+} and Sm^{3+} ions was also proposed[118]. Much more different sometimes contradictory results are published on this topics[119,120,121]. All these results obtained demonstrate that this topic still is on investigation by many research groups. Sm^{3+} in various solid matrices has long lived (ms) and intense visible emission from the $^4G_{5/2}$ level, the weak absorption in visible above this level and the absence of suitable pump sources, together with the emission self-quenching by cross-relaxation, restricted the applications to phosphors or to pressure sensors, with less interest for laser emission and limited the fundamental investigations too. Only recently the interest for Sm^{3+} in different materials (glasses, single crystals, polycrystalline materials or nanocrystalline powders) has increased due to the development of GaN laser diodes at ~405 nm that can excite efficiently the visible emission. The cubic materials, that can be produced by ceramic techniques, garnets or the isostructural sesquioxides R_2O_3 (R = Y, Lu, Sc), are attractive hosts for Sm^{3+} ion. In YAG the Sm^{3+} ions occupy a unique structural site of D2 symmetry, but in sesquioxides they can enter in two sites, both with sixfold O^{2-} coordination, of C2 and C3i symmetry[122,123,124,125]. In case of Sm^{3+}; $^4G_{5/2} \rightarrow {}^6H_{7/2}$ ($\Delta J = \pm 1$) is partly magnetic dipole and partly electric dipole emission band whereas $^4G_{5/2} \rightarrow {}^6H_{5/2}$ is purely magnetic dipole and $^4G_{5/2} \rightarrow {}^6H_{9/2}$ is purely electric dipole natured. The magnetic dipole transition $^4G_{5/2} \rightarrow {}^6H_{5/2}$ does not depend on chemical surroundings of the luminescent centre and its symmetry. However, the hypersensitive $^4G_{5/2} \rightarrow {}^6H_{9/2}$ transition is magnetic-dipole forbidden and electric dipole allowed and its intensity increase as the environmental symmetry become lower[24,126].

Rare earth element containing compounds, especially those containing Eu^{3+} and Sm^{3+} ions have attracted a special attention during the past decades for their superior optical properties such as narrow emission bands for high colour purity, high quantum efficiency, large stokes shifts and long life time. These materials have important applications in the display field due to their excellent fluorescence properties in the visible region[24,126].

Because of the large crystal field splitting of the 2-D level of Ce^{3+} ion in the garnet structure, YAG:Ce has a very efficient broad-band emission in the yellow spectral region when excited by blue light. This property makes YAG:Ce a suitable yellow-emitting phosphor for the application to white LEDs by combining it with blue LEDs[73,127].

1.2. Sol-Gel Chemistry Procesing

The sol-gel synthesis method offers a molecular-level mixing of precursors, which is capable of improving chemical homogeneity in comparison with conventional methods such as solid state reactions, wet precipitation, and hydrothermal synthesis[128]. Several chemical methods have been used for the synthesis of YAG nanophosphor such as co-precipitation[43], solvothermal[48], combustion[51], glycothermal treatments[129] and the sol–gel process[4]. Among these preparation methods, the sol–gel process provides some advantages. Different alternative chelating agents such as citrate, ethylene glycol, tartaric acid and polyvinyl alcohol, etc. have been used for the synthesis of YAG phosphors[130]. The reasons for the particular value of and interest in sol-gel synthesis are given below.

- The temperature required for all stages are low, frequently close to room temperature. Thus thermal degradation of both the material itself and any entrapped species is minimized, and high purity and stoichiometry can be achieved.

- The low temperature of sol-gel processes is generally below the crystallization temperature for oxide materials, and this allows the production of unusual amorphous and nanocrystalline materials.
- Since precursors involving different metals are frequently miscible, homogenous controlled doping is easy to achieve.
- By using organometallic precursors containing polymerizable organic ligands, materials may be produced which contain both inorganic and organic polymer networks.
- The chemical conditions are mild. In this way pH sensitive organic and biological species may be enterapped and still retain their functions.
- Since liquid precursors are used it is possible to cast ceramic materials in a range of complex shapes and to produce thin films or fibres as monoliths, without the need for machining or melting[53].

The sol-gel method is well established: the first scientific references based on the method were published at the beginning of the XX century. Recently, the sol-gel method become useful to produce materials for optoelectronic and optocommunication (photonic). For example, nanocrystalline oxide powders doped with rare-earth ions exhibit a strong luminescence. They may be used to produce laser ceramics and photonic wires[131,132,133]. Formation of YAG doped with the rare-earth ions in the monocrystallic form is an expensive and time-consuming process. Precursors for YAG nanocrystals can be obtained by two routes using metal alkoxides or inorganic salts. Originally the alkoxide way was applied[134]. But preparation of YAG using metal alkoxides is expensive, sophisticated and time–consuming manner. The second way based on inorganic salts is faster, cheaper and less complicated. It additionally requires to use the complexing agents: citric acid[135,136,135], ethylene glycol[36] or ethylenediamine-tetraacetic acid (EDTA)[53].

The synthesis of nanopowders by the sol-gel method bases on the formation of a water colloid suspension (sol) in the course of hydrolysis of metal compounds to hydroxides. The sols transform next into sticky gels, and after drying at 120 °C, into solid xerogels. The polycrystalline YAG precursor powders were formed as a result of thermal treatment at 1000 ^{o}C[53,134,135]. The formation of polycrystalline powders of YAG proceeds via several stages[5,51,112,137,138].

Starting metal oxides could be dissolved in concentrated acetic acid with small amount of water (the access of the acid is evaporated), and metal salts just in watter. Clear solutions are obtained after stirring in beakers covered with a watch-glass. Then metal acetates or nitrates are added. Finally, the complexing agent (1,2-ethanediol, tartaric acid, malonic acid, citric acid, oxalic acid or ethylenediaminetetraacetic acid (EDTA) is added[15,139,140,141,142]. The beaker with formed sol is placed into the dryer or left on the heating plate under stirring to evaporate all the solvent. The obtained gel is dried, ground and annealed at different temperatures including intermediate pre-grinding with a purpose to get well crystallized powders.

The following mechanism of the formation of YAG was proposed[53]. The process starts with dissolution of yttrium and neodymium oxides in acetic acid:

$Y_2O_3 + 6\ CH_3COOH = 2\ Y(CH_3COO)_3 + 3\ H_2O$ (1a)

$Nd_2O_3 + 6\ CH_3COOH = 2\ Nd(CH_3COO)_3 + 3\ H_2O$ (1b)

The yttrium and neodymium acetates formed as well as aluminum nitrate undergo dissociation into ions:

$Y(CH_3COO)_3 = Y^{3+} + 3CH_3COOH^-$ (2a)

$Nd(CH_3COO)_3 = Nd^{3+} + 3CH_3COOH^-$ (2b)

$Al(NO_3)_3 = Al^{3+} + 3NO_3^-$ (3)

The temperature and weak acidic environment cause hydrolysis and yttrium, neodymium and aluminum hydroxides are produced:

$M^{3+} + 3HOH = Me(OH)_3$ (4)

where M stands for Y, Nd or Al.

The hydroxides undergo olation or oxolation and the metals become to be bound by the oxygen bridges:

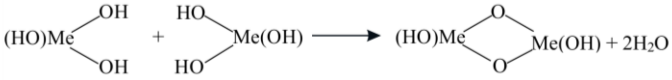

(5)

The complexing agent plays an important role: each ethylene glycol molecule can bind the oxygen bridged metal compounds through the two hydroxide groups into olygomers. As a result, a matrix influencing precursor molecule size appears:

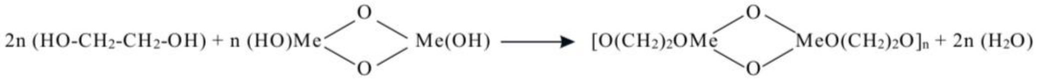

(6)

1.3. Introducton to Solvothermal Processing

A solvothermal process can be defined as “a chemical reaction in a closed system in the presence of a solvent (aqueous and non aqueous solution) at a temperature higher than that of the boiling point of such a solvent”. Consequently, a solvothermal process involves high or moderate pressures (typically between 1 atm and 10,000 atm). The selected temperature (typically between 100 ˚C and 1000 ˚C) depends on the required reactions for obtaining the target-material through the involved process. If water is used as the solvent, the method is called “hydrothermal synthesis”. The hydrothermal technology have been studied and developed a long time ago with different objectives[143]. The process can be used to prepare many geometries including thin films, bulk powders, single crystals and nanocrystals. In addition, the morphology (sphere (3D), rod (2D), or wire (1D)) of the crystals formed is controlled by manipulating the solvent supersaturation, chemical‘s concentration and kinetic control. The method can be used to prepare thermodynamically stable and metastable states including novel materials that cannot be easily formed from other synthetic routes. Over the last decade, a majority (~80%) of the literature concerning solvothermal synthesis has focused on nanocrystals[144].

The YAG-based materials are normally synthesysed at a relatively high temperature (>1500 ˚C) by a solid state reaction of a stechiometric micture of the component oxides with prolong heating time. Sovothermal synthesys are conducted in stailness steel autoclave[145,146] (Fig. 2).

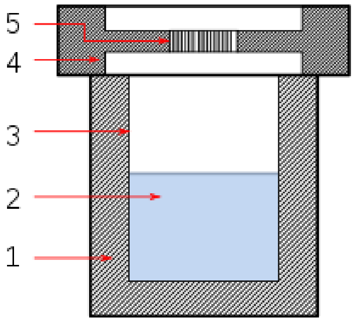

Fig. 2. Schematic diagram of solvothermal synthesis setup: (1) stainless steel autoclave, (2) precursor solution, (3) Teflon liner, (4) stainless steel lid (5) spring.

Solvothermal method exploits the solubility of almost all inorganic substances in solvent at elevated temperatures and pressures and subsequent crystallization of the dissolved material from the fluid. It is known that the properties of nano/micro crystals depend not only on their composition, but also on their structure, phase, shape, size, and size distribution[147]. The selection of the solvent plays a key-role through the control of the chemical mechanisms leading to the target-material[143]. For example, Kudryashova et al.[146] have described the preparation of YAG using a mixture of yttrium chloride, aluminum chloride and aluminum isopropylate, and using the same experimental conditions but changing only the nature of the solvent (diphenyloxide, oleic acid, stearic acid, and oleylamine). Thermal treatment of this mixture was carried out at 250–300 °C in an argon atmosphere from 8 to 24 h. It was shown that different solvents can play an important role in the properties of the final products[143,146].

Among the various synthesis techniques, solvothermal treatment as a typical solution approach has proven to be an effective and convenient process in preparing various inorganic materials with a variety of controllable morphologies and architectures. The advantage of the solvothermal method is: materials can be synthesized at relatively low temperatures without milling or calcination. Since water is an ideal solvent for most inorganic species, and ethanol is a good solvent for most of the surfactants, most of the soluble inorganic salts can be adopted as the starting materials. Moreover, long alkyl chain surfactants such as sodium oleate or oleylamine can be used as protecting reagents to prevent agglomeration and control the morphology development of nanocrystals since they can complex with different metal ions to form metal salts, which may covalently combine the surface of the nanocrystals. Therefore, the long alkyl chain surfactants are suitable choices as both precursors and protecting reagents for the development of a general synthetic method to fabricate monodisperse nanocrystals with inorganic salts[148,149,150].

The hydrothermal/solvothermal process is a green process because of the closed system conditions used in hydrothermal reactors, and it has been extensively used for growing single crystals, for example, quartz and many kinds of metal oxides[151,152,153], metals[154] and semiconductors[155],[156].

2. EXPERIMENTAL PART

2.1. Reagents and Solutions

The following starting materials were used for the synthesis and analysis: Ho_2O_3 (Merck, 99.9%), Tb_4O_7 (Merck, 99.9%), Dy_2O_3 (Merck, 99.99%), Eu_2O_3 (Alfa Aesar, 99.99%), $Eu(NO_3)_3{\cdot}6H_2O$ (Alfa Aesar, 99.99%), $Ho(NO_3)_3{\cdot}5H_2O$ (Alfa Aesar, 99.99%), $Nd(NO_3)_3{\cdot}6H_2O$ (Alfa Aesar, 99.9%), $Sm(NO_3)_3{\cdot}6H_2O$ (Alfa Aesar 99.9%), $Y(NO_3)_3{\cdot}6H_2O$ (Alfa Aesar, 99.9%), Er_2O_3 (Sigma Aldrich, 98.0%), Yb_2O_3 (Sigma Aldrich, 98.0%), Lu_2O_3 (Sigma Aldrich, 98.0%), Tm_2O_3 (Sigma Aldrich, 98.0%), $Al(NO_3)_3{\cdot}9H_2O$ (Eurochemicals 99.99%), $Al(NO_3)_3{\cdot}9H_2O$ (Alfa Aesar, 99.99%), $HOCH_2CH_2OH$ (1,2-etandiol, Roth, 99.5%), NH_3 (Merck), C_2H_5OH (Abs. Scharlau), HNO_3 (Roth, 65 wt.%), CH_3COOH (Roth, glacial acetic acid).

2.2. Synthesis Methods

Various lanthanide aluminium garnets have been synthesized utilizing two different sol-gel and solvothermal methods.

2.2.1. Sol-gel method

The lanthanide aluminium garnet samples were synthesized by an aqueous sol-gel method with optimized synthesis parameters[35,157]. For the preparation of $Tb_3Al_5O_{12}$:Eu, $Dy_3Al_5O_{12}$:Eu, $Ho_3Al_5O_{12}$:Eu, $Y_{3-x}Sm_xAl_5O_{12}$, $Y_{2.9}Sm_{0.1}Al_5O_{12}$:Eu, $Y_{3-x}Sm_xAl_5O_{12}$:Eu, $Y_{3-x}Nd_xAl_5O_{12}$, $Y_{2.9}Nd_{0.1}Al_5O_{12}$:Eu, $Y_{3-x}Nd_xAl_5O_{12}$:Eu, $Er_3Al_5O_{12}$:Eu, $Yb_3Al_5O_{12}$:Eu, $Lu_3Al_5O_{12}$:Eu, $Tm_3Al_5O_{12}$:Eu samples yttrium and lanthanide oxides were dissolved in concentrated acetic acid (about 10 mL) with small amount of water. Clear solutions were obtained after stirring at 60-65°C in beakers covered with a watch-glass. Metal nitrites were dissolved in distilled watter. Then aluminium nitrate nonahydrate and appropriate quantity of europium oxide dissolved in small amount of acetic acid were added to the above solution and diluted to 100 mL. The resulting mixtures were stirred at 65 °C for 1 h, followed by dropwise addition of ethane-1,2-diol upon vigorous stirring. The resulting solution was mixed at the same temperature for another 1 h and then concentrated by slow solvent evaporation at 65 °C until solution turned into transparent gels. The gels were dried in an oven at 100 °C for 24 h. The resulting gel powders were ground in an agate mortar and heated in air at 800 °C for 4 h by slow temperature elevation (5 °C min^{-1}). After grinding in an agate mortar, the powders were further sintered in air at 1000 °C for 10 h. The simplified scheme of the sol-gel route used is presented in Fig. 3.

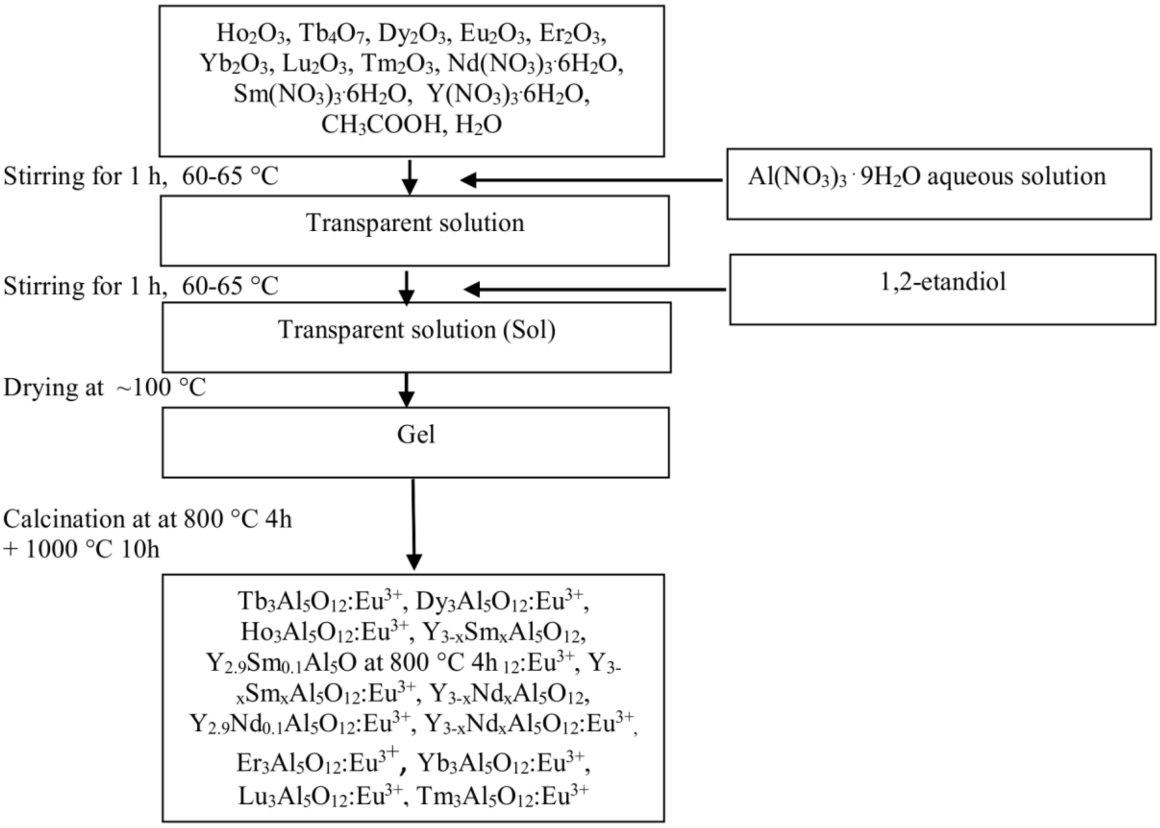

Fig. 3. Schematic representation of the steps involved in the sol-gel processing.

2.2.2. Solvothermal method

For the preparation of HoAG:Eu the $Al(NO_3)_3 \cdot 9H_2O$, $Ho(NO_3)_3 \cdot 5H_2O$ and $Eu(NO_3)_3 \cdot 6H_2O$ were used as starting materials. Firstly, aluminium, holmium and europium solution was prepared by dissolving metal nitrates in 50 ml of deionized water. The resulting mixture was stirred until substances fully dissolved. Secondly, ethane-1,2-diol (Me:Et ratio 1:2) upon vigorous stirring was added to the above solution. The aluminium, holmium and europium hydroxides were precipitated by dropwise addition of excess of 10% ammonia solution under vigorous stirring. The precipitates were repeatedly centrifuged and washed with distilled water to remove the residual ammonia. The washed hydroxides were dispersed in ethane-1,2-diol and then placed in an autoclave with a Teflon liner. The autoclave was heated up to the 220 °C and maintained at this temperature for 20 h. The obtained powders were centrifuged and repeatedly washed with ethanol solution, dried in the air at 80 °C and then annealed at different temperatures for 4 h. The simplified scheme of the solvothermal method is presented in Fig. 4.

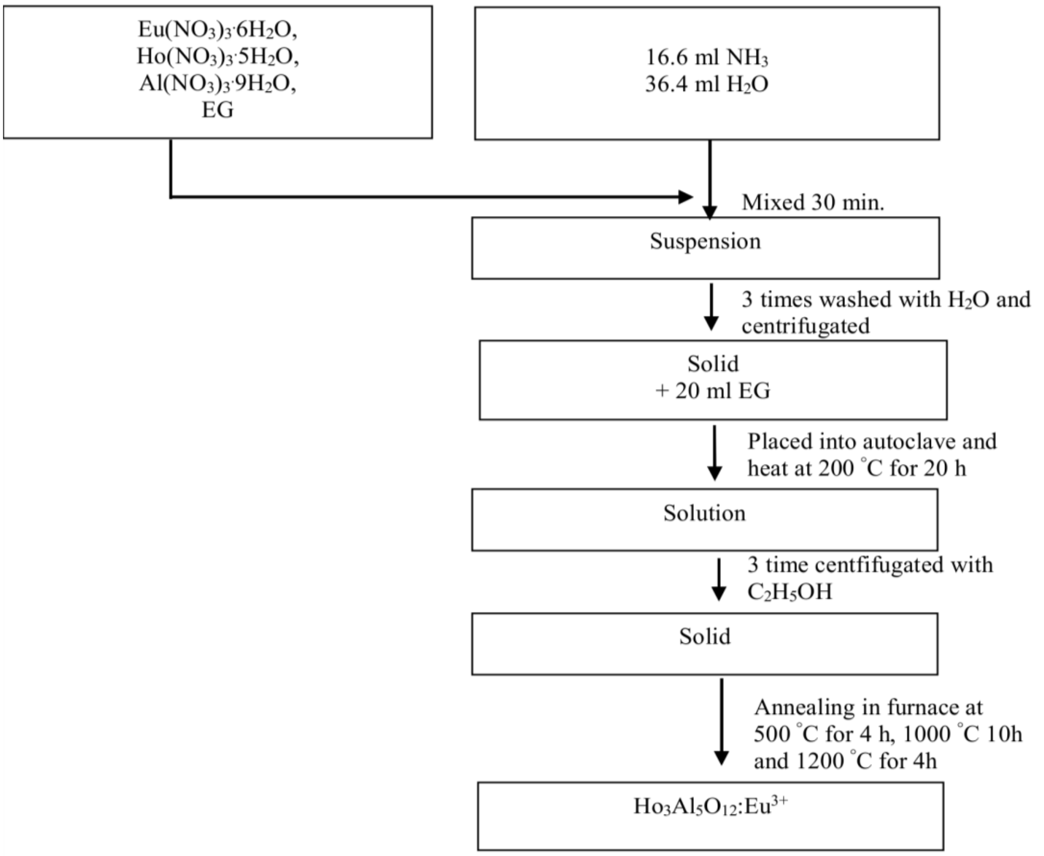

Fig. 4. Schematic representation of the steps involved in the HoAG:Eu by solvothermal method.

2.3. Instrumentation and Characterization Techniques

The phase purity and crystallinity of synthesized samples were characterized by X-ray powder diffraction (XRD) analysis on D8 Bruker AXS powder diffractometer using Cu Kα1 radiation. The diffraction patterns were recorded at the standard rate of 1.5 2θ/min. The XRD patterns of HoAG:Eu synthesized by solvothermal method were recorded on a Siemens D5000 diffractometer with Cu Kα radiation (using a step of 0.05º 2θ and 1.5s/step). Some XRD analyses were carried out on a Siemens D5000 X-Ray powder diffractometer.

The infrared spectroscopy (FTIR) measurements were recorded with a Perkin-Elmer FT-IR Spectrum 1000 spectrometer or with FT-IR Bruker Vertex 70 FT-IR spectrometer.

Scanning electron microscope (SEM) images were obtained using a Hitachi SU-70 scanning electron microscope and JEOL JEM-3100F field emission scanning electron microscope.

The local structure of garnets was investigated by solid-state nuclear magnetic resonance spectroscopy (NMR). ^{27}Al MAS (Magic-Angle Spinning) NMR spectra were recorded on a 600 MHz (14.1 T) Varian NMR system equipped with a 1.6mm NB Triple Resonance HXY Fast MAS probe. Larmor frequency for ^{27}Al was 156.25 MHz and chemical shift axis was referenced to 1 M $Al(NO_3)_3$. MAS frequency was 32 kHz. ^{27}Al spectra were measured using a short excitation pulse with the duration of 1 μs. The number of scans was 800 and the relaxation delay was 1 s. MAS NMR spectra were acquired on an Agilent VNMRS DirectDrive 400MHz spectrometer (9.4 T wide bore magnet) equipped with a T3HX 3.2 mm probe.

Raman spectra were recorded using Horiba Jobin Yvon T64000 Raman spectrometer equipped with a BXFM Olympus 9/128 microscope, a Horiba JY Symphony CCD detector and a 488 nm Lexell SHG laser.

Luminescence properties were measured using Edinburgh Instruments FLS980 spectrometer equipped with double excitation and emission monochromators, 450 W Xe arc lamp, mirror optics for powder samples and liquid nitrogen cooled (-80 °C) NIR detector (Hamamatsu R5509 - 42). Emission spectra were conducted using an OPO (optical parametric oscillator) pumped by the third harmonic of a Thales Q-switched Nd:YAG laser. An ICCD Roper Scientific camera (intensified charge coupled device) coupled to an HR 250 Jobin–Yvon monochromator was used to detect and analyse the fluorescence. values were extracted from the shape of the decay profiles. All optical measurements have been made at room temperature. Fluorescence data characterized by fluorescence spectrophotometer Cary Eclipse Varian.

Particle size distributions of aqueous suspensions of the powders were measured with a Malvern Zetasizer Nano ZS analyzer.

The particles were characterised by transmission electron microscopy (TEM) (FEI Tecnai G2 Spirit Twin). After a sonication step of 30 seconds, a small drop of a suspension of the sample was casted on a carbon coated copper grid (EMS, FCF-200-Cu), after which the whole was dried overnight under an infrared lamp. The TEM was operated at 120 kV.

3. RESULTS AND DISCUSSION

3.1. Sol-Gel Synthesis and Characterization of Eu^{3+}-Doped Tb, Dy and Ho Aluminium Garnets

In this part of dissertation a sol-gel method based on in-situ generation of mixed-metal chelates by complexing metal ions with ethane-1,2 diol in an aqueous media has been elaborated to prepare lanthanide-ion containing garnets, $Tb_3Al_5O_{12}$ (TAG), $Dy_3Al_5O_{12}$ (DAG) and $Ho_3Al_5O_{12}$ (HAG) doped with different amount of Eu.

3.1.1. XRD, FTIR, SEM, DLS, NMR and Raman analyses

The phase purity and compositional changes of the LnAG doped with different amount of Eu^{3+} ions were controlled by X-ray diffraction analysis. The XRD patterns of corresponding $Tb_3Al_5O_{12}$ (TAG), $Dy_3Al_5O_{12}$ (DAG) and $Ho_3Al_5O_{12}$ (HAG) with different doping level of Eu synthesized at 1000 ^oC are shown in Fig. 5. The XRD results presented in Fig. 5 (a) revealed that ceramics obtained at 1000 °C consists of one crystalline phase: terbium aluminium garnet ($Tb_3Al_5O_{12}$, TAG). The obtained XRD patterns are in a good agreement with the reference data for $Tb_3Al_5O_{12}$ (PDF [04-006-4054]). Fig. 5 (b) shows that only one dysprosium aluminium garnet $Dy_3Al_5O_{12}$ phase (PDF [04-006-4053]) was obtained after calcination of Dy-Al-O:Eu precursors at 1000 °C. In the case of the Ho-Al-O system, the analogous results to the Tb-Al-O and Dy-Al-O systems were obtained. In Fig. 5 (c) the X-ray diffraction patterns of the final Ho-Al-O ceramic samples annealed at 1000 °C are presented. The XRD patterns prove the formation of the cubic holmium aluminium garnets ($Ho_3Al_5O_{12}$). Evidently, the obtained XRD patterns are in a good agreement with the reference data for $Ho_3Al_5O_{12}$ (PDF [04-001-9715]). Thus, we can conclude that the 1000 ^oC temperature is high enough for the formation of Eu^{3+}-doped $Tb_3Al_5O_{12}$, $Dy_3Al_5O_{12}$ and $Ho_3Al_5O_{12}$ garnets.

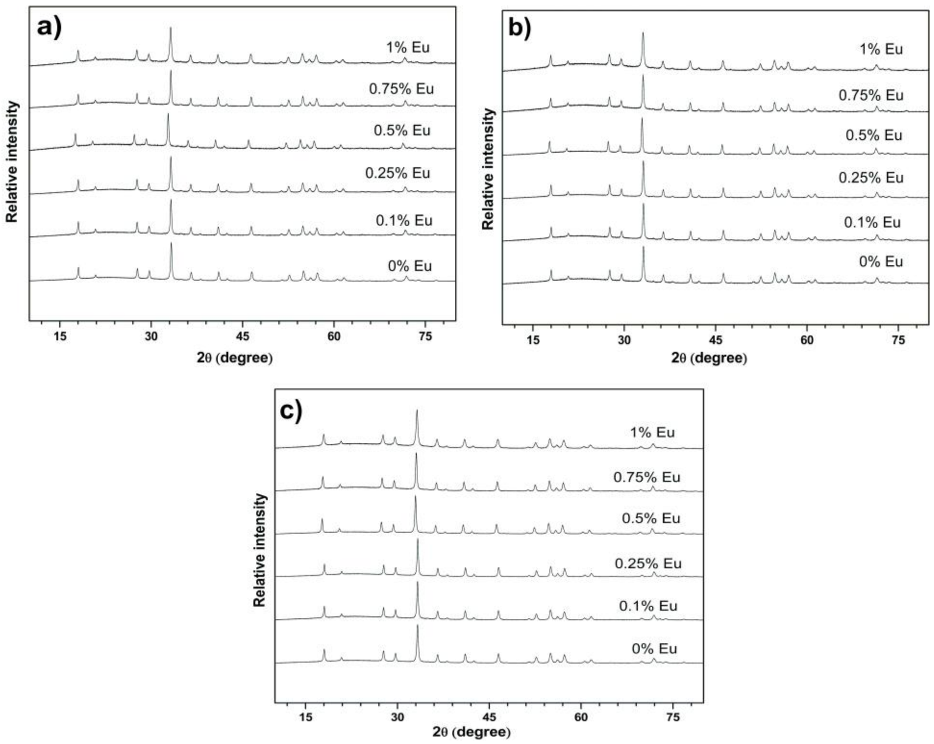

Fig. 5. XRD patterns of the Tb-Al-O:Eu (a), Dy-Al-O (b) and Ho-Al-O (c) gels annealed at 1000 °C. $Tb_3Al_5O_{12}$ PDF [04-006-4054], $Dy_3Al_5O_{12}$ PDF [04-006-4053], $Ho_3Al_5O_{12}$ PDF [04-001-9715].

FTIR spectroscopy was used as additional tool for the structural characterization of the ceramic materials obtained by the aqueous sol-gel method. The FTIR spectra of ceramic materials obtained after the calcinations of the Ho-Al-O:Eu gels at 1000 °C for 10 h are shown in Fig. 6 (c). The FTIR spectra of synthesized ceramics show several quite intense broad bands at 675 cm^{-1}, 720 cm^{-1} and 775 cm^{-1}, which are typical metal-oxygen (M-O) absorptions for the garnet-type compounds[97,157]. The FTIR spectra of Tb-Al-O (Fig. 6 (a)), Dy-Al-O (Fig. 6 (b)) garnets doped with europium were very similar to the presented in Fig. 6 (c). The most important feature is that intensive bands are determined in the region of 900–450 cm^{-1}, which may be also attributed to the stretching modes of the isolated [AlO_4] tetrahedra and [AlO_6] octahedra in the garnet structure, i.e. these bands correspond to the formation of crystalline TAG:Eu, DAG:Eu and HAG:Eu. Thus, the observed M–O vibrations which in view of the earlier reports are characteristic of RE–O and Al–O stretching frequencies let us to conclude, that the FTIR results are consistent with crystallization process observed by XRD measurements. Consequently, the FTIR results absolutely support the conclusions made on grounds of the XRD measurement and prove that there is no left organic matter in the sol-gel derived garnet structure compounds[24, 48,51, 97,158,159,160,161, 162].

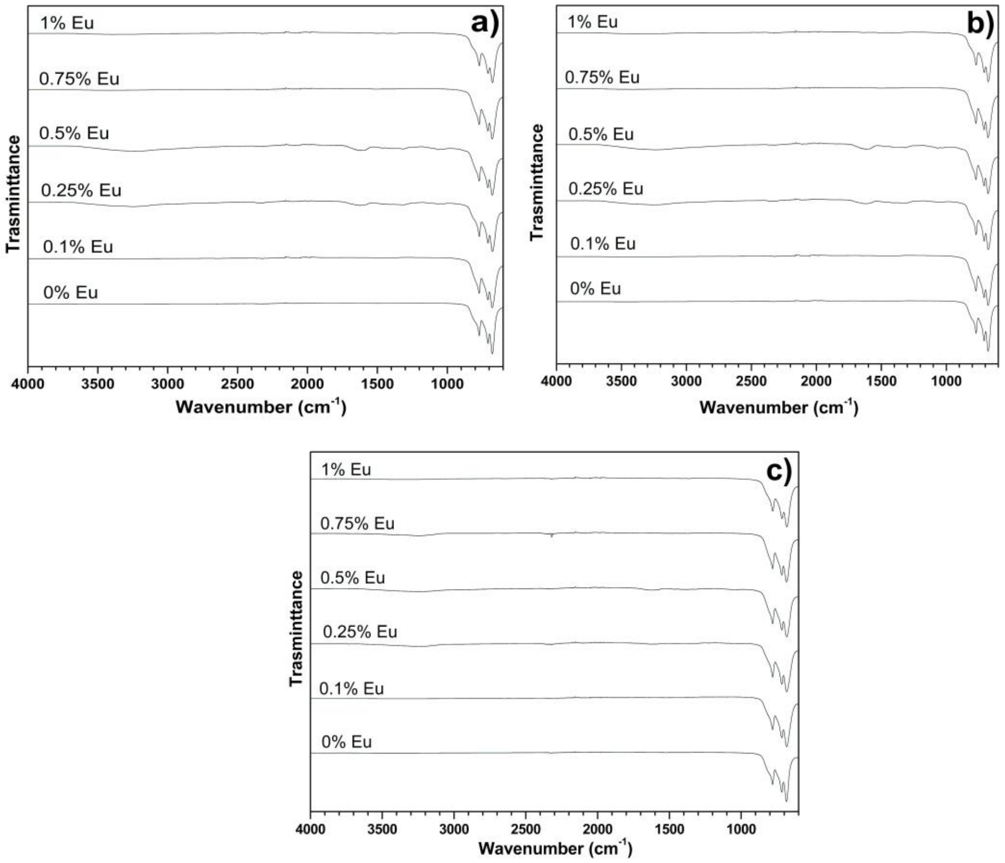

Fig. 6. FTIR spectra of Tb-Al-O:Eu (a), Dy-Al-O (b) and Ho-Al-O (c) garnets synthesized at 1000 ^{o}C.

The textural properties of the calcined Tb-Al-O:Eu, Dy-Al-O:Eu, Ho-Al-O:Eu powders were investigated by SEM, from which the grain size and typical morphologies were obtained. Scanning electron micrographs of the Tb-Al-O:0.5%Eu, Dy-Al-O:0.5%Eu and Ho-Al-O:0.5%Eu samples obtained at 1000 ^{o}C are shown in Fig. 7. Individual particles seem to be submicro-sized plate-like crystals and they partially fused to form hard agglomerates. The SEM micrographs presented in Fig. 7 show the formation of very homogeneous mixed-metal oxides, and the formation of a continuous network of crystallites is characteristic feature for these materials. The $Dy_3Al_5O_{12}$:Eu and $Ho_3Al_5O_{12}$:Eu garnet particles are a little differently shaped comparing with $Tb_3Al_5O_{12}$:Eu garnet. Apparently, the particles were formed with more pronounced agglomeration, indicating good connectivity between the grains which is characteristic feature for ceramic composite material[163].

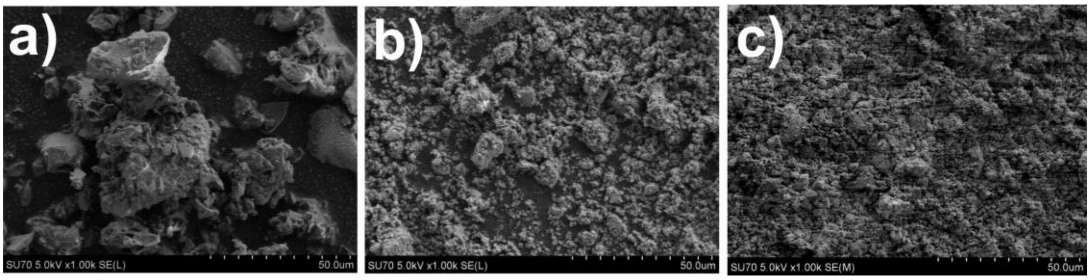

Fig. 7. SEM micrograph of the $Tb_3Al_5O_{12}$:0.5%Eu (a), $Dy_3Al_5O_{12}$:0.5%Eu (b) and $Ho_3Al_5O_{12}$:0.5%Eu (c) garnets.

The particle size distribution in $Ho_3Al_5O_{12}$:Eu garnets annealed at 1000 °C for 10 h were investigated by dynamic light scattering (DLS) (Fig. 8).

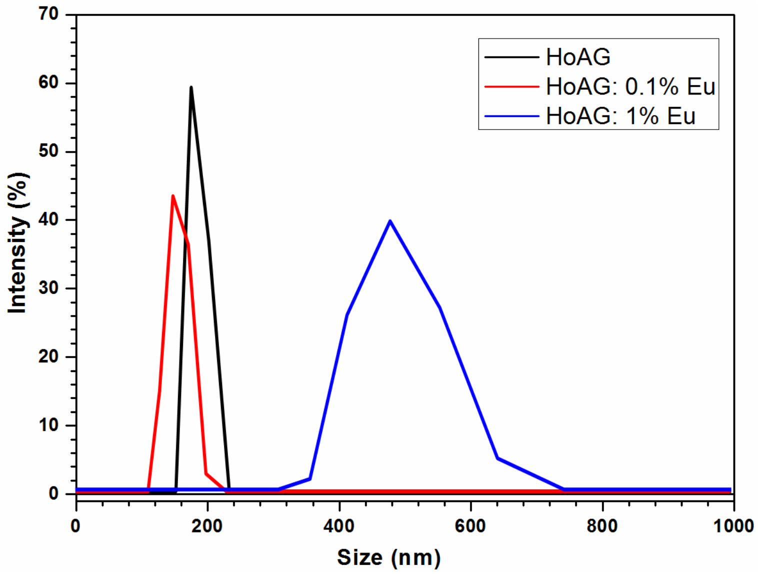

Fig. 8. Dynamic light scattered measurements of HoAG:Eu

When Eu doping level less or equal 0.1% very narrow particle size distribution (~420 nm) was determined. The sample with higher europium concentration (0.5%) was composed of larger particles (~700 nm). When garnet doped with 0.25% - 0.75% of Eu^{3+} some particles were much larger, and consequently the particle size is not stable and split in a biggest range. However, the biggest particle size was determined for the sample with 1% of doping level of Eu. Interestingly, the DLS results fit very well with scanning electron microscopy data showing that 0.5% of Eu is the optimum doping level for Tb, Dy and Ho aluminium garnets having very homogeneous particle size distribution.

It was impossible to observe NMR and RAMAN spectroscopy data of Tb-Al-O:Eu, Dy-Al-O:Eu and Ho-Al-O:Eu samples.

3.1.2. Optical Properties

The fluorescence data of $Ho_3Al_5O_{12}$:Eu are shown in Fig. 9.

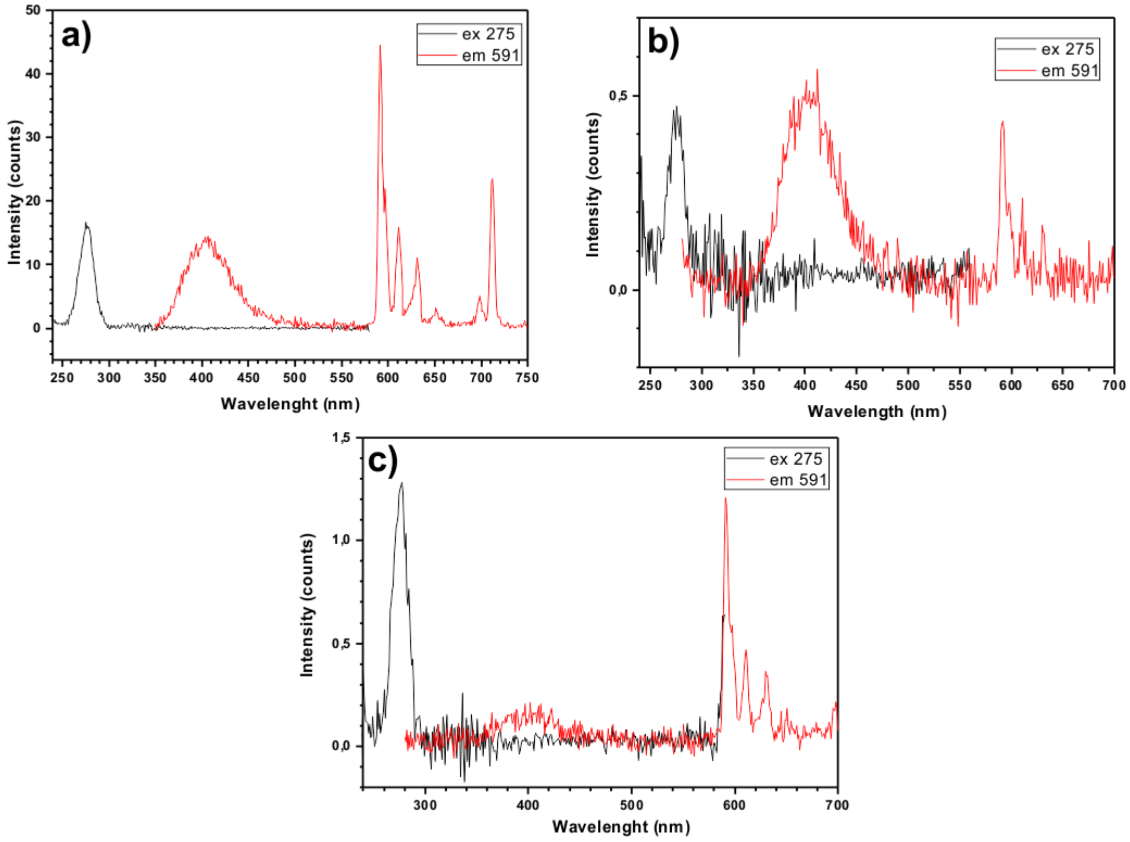

Fig. 9. Fluorescence measurement data of $Ho_3Al_5O_{12}$:Eu garnets. 0.5% Eu (a), 0.75% Eu (b), 1% Eu (c).

As seen in Fig. 9 (a) the 0.5% Eu^{3+}-doped sample shows the most intensive europium emission. This might be associated with XRD results (peaks with 0.5% europium are shifted to the smaller 2θ). The sample having 1% of Eu shows fluorescence, however, not so intensive as the sample with 0.5% of Eu, but more intensive than 0.75% Eu-doped sample. These results are unpredictable and very hard to explain. The XRD data also showed the smaller shift for 0.75% Eu and 1% Eu samples. It is well known, that phosphors with spherical shaped particles (≤ 2 μm) are of greater importance because of their high packing density, lower scattering of light, brighter luminescent performance, high definition and more improved screen packing density. This could explain why HoAG with 0.5% of europium doping shows the best luminescent properties[49,164]. Besides, the $Ho_3Al_5O_{12}$:Eu samples with doping of 0.1% Eu and 0.25% Eu do not show any emission.

Fig. 10 and 11 represent luminescence spectra of $Tb_3Al_5O_{12}$:Eu and $Dy_3Al_5O_{12}$:Eu garnets, respectively. The emission spectra were obtained using 277 nm excitation. The emission peaks were fixed between 550 and 720 nm and are in a good agreement with the reported values of emission transitions for Eu^{3+} [110,165]. The emission spectral lines of Eu^{3+} ion are sharp due to the screening of 4f orbital by 5s and 5p orbitals from crystal field of the host lattice. The spectra show the characteristic emission of Eu^{3+} arising due to $^5D_0 \rightarrow {}^7F_1$ (591nm), $^5D_0 \rightarrow {}^7F_2$ (611nm) and $^5D_0 \rightarrow {}^7F_4$ (708nm) transitions[166,167]. Fig. 11 also show additional peaks in excitation spectra (Fig. 10 (a)) which ocours from $^7F_6 \rightarrow {}^5H_{5,6,7}$, and $^7F_6 \rightarrow {}^5D_3$ transitions typical for Tb^{3+} ion. The excited electrons can relax to the ground states yielding the characteristic emission of Eu^{3+} ion. Observed energy transferred from the $^5D_3$ level of Tb^{3+} to the $^5D_1$ and/or $^5D_0$ levels of Eu^{3+}.

The obtained photoluminescence lifetimes show a decrease (Fig. 12 (b)) from 2.58 to 1.98 ms with increasing the concentration of dopant. Upon increasing the dopant concentration the decay becomes faster (Fig 12 (a)). In our case the maximum decay time is 2.58 ms with 0.1 mol% of Eu. An increase of lanthanide content may increase the number of ions occupying the surface states in nanoscale dimensional materials and these states may be leading to concentration – quenching behaviour[110,168].

3.2. Sol-Gel Synthesis and Characterization of Eu^{3+} - doped Er, Yb, Lu and Tm Aluminium Garnets

In this part of dissertation Er, Yb, Lu, and Tm aluminium garnets and Er, Yb, Lu, Tm aluminium garnets doped with Eu^{3+} have been synthesized by sol-gel method.

3.2.1. XRD, FTIR, TEM and NMR analyses

The XRD patterns of corresponding $Er_3Al_5O_{12}$ (EAG), $Tm_3Al_5O_{12}$ (TAG), $Yb_3Al_5O_{12}$ (YAG) and $Lu_3Al_5O_{12}$ (LAG) with different doping level of Eu synthesized at 1000 ºC are shown in Fig.13.

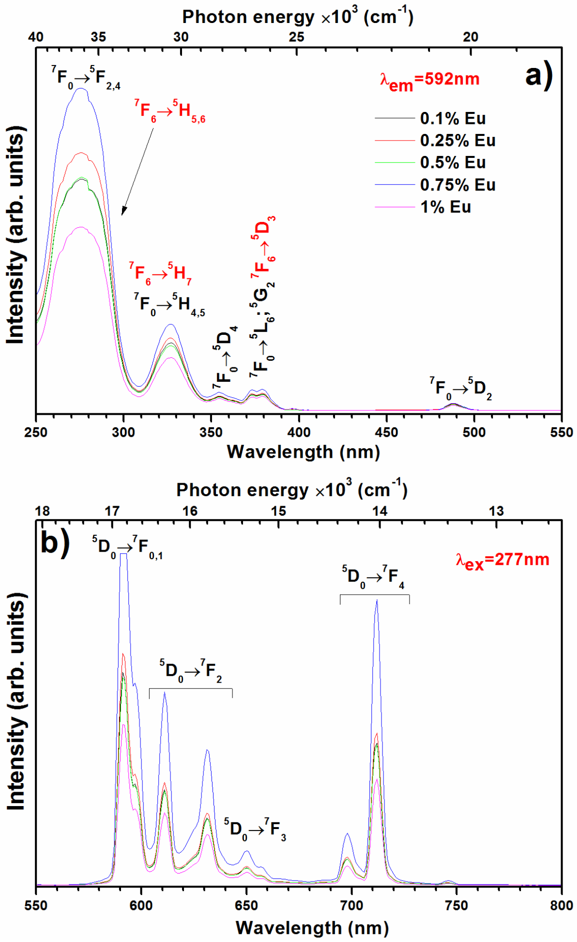

Fig. 10. Luminescent spectra of $Tb_3Al_5O_{12}$:Eu garnets: excitation (a) and emission (b).

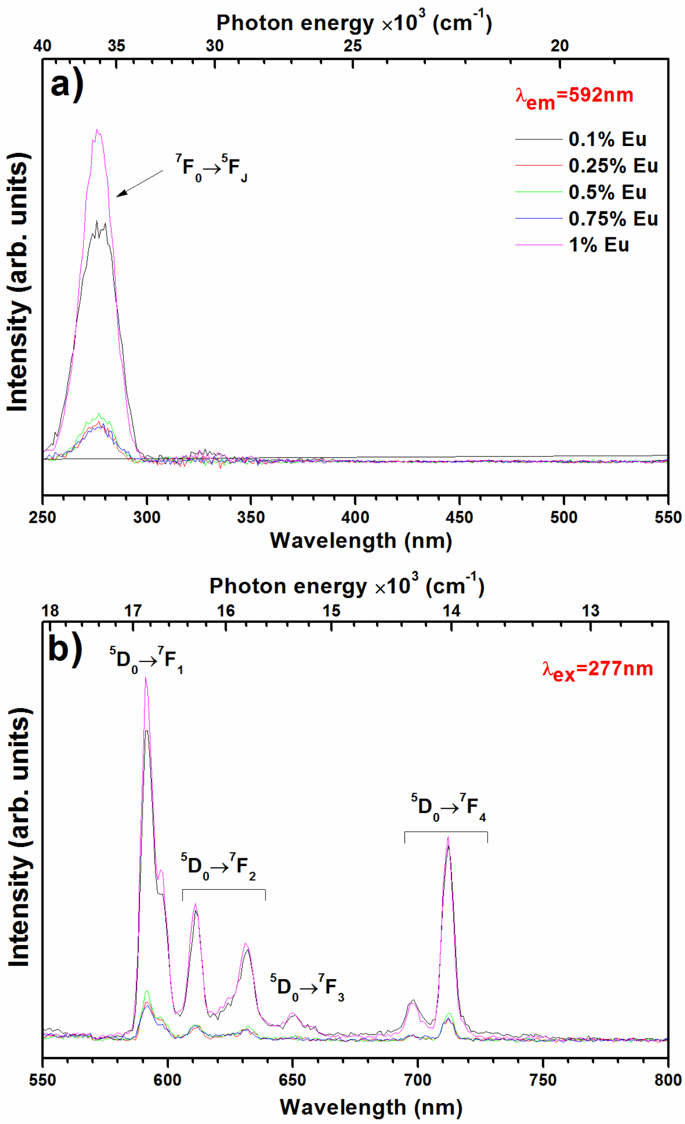

Fig. 11. Luminescent spectra of $Dy_3Al_5O_{12}$:Eu garnets: excitation (a) and emission (b).

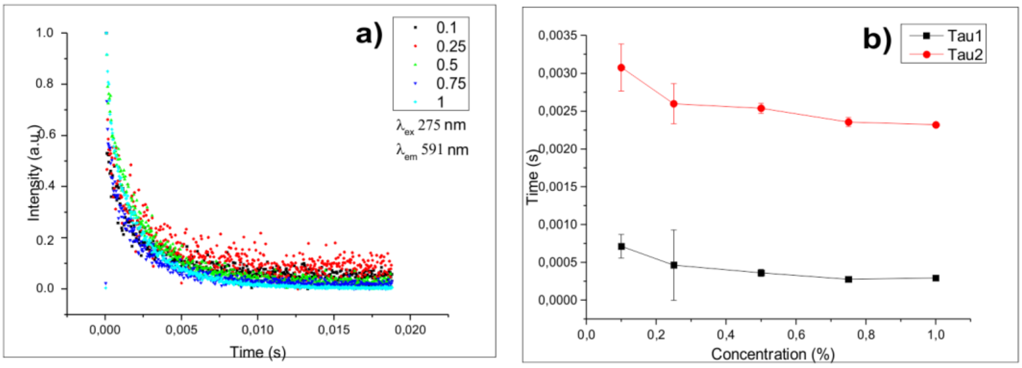

Fig. 12. The decay curves (a) and life time (b) for $Ho_3Al_5O_{12}$:Eu garnet.

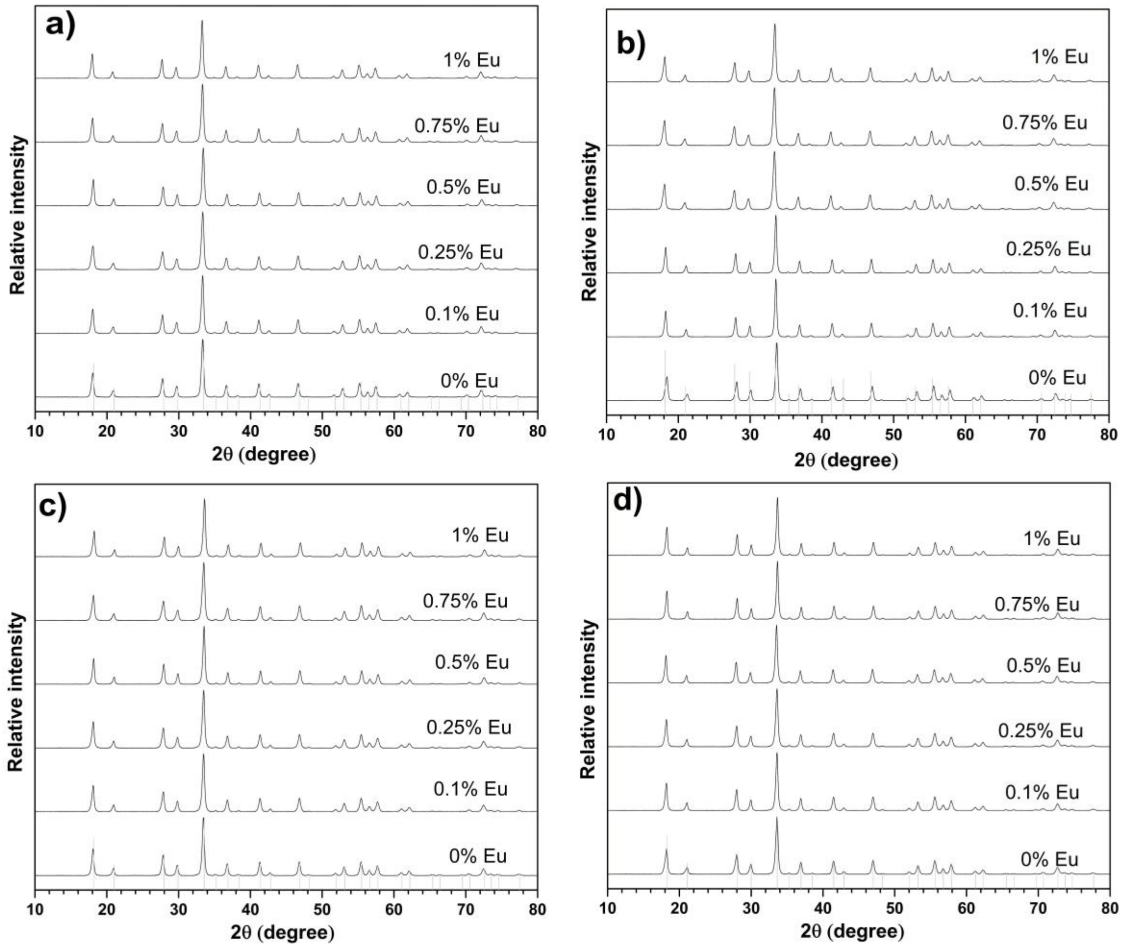

Fig. 13. XRD patterns of $Er_3Al_5O_{12}$:Eu (a), $Tm_3Al_5O_{12}$:Eu (b), $Yb_3Al_5O_{12}$:Eu (c) and $Lu_3Al_5O_{12}$:Eu (d) samples annealed at 1000 °C. $Er_3Al_5O_{12}$ PDF [01-078-1451], $Tm_3Al_5O_{12}$ PDF [00-017-0734], $Yb_3Al_5O_{12}$ PDF [01-073-1369], $Lu_3Al_5O_{12}$ PDF [01-073-1368].

The XRD results presented in Fig. 13 (a) revealed that ceramics obtained at 1000 °C consists of one crystalline erbium aluminium garnet phase. The obtained XRD patterns are in a good agreement with the reference data for $Er_3Al_5O_{12}$ (PDF [01-078-1451]). Fig. 13 (b) shows that only one thulium aluminium garnet $Tm_3Al_5O_{12}$ phase (PDF [00-017-0734]) was obtained after annealing of Tm-Al-O:Eu precursors at 1000 °C. In Fig. 13 (c) the X-ray diffraction patterns of the final Yb-Al-O ceramic samples annealed at 1000 °C are presented. The XRD patterns prove the formation of the monophasic cubic ytterbium aluminium garnets ($Yb_3Al_5O_{12}$). Evidently, the obtained XRD patterns are in a good agreement with the reference data for $Yb_3Al_5O_{12}$ (PDF

[01-073-1369]). In Fig. 13 (d) presented XRD patterns confirm the formation of single-phase $Lu_3Al_5O_{12}$ (PDF [01-073-1368]). Fig. 14 shows the dependence of crystallinity of garnet phase on the annealing atmosphere.

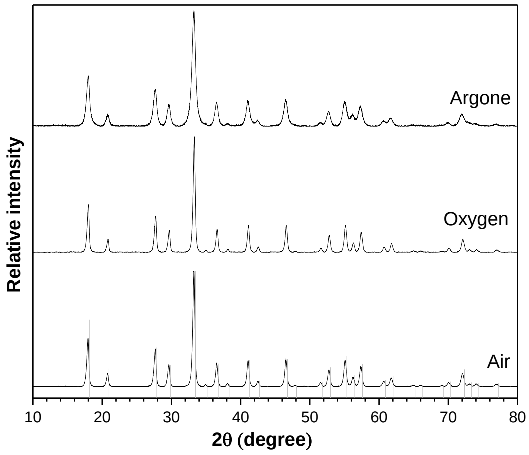

Fig. 14. XRD patterns of the $Er_3Al_5O_{12}$:Eu samples annealed at 1000 °C in differen atmospheres. Vertical lines represent the standard XRD pattern of ErAG.

As seen, high crystalline $Er_3Al_5O_{12}$:Eu samples have formed in air and oxygen atmospheres. However, the broad reflections are seen in the XRD patterns for the sample obtained in argon atmosphere.

The FTIR spectra (Fig. 15) of synthesized garnets show several quite intense broad bands at 693 cm^{-1}, 729 cm^{-1} and 795 cm^{-1} as in the FTIR spectra of TAG:Eu, DAG:Eu and HAG:Eu (previous section), which are typical metal-oxygen (M-O) absorptions for the garnet-type compounds[97,157]. The most important feature remain the same in the region of 900–450 cm^{-1}, which is also attributed to the stretching modes of the isolated [AlO_4] tetrahedra and [AlO_6] octahedra in the garnet structure. The observed M–O vibrations which are characteristic of RE–O and Al–O stretching frequencies let us to conclude that the FTIR results are consistent with crystallization process observed by XRD measurements[158, 159,160,161,162].

The textural properties of the $Er_3Al_5O_{12}$:Eu, $Tm_3Al_5O_{12}$:Eu, $Yb_3Al_5O_{12}$:Eu and $Lu_3Al_5O_{12}$:Eu powders were investigated by TEM.

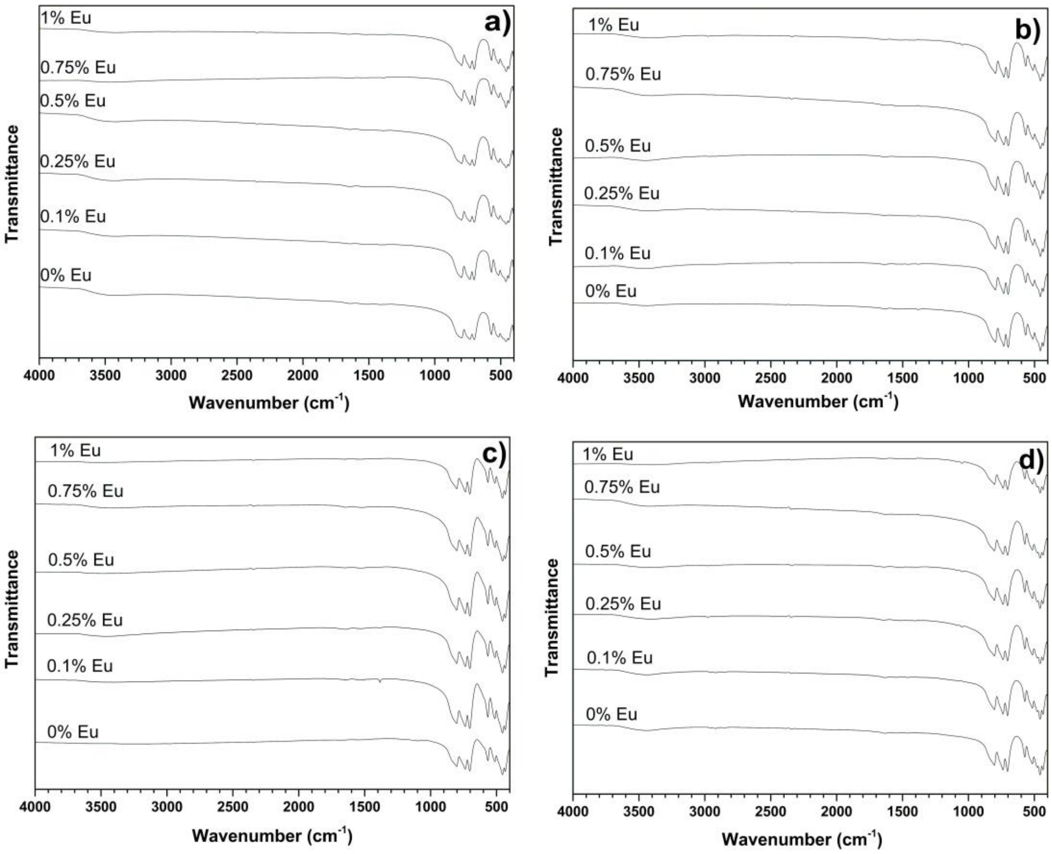

Fig. 15. FTIR spectra of $Er_3Al_5O_{12}$:Eu (a), $Tm_3Al_5O_{12}$:Eu (b), $Yb_3Al_5O_{12}$:Eu (c) and $Lu_3Al_5O_{12}$:Eu (d) garnets synthesized at 1000 °C.

The TEM micrographs of these garnet samples are shown in Fig. 16-19. The TEM images of $Er_3Al_5O_{12}$:Eu samples presented in Fig. 16 show the formation of very homogeneous mixed-metal garnets. Individual oblong particles are nano-sized and partially fused to form hard agglomerates. It is known, however, that the phosphors with irregularly shaped particles could decrease screen brightness and resolution[168]. Evidently, the agglomeration increases with increasing doping level of Eu^{3+}. The thulium aluminum garnets are less agglomerated comparing with erbium aluminum garnet (Fig. 17). Besides, the formation of associated particles with increasing dopant concentration is less pronounced for the $Tm_3Al_5O_{12}$:Eu samples. The microstructure of ytterbium aluminum garnets (Fig. 18) is very similar to the determined for $Tm_3Al_5O_{12}$:Eu garnets. However, the small clusters consist mostly nano-sized spherically shaped particles.

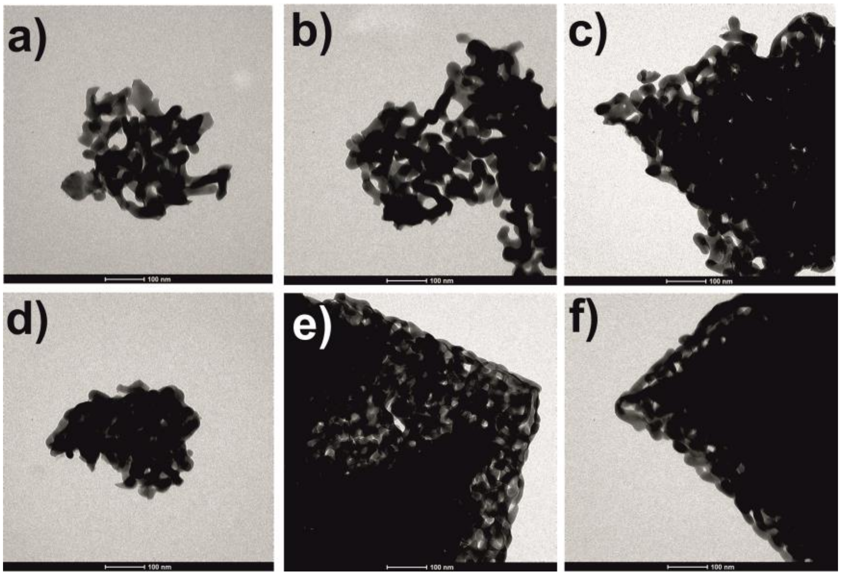

Fig. 16. TEM micrographs of $Er_3Al_5O_{12}$:Eu garnets (0% Eu (a), 0.1% Eu (b), 0.25% Eu (c), 0.5% Eu (d), 0.75% Eu (e), 1% Eu (f)).

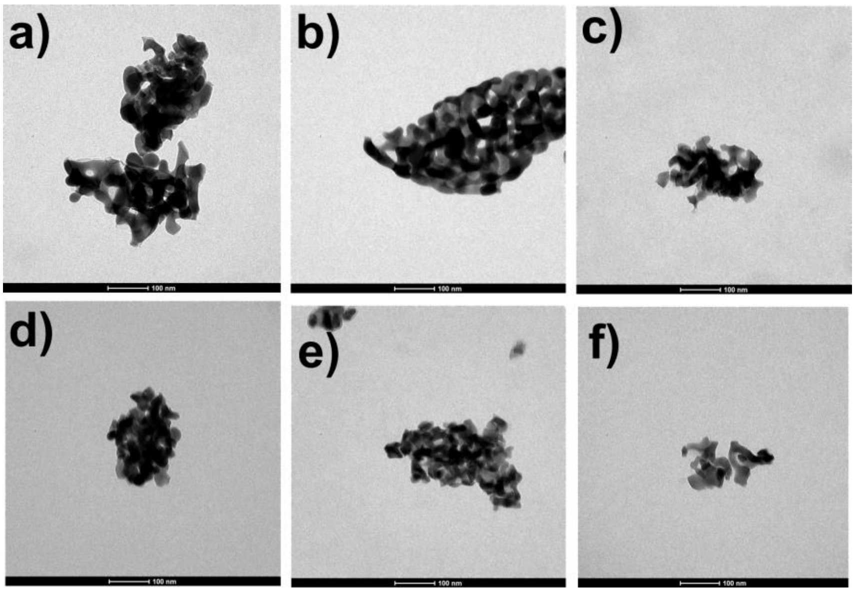

Fig. 17. TEM micrographs of $Tm_3Al_5O_{12}$:Eu garnets (0% Eu (a), 0.1% Eu (b), 0.25% Eu (c), 0.5% Eu (d), 0.75% Eu (e), 1% Eu (f)).

The highest level of particles agglomeration which does not depend on the dopant concentration is observed for the $Lu_3Al_5O_{12}$:Eu samples (Fig. 19). TEM images of $Er_3Al_5O_{12}$:1% Eu sample obtained in different atmospheres are shown in Fig. 20. The TEM results show that annealing atmosphere influences the level of agglomeration of final product. As seen, the rate of agglomeration could be laid in the following line: air > argone > oxygen.

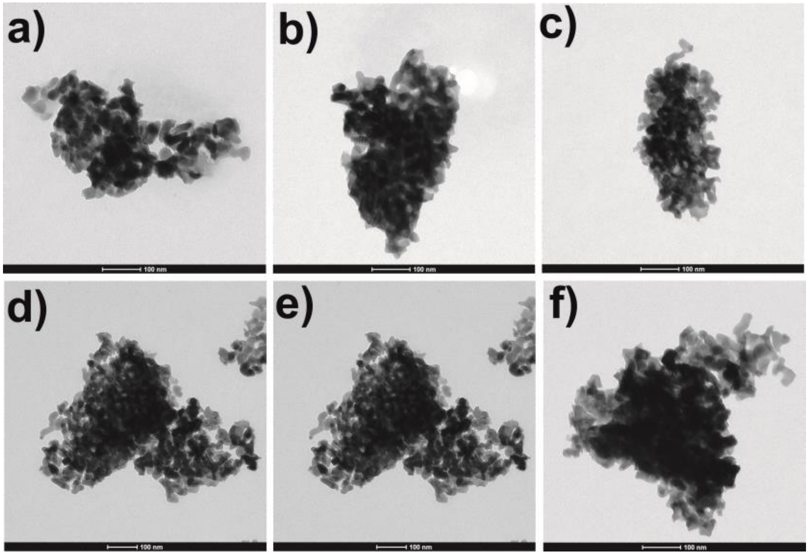

Fig. 18. TEM micrographs of $Yb_3Al_5O_{12}$:Eu garnets (0% Eu (a), 0.1% Eu (b), 0.25% Eu (c), 0.5% Eu (d), 0.75% Eu (e), 1% Eu (f)).

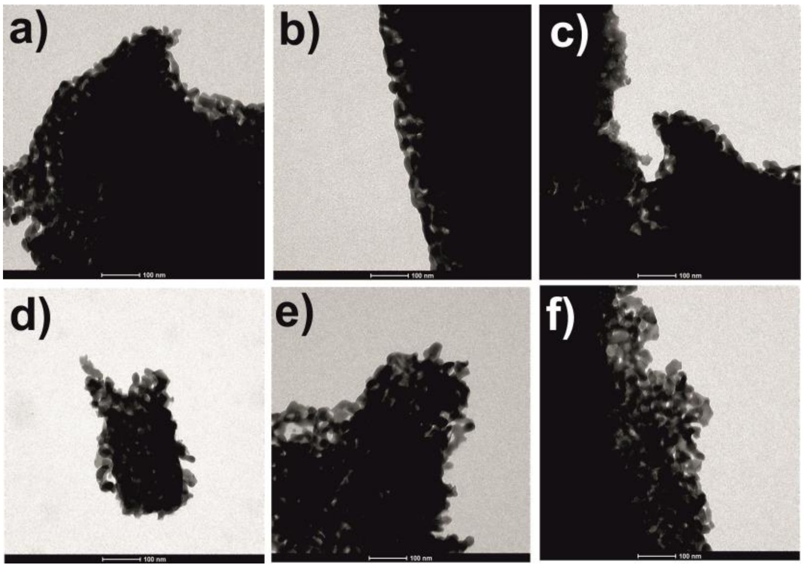

Fig. 19. TEM micrographs of $Lu_3Al_5O_{12}$:Eu garnets (0% Eu (a), 0.1% Eu (b), 0.25% Eu (c), 0.5% Eu (d), 0.75% Eu (e), 1% Eu (f)).

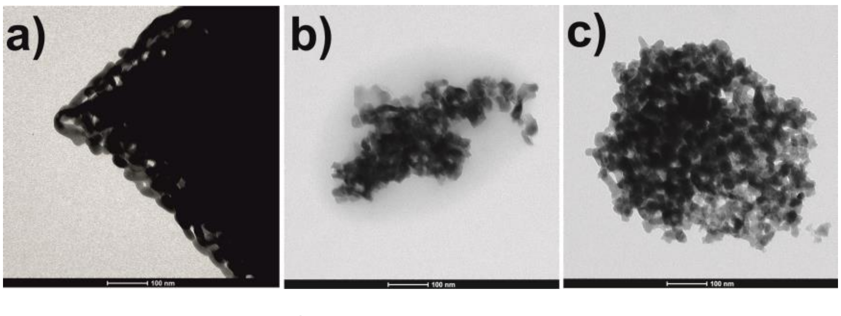

Fig. 20. TEM micrographs of $Er_3Al_5O_{12}$:1%Eu sample obtained in different atmospheres: air (a), oxygen (b) and argone (c).

Eu^{3+}, Lu^{3+} and Yb^{3+} ions occupy the same dodecahedral interstices in the lanthanide aluminium garnets. Local environment of these cations could be inspected by solid-state NMR spectroscopy, which uses NMR-active ^{27}Al nuclei as local probes. ^{27}Al MAS NMR spectra of the $Lu_3Al_5O_{12}$:Eu and $Yb_3Al_5O_{12}$:Eu samples are presended in Fig. 21 and 22, respectively.

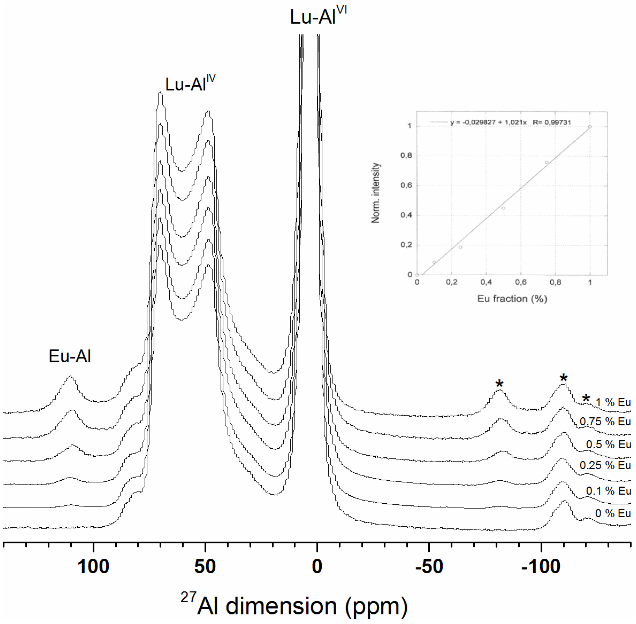

Fig. 21. ^{27}Al MAS NMR spectra of the $Lu_3Al_5O_{12}$:Eu samples. Asterisks denote spinning sidebands.

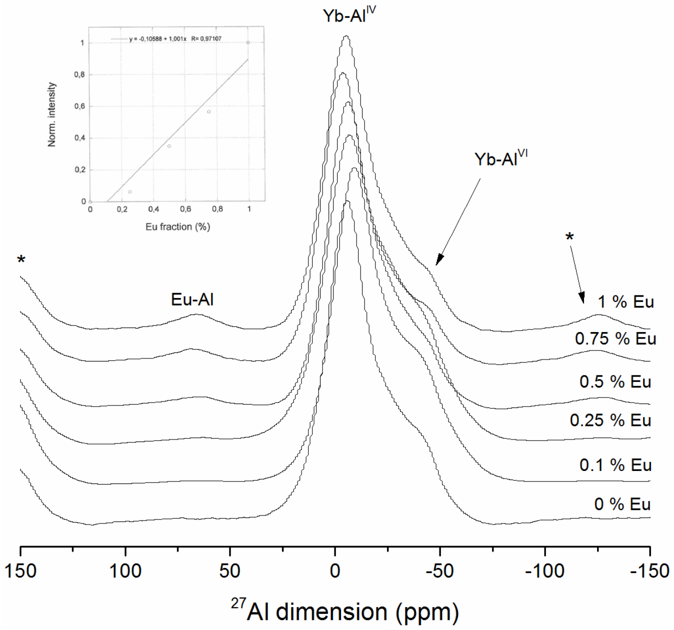

Fig. 22. ^{27}Al MAS NMR spectra of the $Yb_3Al_5O_{12}$:Eu samples.

The signals observed in Fig. 21 at 70 ppm and 48 ppm correspond to Al^{IV} environment (four-coordinated Al site, close to Lu). Signals observed at 3 ppm belong to Al^{VI} environment (six-coordinated Al site close to Lu). At higher concentrations of europium additional peaks at 110 ppm appear. They are assigned to Al^{VI} which is close to Eu environments. Intensities of aluminium signals as a function of Eu^{3+} concentration in the samples are represented in Fig. 21. Solid lines represent the calculated integral intensities after fitting the overlapping contour using multiple Voigt profile for the random spatial distribution of Eu^{3+} ions along the crystal lattice. A simple calculation of expected aluminium intensities based on probabilities for a normal distribution shows a very nice agreement with the experimentally detected intensities and thus reveals that the Eu^{3+} ions are randomly dispersed throughout the crystal lattice of LuAG:Eu.

^{27}Al MAS NMR spectra of the $Yb_3Al_5O_{12}$:Eu a placed in Fig. 22. The most intensive peak observed at -5 ppm is atributed to Al^{IV} which close to ytterbium in lanthanide aluminum garnet lattice. Another not very clear visible and coverlapped bands at - 44 ppm corespond to Al^{VI} also closed to ytterbium ion. Eu-Al^{VI} band at 65 ppm could be observed only at the concentrations of Eu^{3+} higher than 0.5%. Intensities of aluminium signals as a function of Eu^{3+} concentration in the samples increase proportionally with increasing amount of Eu^{3+}. ^{27}Al MAS NMR spectroscopy data confirm efective doping of Eu ion in the lanthanide aluminum lattice.

It was not possible to recoord ^{27}Al MAS NMR spectra of $Er_3Al_5O_{12}$:Eu and $Yb_3Al_5O_{12}$:Eu aluminium garnets because of strong characteristic paramagnetic properties.

3.2.2. Optical properties

During photoluminescence the emission spectra were measured at room temperature under 394 nm excitation and excitationn spectra under 590 nm emission for europium. The excitation and emission spectra of LuAG:Eu samples are shown in Fig 23. Several peaks in the region of 250-530 nm corresponding to the 4f→4f transitions within Eu^{3+} $4f^6$ configuration are observed in the excitation spectra. The most efficient and intensive line is located at 394 nm which corespond to the $^7F_0 \rightarrow ^5L_6$ transition. The emission peaks found at 591 nm, 594 nm, 609 nm, 630 nm, 648-662 nm, 696 nm, 701 nm, 709 nm, 716 nm and 744 nm are in a good agreement with the reported values of Eu^{3+} emission transitions[165,169,170]. The emission spectra are composed of $^5D_0 \rightarrow ^7F_J$ lines of Eu^{3+} dominated by the $^5D_0 \rightarrow ^7F_1$ (590 nm) magnetic-dipole transition. In cubic LuAG phase, the Lu^{3+} is coordinated by eight oxygen ions with D2 point symmetry. However, the exact local symmetry of doped Eu^{3+} is only a small distortion of D2h point symmetry, which is centrosymmetric[171]. As a result, the luminescent intensity is concentrated mainly on the $^5D_0 \rightarrow ^7F_1$ magnetic dipole transition. The peak at 590 nm has a small full width at half maximum (FWHM) which indicating high purity and crystallinity of the phosphor particles[172]**.** The spectra also shows the characteristic emission of Eu^{3+} arising due to $^5D_0 \rightarrow ^7F_2$ (611 nm) and $^5D_0 \rightarrow ^7F_4$ (708 nm) transitions[50]. The $^5D_0 \rightarrow ^7F_2$ band is attributed to the forced electric-dipole transition allowed only at low symmetries with no inversion center[173,174]. It is also a hypersensitive transition and found to be very sensitive to the local structure surrounding the Eu^{3+} ions.

$Er_3Al_5O_{12}$ and $Tm_3Al_5O_{12}$ garnets doped with Eu^{3+} ion do not show any peaks in the luminescence spectra. Usually, the activator concentration that governs the distance between the two neighboring activator ions has a great impact on the emission intensities in a RE ion doped nanocrystalline host lattice. With increasing the doping concentration of co-activator ions, the energy transfer from the higher energy level of the donor to the next lower energy level of the acceptor increases and the cross-relaxation process may occur between the adjacent dopant ions at higher doping concentrations[175,176]. In this case (Er-Al-O, Tm-Al-O) these elements (Eu^{3+}, Er^{3+}, Tm^{3+}) can be excited under similar excitation wavelength. So, both energy transfer and the cross-relaxation processes occurred between Tm^{3+}– Eu^{3+}, and Er^{3+}– Eu^{3+}. The energy transfer process occurred between the Tm^{3+} and Eu^{3+} ions from the excited $^1D_2$ level of the Tm^{3+} ions to the excited $^5D_4$ level of the Eu^{3+} ions.

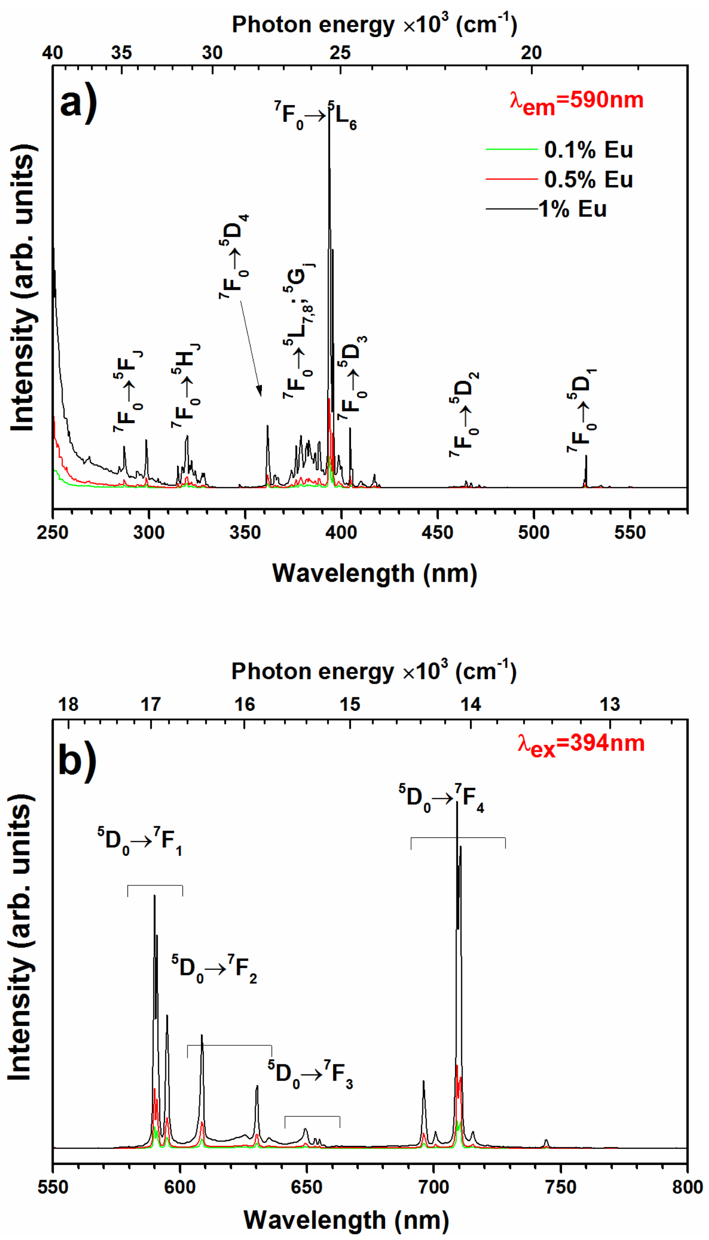

Fig. 23. Excitation (a) and emission (b) spectra of the $Lu_3Al_5O_{12}$:Eu samples.

The Eu^{3+} ions were relaxed nonradiatively down to the $^5D_1$ and $^5D_0$ metastable states[175]. In a similar way, the excited $^4G_{9/2}$ level of Er^{3+} ions is closer to the $^5G_2$ level of the Eu^{3+} ions.Therefore, when excited under similar excitation wavelength, the Er^{3+} ions have been excited to the $^4G_{9/2}$ level and these ions transfer some of the excitation energy to the next lower level of the Eu^{3+} ($^5G_2$) ions. Then, they were relaxed nonradiatively to metastable states of Er^{3+} and Eu^{3+}. Note that if the energy transfer occurred between the metastable state of Tm^{3+}–Eu^{3+}, the emission intensity of $^5D_0 \rightarrow {}^7F_J$ transitions of Eu^{3+} ions is very high, which is enough clarification for the way of energy transfer identification from Tm^{3+} or Er^{3+} to Eu^{3+} ions. Because of the hypersensitive nature of the $^5D_0 \rightarrow {}^7F_2$ transition, other interesting features of this process such as the cross-relaxation due to the resonance energy transfer between the adjacent dopant ions were observed. The crossrelaxation process stimulated the quenching of excitation energy and thereby decreased emission intensities of Tm^{3+}, Er^{3+}, and Eu^{3+} in the blue, green, and red regions.The possible cross-relaxation ways between Tm^{3+}–Eu^{3+}, and Er^{3+}–Eu^{3+} pairs are:

$$^3H_4\,(Tm^{3+}) + {}^7F_0\,(Eu^{3+}) \rightarrow {}^3H_5\,(Tm^{3+}) + {}^7F_5\,(Eu^{3+}) \qquad (7)$$

$$^4I_{11/2}\,(Er^{3+}) + {}^7F_0\,(Eu^{3+}) \rightarrow {}^4I_{13/2}\,(Er^{3+}) + {}^7F_4\,(Eu^{3+}) \qquad (8)$$

In these undesirable cross-relaxation processes, the excitation energy absorbed by the Tm^{3+} or Er^{3+} ions can be transferred to the ^7F_J levels of the nearest Eu_{3+} ions and then dissipated nonradiatively as heat. As a result, required emission intensities of Tm^{3+}, Er^{3+} and Eu^{3+} emissions are missed. Therefore, it should be noted that the cross-relaxation process is dominant rather than the energy transfer process.

$Yb_3Al_5O_{12}$:Eu garnets also do not show any absorbtion and emission peaks in the spectra. There are few cases in the literature about these luminescent ions (Yb^{3+} and Eu^{3+}) composition and they could explain why the luminescence wasn’t observed. L. Wang et all[177] reports that using Yb^{3+} and Er^{3+} as double sensitizers and 980 nm laser as pump light, unusual radiative transitions $^5H_{3–7} \rightarrow {}^7F_{0–3}$, $^5L_6 \rightarrow {}^7F_0$, $^5D_3 \rightarrow {}^7F_{2,3}$, and $^5D_2 \rightarrow {}^7F_{0,1,2,3}$ of Eu^{3+} ions in $NaYF_4$ nanocrystals were observed. $^5H_{3–7}$, $^5L_6$, and $^5D_{2,3}$ levels of Eu^{3+} have been populated by two-step energy transfer process of $Yb^{3+} \rightarrow Er^{3+} \rightarrow Eu^{3+}$ and become efficient radiative levels in the upconversion scheme. Y. Wang et al.[178] compared emission of $La_{0.3}Y_{2.7}Sc_2Ga_3O_{12}$:Er and $La_{0.3}Y_{2.7}Sc_2Ga_3O_{12}$:Yb,Er,Eu where presence of Yb^{3+}, Eu^{3+} and La^{3+} ions enhanced emission doubly in Yb,Er,Eu:LaYSGG. The energy transfer efficiencies of Yb^{3+}-Er^{3+} (ET1) and Er^{3+}-Eu^{3+} (ET2) in $La_{0.3}Y_{2.7}Sc_2Ga_3O_{12}$:Yb,Er,Eu crystal are estimated to be 94.8% and 93.9%, respectively. These results indicate that the codopant Yb^{3+} and Eu^{3+} ions are beneficial. There was published an article by Pandey et al.[179] where cubic structured Eu^{3+}, Yb^{3+} codoped Y_2O_3 phosphors synthesized by low temperature combustion technique successfully. Where the study of upconversion emission observed from the synthesized phosphor by 980 nm excitation support the possibility of cooperative energy transfer from Yb^{3+} to Eu^{3+} ions. In our case in $Yb_3Al_5O_{12}$:Eu garnets didn't appear this transition and the reason could be quenching of Yb^{3+} form lattice.

3.3. Solvothermal Synthesis and Characterization of Eu^{3+}-doped Holmium Aluminium Garnet

In this part of dissertation Eu^{3+}-doped holmium aluminium garnet ($Ho_3Al_5O_{12}$, HoAG) has been synthesized by solvothermal method and annealed at various temperatures. The XRD patterns of the holmium aluminium garnet synthesized solvothermally at 220 °C and annealed at different temperatures are shown in Fig. 24.

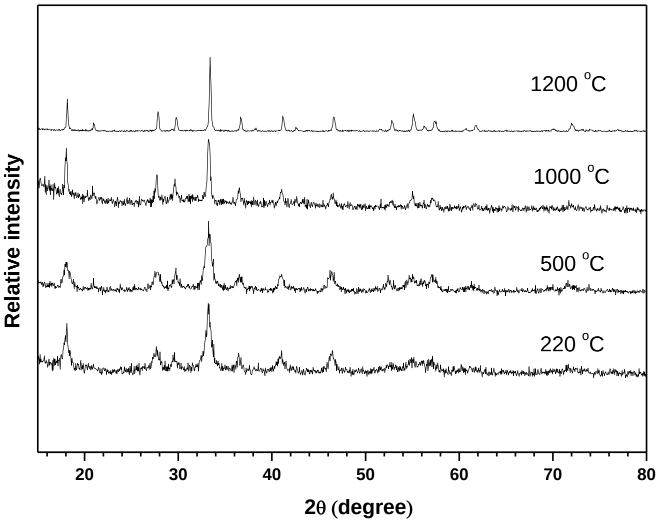

Fig. 24. XRD patterns of solvothermally derived holmium aluminium garnet powders and calcined at different temperatures. $Ho_3Al_5O_{12}$ PDF [04-001-9715])

Fig. 24 clearly shows that the product obtained at 220 °C (20 h heating) is well-crystalized, and all diffraction lines could be attributed to holmium aluminium garnet (PDF [04-001-9715]) crystalline phase. Interestingly, the XRD pattern of the HoAG sample additionally heated at 500 ^{o}C for 4 h is almost identical to that of just synthesized in autoclave specimen. With further heating of the HoAG at higher temperatures (1000 ^{o}C for 10 h and 1200 ^{o}C for 4 h) the intensity of the HoAG diffraction peaks increases and the full-width at half-maximum decreases due to the growth of particles and improved crystallinity of the samples.

As seen from Fig. 25, solvothermally synthesized HoAG:Eu garnet samples are also monophasic compounds. Apparently, europium does not affect the formation of garnet structure up to concentration of 5%. No any new peaks or/and any shifted peaks could be determined in the XRD patterns of differently Eu^{3+}- doped holmium aluminium garnets.

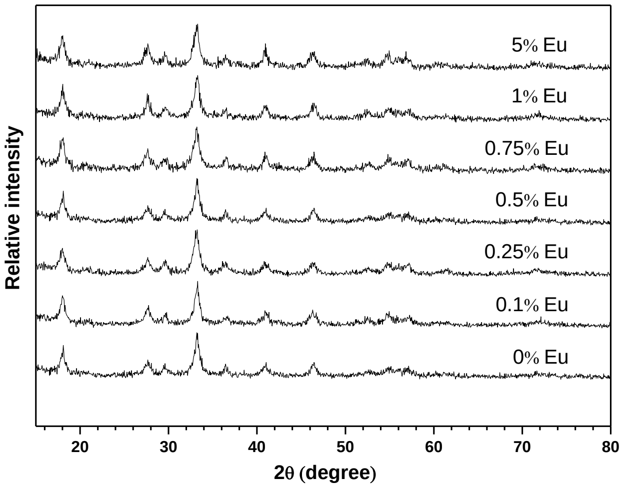

Fig. 25. XRD patterns of HoAG samples doped with different amount of europium ions and synthesized by solvothermal method at 220 $^{\circ}$C for 20 h. $Ho_3Al_5O_{12}$ PDF [04-001-9715])

The particle size and its distribution in $Ho_3Al_5O_{12}$ garnets synthesized at 220 ^{o}C and annealed at different temperatures were investigated by dynamic light scattering (DLS). Fig. 26 shows high influence of annealing temperature on the particle size of HoAG.

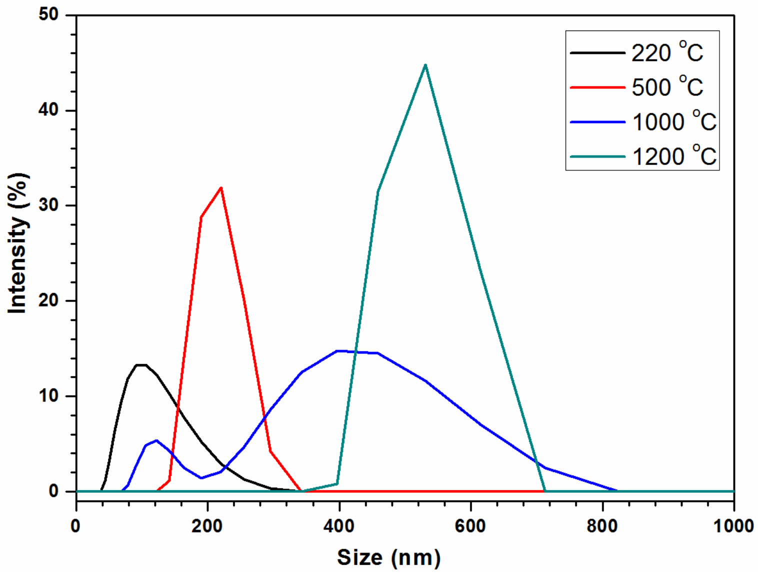

Fig. 26. Particle size and its distribution of HoAG samples obtained at different temperatures.

As seen, nanoparticles of HoAG (~100 nm) with narrow particle size distribution have formed during solvothermal synthesis at 220 °C. The particles of ~220 nm in size have formed after heating the solvothermally obtained sample at 500 °C. With increasing the heating temperature till 1000 °C the largest fraction of HoAG is composed of ~410 nm particles. The largest particles were determined for the HoAG sample annealed at 1200 °C. Thus, the particle size of HoAG synthesized using solvothermal method monotonically increases from 100 nm to 600 nm with increasing annealing temperature. The particle size distribution becomes also broader with increasing the heating temperature.

The textural properties of HoAG powders were investigated by SEM, from which the grain size and typical morphologies were obtained. Scanning electron micrographs of the HoAG and HoAG:Eu samples are shown in Fig. 27. The SEM results are in a good agreement with those obtained by DLS measurements. The even increase of particle size of HoAG with increasing the heating temperature is evident. As synthesized at 220 °C HoAG is composed mainly of well-distributed fine spherical grains (less than 100 nm). The SEM image of HoAG:Eu sample annealed at 500 °C at first glance looks very similar, however, the connectivity between grains is less pronounced. The

HoAG and HoAG:Eu specimens annealed at 1200 °C are obviously composed of largest and agglomerated spherical particles.

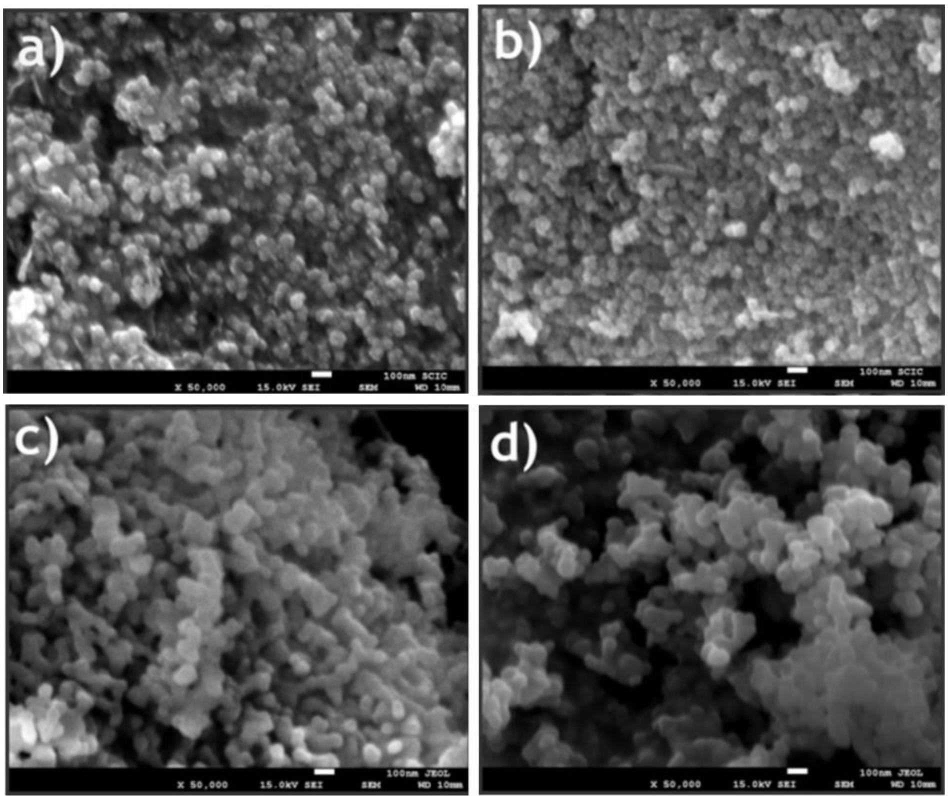

Fig. 27. SEM micrographs of HoAG synthesized at 220 °C (a), HoAG:0.25%Eu annealed at 500 °C (b), HoAG annealed at 1200 °C (c) and HoAG:0.25%Eu annealed at 1200 °C (d).

3.4. Sol-Gel Synthesis and Characterization of Eu^{3+}-doped $Y_{3-x}Nd_xAl_5O_{12}$ Garnet

In this part of dissertation the YAG samples doped with different amount of Nd^{3+} and YAG:Nd garnets with various doping levels of europium were synthesized by sol-gel method and investigated.

3.4.1. XRD, FTIR, SEM, NMR and Raman analyses

The XRD patterns of corresponding $Y_{3-x}Nd_xAl_5O_{12}$, $Y_{2.9}Nd_{0.1}Al_5O_{12}$:Eu and $Y_{3-x}Nd_xAl_5O_{12}$:0.5% Eu powders annealed at 1000 °C are shown in Fig. 28. The XRD results presented in Fig. 28 (a) revealed that neodymium doped garnet samples obtained at 1000 °C consists of one YAG crystalline phase in whole investigated substitutional range. The obtained XRD patterns are in a good agreement with the reference data for $Y_3Al_5O_{12}$. Besides, the XRD patterns showed that these garnets were the only phase detected in the end products. The XRD patterns shown in Fig. 28 (b,c) also confirmed the formation of cubic structure in $Y_{2.9}Nd_{0.1}Al_5O_{12}$:Eu and $Y_{3-x}Nd_xAl_5O_{12}$:0.5% Eu garnets, respectively. All XRD patterns match with reference data and do not show any influence of dopants on the formation of garnet crystalline structure.

The Nd^{3+} and Eu^{3+} ions incorporated in the lattice both substitute the Y^{3+} ions. The small increase in the lattice parameter for the Eu^{3+} doped samples compared to the undoped one has been attributed to the larger ionic radius of Eu^{3+} (1.095 Å) compared to Y^{3+} ions (1.053 Å)[36,180].

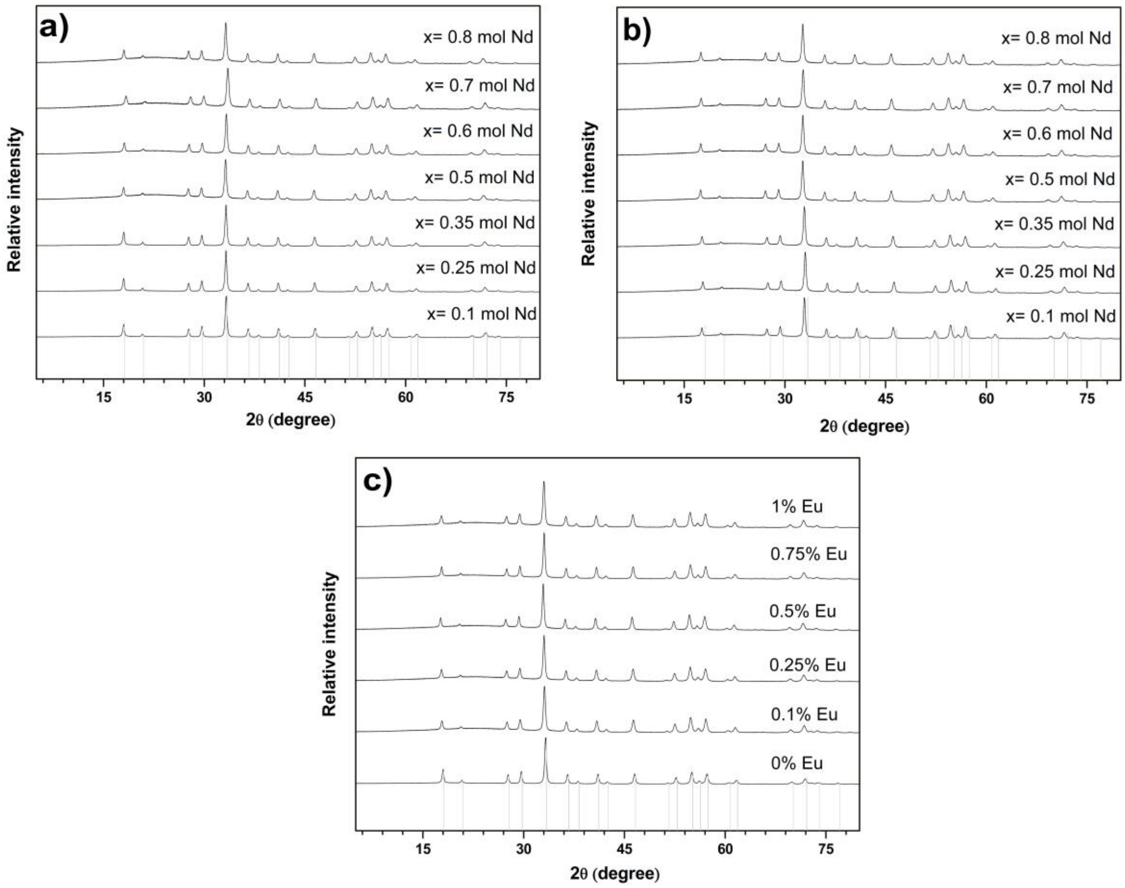

Fig. 28. XRD patterns of the $Y_3Al_5O_{12}$:Nd (a), $Y_{3-x}Nd_xAl_5O_{12}$:0.5% (b), $Y_{2.9}Nd_{0.1}Al_5O_{12}$:Eu (c) samples annealed at 1000 °C for 10 h. Vertical lines represent the standard XRD pattern of YAG. $Y_3Al_5O_{12}$ [PDF 88-2048].

Moreover, a small decrease should appear in garnet lattice doped with Nd^{3+} ion (0.980 Å)[181]. On the other hand, the garnet co-doped with both ions (Nd^{3+} and Eu^{3+}) may not have very different lattice parameter from the undoped one, because larger and smaller ionic radius are compensated in an average image that XRD measurement can offer. Comparing with reference data, our synthesized garnets show almost the same lattice parameters as standard $Y_3Al_5O_{12}$ [PDF 88-2048].

The FTIR spectra Y-Al-O:Nd,Eu precursor gels annealed at 1000 °C for 10 h are shown in Fig. 29. As seen all FTIR spectra are almost identical showing a high reproducibility of the used sol-gel processing. The observed M–O vibrations let us conclude that FTIR results are consistent with the crystallization process observed by XRD measurements.

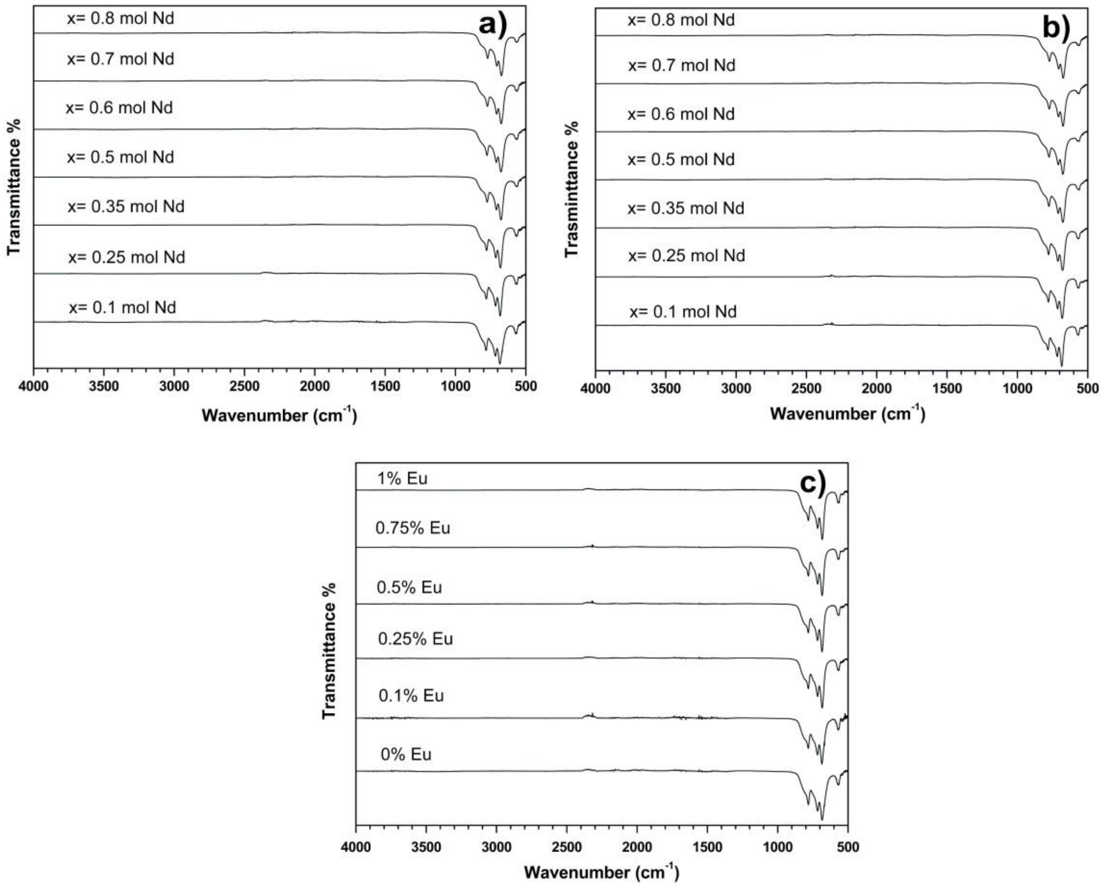

Fig. 29. FTIR spectra of the $Y_{3-x}Nd_xAl_5O_{12}$ (a), $Y_{3-x}Nd_xAl_5O_{12}$:0.5%Eu (b) $Y_{2.9}Nd_{0.1}Al_5O_{12}$:Eu (c) samples annealed at 1000 °C for 10 h.

The textural properties of the $Y_{3-x}Nd_xAl_5O_{12}$, $Y_{2.9}Nd_{0.1}Al_5O_{12}$:Eu and $Y_{3-x}Nd_xAl_5O_{12}$:Eu powders were investigated by SEM. SEM micrographs of the $Y_{2.9}Nd_{0.1}Al_5O_{12}$:Eu garnet samples are shown in Fig. 30. The SEM micrographs show the formation of very homogeneous surface, and individual particles seem to be nano-sized spherically shaped particles forming hard agglomerates. The microstructure of $Y_{3-x}Nd_xAl_5O_{12}$ (Fig. 31) and $Y_{3-x}Nd_xAl_5O_{12}$:Eu (Fig. 32) samples is very similar indicating that particle size and shape are not influenced by lanthanides and their concentration. Apparently, the particles of all sol-gel derived garnet samples were formed with pronounced agglomeration, indicating good connectivity between the grains[157].

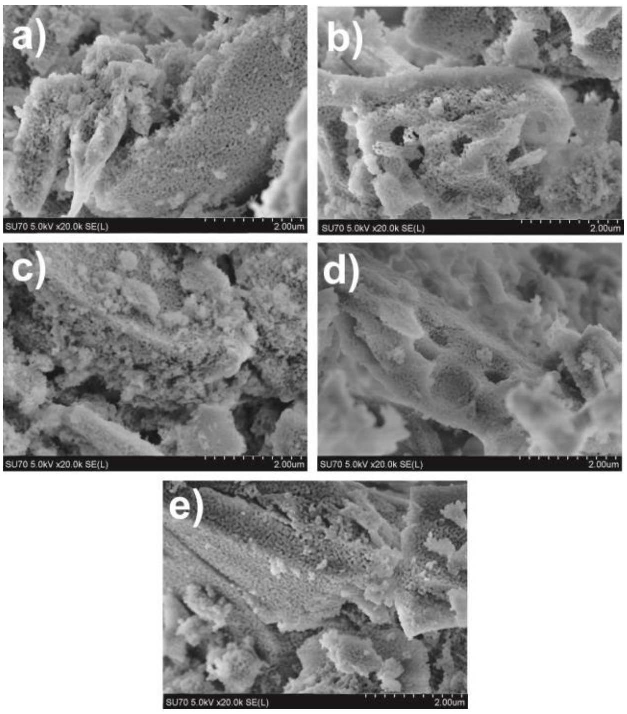

Fig. 30. SEM micrographs of $Y_{2.9}Nd_{0.1}Al_5O_{12}$:Eu garnets (Eu: 0.1% (a); 0.25% (b); 0.5% (c); 0.75% (d); 1% (f)).

In non-doped $Y_3Al_5O_{12}$, yttrium cations reside in the dodecahedral interstices formed by the network of corner-sharing AlO_4 and AlO_6 polyhedra[5,182,183]. Since it is expected that Eu^{3+} and Nd^{3+} ions will occupy the same dodecahedral interstices, local environment of these cations could be inspected by solid-state NMR spectroscopy, which uses NMR-active ^{27}Al

nuclei as local probes. Indeed, the resonance frequency of ^{27}Al nuclei that are close to the Nd^{3+} substituent ions is shifted to lower values compared to the resonance frequency of ^{27}Al nuclei that have only Y^{3+} ions nearby (Fig. 33). This is a result of a through-bond hyperfine interaction and through-space anisotropic dipolar interaction between the unpaired Nd^{3+} 4*f* electronic spins and the ^{27}Al nuclear spins[184].

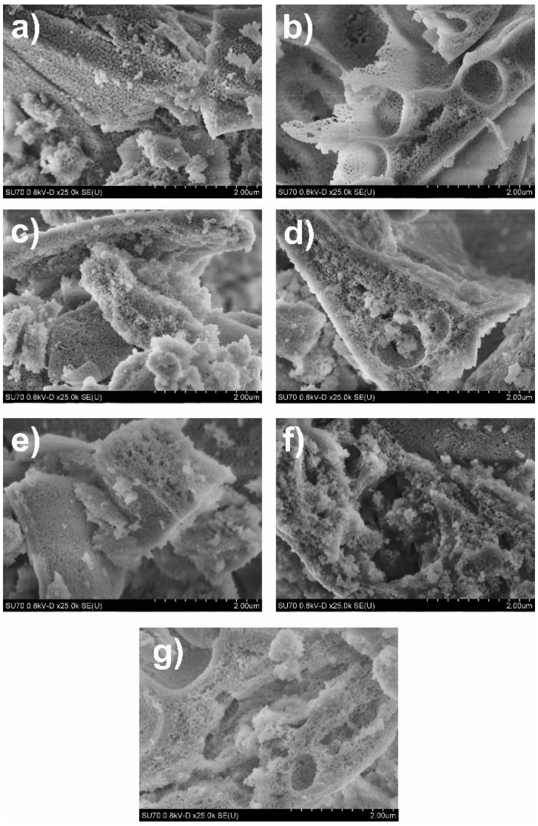

Fig. 31. SEM micrographs of $Y_{3-x}Nd_xAl_5O_{12}$ garnets (0.1 (a); 0.25 (b); 0.35 (c); 0.5 (d); 0.6 (e); 0.7 (f); 0.8 (g)).

A closer look at ^{27}Al MAS NMR spectra shows that at low concentrations of Nd^{3+} in the samples, two major ^{27}Al signals at 68 ppm and 0 ppm can be observed (Fig. 33 (a), 34-37). The observed signals correspond to four- and six-coordinated aluminium atoms, respectively. The four-coordinated Al^{IV} atoms are surrounded by two yttrium ions at a distance of about 3.0 Å, and by additional four yttrium ions at about 3.7 Å. This gives rise to a relatively large electric field gradient at the position of Al^{IV} nuclei and thus to a rather broad peak. The six-coordinated Al^{VI} atoms reside in a much more symmetrical environment. They are surrounded by six equidistant yttrium ions at a distance of 3.35 Å, which leads to small value of the electric field gradient. As a result, the Al^{VI} peak is narrow and well resolved. In addition to the two strong peaks, two weaker peaks resonating at 43 ppm and -63 ppm can be observed in the ^{27}Al MAS NMR spectra.

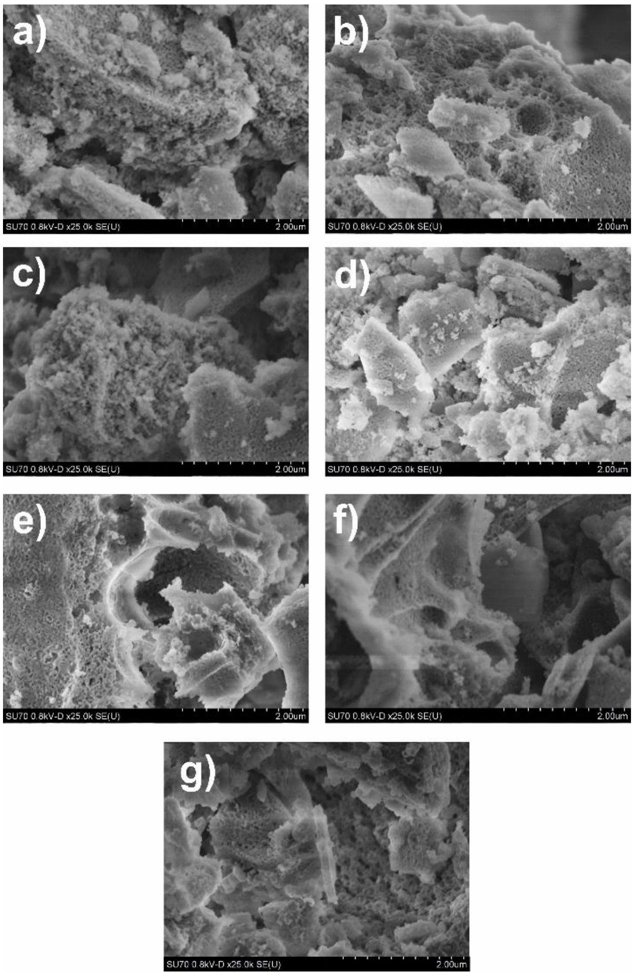

Fig. 32. SEM micrographs of $Y_{3-x}Nd_xAl_5O_{12}$:0.5%Eu garnets (0.1 (a); 0.25 (b); 0.35 (c); 0.5 (d); 0.6 (e); 0.7 (f); 0.8 (g)).

The latter two peaks can be assigned respectively to Al^{IV} and Al^{VI} atoms with one neodimium cation in their first cation coordination shells (Al^{IV}(1Nd) and Al^{VI}(1Nd)). These peaks already confirm the proximity of Al and Nd within the YAG:Nd,Eu materials. At high Nd^{3+} concentration (e.g. $x = 0.8$), additional peaks appear at -127 ppm and -192 ppm. The paramagnetic shifts are additive with the number of proximal Nd^{3+} ions, so these peaks can be attributed to the Al^{VI} nuclei that have two and three Nd^{3+} ions in their first cation coordination shell, respectively. Their intensities increase with the increasing amount of neodymium. Al^{IV} nuclei with two and three neodymium ions nearby are expected to resonate at 18 ppm and -7 ppm, respectively. This is very close to the strong peak of Al^{VI} atoms surrounded only by yttrium ions, which is why the two weak peaks cannot be resolved.

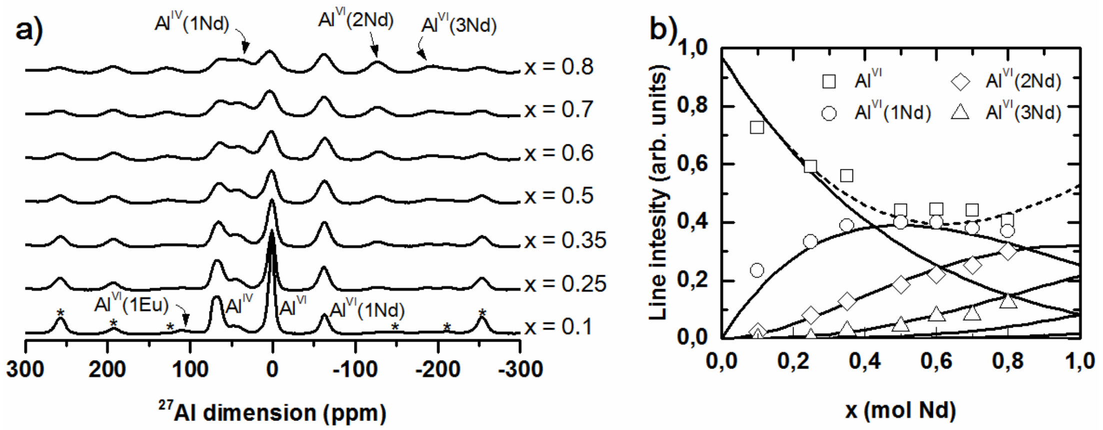

Fig. 33. (a) ^{27}Al MAS NMR spectra of the $Y_{3-x}Nd_xAl_5O_{12}$:0.5%Eu samples. The signals at 43 ppm and -63 ppm belong to Al^{IV}(1Nd) and Al^{VI}(1Nd) environments, i.e. to four- and sixcoordinated Al sites with one Nd^{3+} cation in their vicinity. At high neodymium concentrations additional peaks at -127 ppm and -192 appear ppm. They are assigned to Al^{VI}(2Nd) and Al^{VI}(3Nd) environments, respectively. Asterisks denote spinning sidebands. (b) Intensities of different aluminum signals as a function of concentration of Nd in the samples. Solid lines represent calculated intensities for the random spatial distribution of Nd^{3+} ions along the crystal lattice. The discrepancy between the Al^{VI} data points and the corresponding calculated line is a consequence of overlapping Al^{VI}, Al^{IV}(2Nd) and Al^{IV}(3Nd) signals; the calculated sum of all three contributions is presented with a dashed line and agrees well with the experimental data.

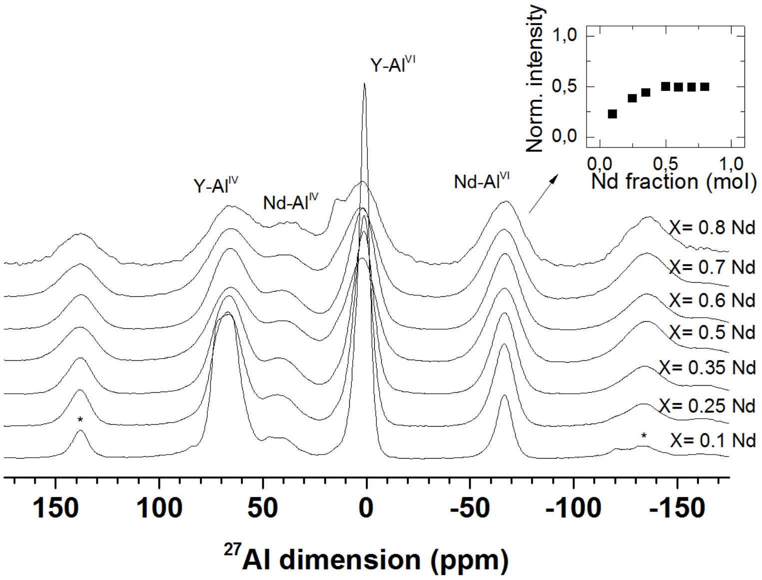

Fig. 34. ^{27}Al NMR spectra of $Y_{3-x}Nd_xAl_5O_{12}$ samples.

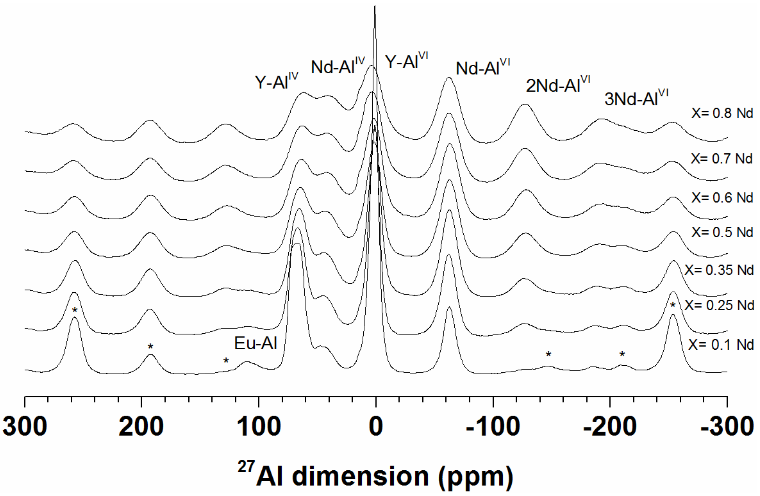

Fig. 35. ^{27}Al NMR spectra of the $Y_{3-x}Nd_xAl_5O_{12}$:0.5%Eu samples.

A simple calculation of expected aluminium intensities based on probabilities for a normal distribution shows a very nice agreement with the experimentally detected intensities and thus reveales that the Nd^{3+} ions are randomly dispersed throughout the crystal lattice of YAG:Nd,Eu (Fig. 33 (b)). ^{27}Al MAS NMR also undoubtedly confirms the successful incorporation of europium ions into the crystalline lattice of YAG:Nd,Eu. As Eu^{3+} ion has six unpaired 4*f* electrons, large paramagnetic shift is expected for the closest ^{27}Al nuclei. Indeed, the resonance frequency of Al^{VI} with one europium cation in the neighbourhood is shifted to substantially higher values, i.e. to 113 ppm. We analysed the ^{27}Al peak intensities of $Y_{2.9}Nd_{0.1}Al_5O_{12}$:Eu samples, in which the content of europium varied (Fig. 37). The linear relation between the Al(1Eu) line intensity and the Eu^{3+} indicates that, as for neodimium, the spatial distribution of europium ions in these samples is also homogeneous.

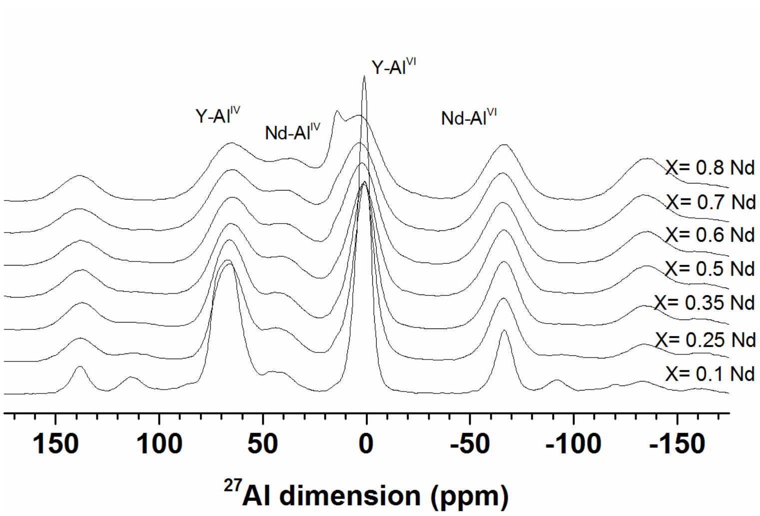

Fig. 36. ^{27}Al NMR spectra of the $Y_{3-x}Nd_xAl_5O_{12}$:1%Eu samples.

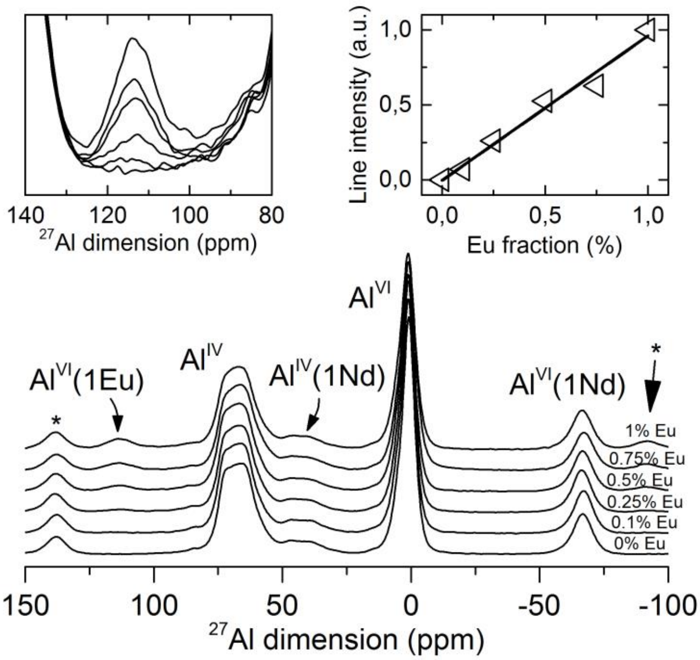

Fig. 37. ^{27}Al MAS NMR spectra of the $Y_{2.9}Nd_{0.1}Al_5O_{12}$:Eu samples with Eu fractions of 0, 0.1, 0.25, 0.5, 0.75 and 1% (from bottom to top), respectively.

Al^{VI}(1Eu) peaks are better seen in the left inset. The right inset shows the linear relation between the Al^{VI}(1Eu) peak intensity and the Eu fraction.

3.4.2. Optical properties

In order to study the doping effect on the luminescence behaviour of the synthesized samples, photoluminescence studies were also carried out. Emission spectra were measured at room temperature under 588 nm excitation for neodymium and under 394 nm excitation for europium. Excitation spectra were recorded monitoring emission at 1064 nm for neodymium and at 591 nm for europium. Excitation and emission spectra of $Y_3Al_5O_{12}$:Nd garnets are shown in Fig. 38.

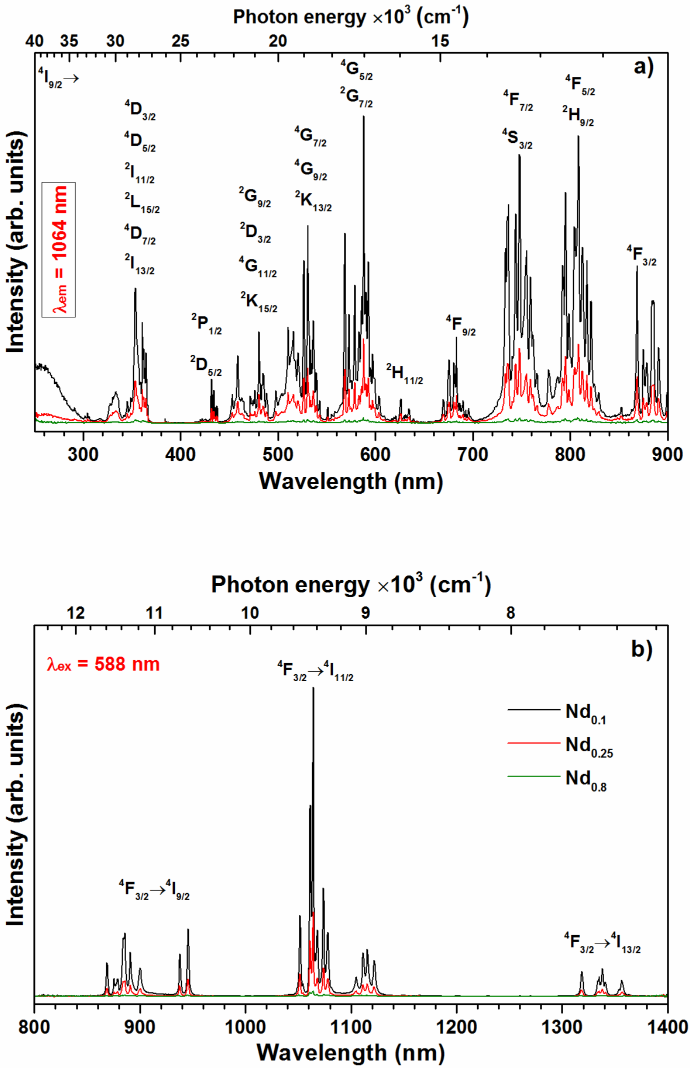

Fig. 38. Excitation (a) and emission (b) spectra of $Y_{3-x}Nd_xAl_5O_{12}$ samples.

Excitation spectra consist of 10 sets of lines at around 380, 430, 470, 520, 580, 630, 680, 750, 810, and 880 nm. These lines originate from intraconfigurational transitions of Nd^{3+} ions from ground state $^4I_{9/2}$ to the excited states, namely, ($^4D_{3/2}$ + $^4D_{5/2}$ + $^2I_{11/2}$ + $^2L_{15/2}$ + $^4D_{7/2}$ + $^2I_{13/2}$), ($^2P_{1/2}$ + $^2D_{5/2}$), ($^2G_{9/2}$ + $^2D_{3/2}$ + $^4G_{11/2}$ + $^2K_{15/2}$), ($^4G_{7/2}$ + $^4G_{9/2}$ + $^2K_{13/2}$), ($^2G_{5/2}$ + $^2G_{7/2}$), ($^2H_{11/2}$), ($^4F_{9/2}$), ($^4F_{7/2}$ + $^4S_{3/2}$), ($^4F_{5/2}$ + $^2H_{9/2}$), and ($^4F_{3/2}$), respectively. The NIR emission spectra comprises several peaks located at 850-950 nm and 1050-1125 nm, which arise due to the $^4F_{3/2} \rightarrow {}^4I_{9/2}$ and $^4F_{3/2} \rightarrow {}^4I_{11/2}$ transitions of Nd^{3+}. Peaks near 1340 nm are attributed to the $^4F_{3/2} \rightarrow {}^4I_{13/2}$ transitions of Nd^{3+} [94,165,185]. As seen, the 0.1 mol Nd-doped sample shows the most intensive luminescence. It is clearly seen that intensity of all peaks increases proportionally with decreasing the doping level of nedymium.

The similar results are also observed for the $Y_{3-x}Nd_xAl_5O_{12}$:0.5%Eu samples (see Fig. 39). However, one can also observe a new set of lines in excitation spectra at around 395 nm. These lines are attributed to the $^7F_0 \rightarrow {}^5L_6$ transition of Eu^{3+} ions. This transition was not observed in samples without europium. All this leads to a conclusion that $Eu^{3+} \rightarrow Nd^{3+}$ energy transfer occurs in samples doped with both ions. Fig. 40 shows excitation and emission spectra of $Y_{2.9}Nd_{0.1}Al_5O_{12}$:Eu. As seen, the phosphor can be effectively excited with 394 nm UV radiation. Excitation was recorded with emission at 591 nm.

The emission peaks found between 550 and 800 nm are in a good agreement with the reported values of Eu^{3+} emission transitions[165,169,170]. The emission spectral lines of Eu^{3+} ion are sharp which is due to the screening of 4f orbital by 5s and 5p orbitals from crystal field of the host lattice. The spectra show the characteristic emission of Eu^{3+} arising due to $^5D_0 \rightarrow {}^7F_1$ (591 nm), $^5D_0 \rightarrow {}^7F_2$ (611 nm) and $^5D_0 \rightarrow {}^7F_4$ (708 nm) transitions[50]. As expected for the Eu^{3+} ions a typical strong red emission was present with the line at 611 nm originated from the $^5D_0 \rightarrow {}^7F_2$ transition. This band is attributed to the forced electric-dipole transition allowed only at low symmetries with no inversion center. It is also a hypersensitive transition and found to be very sensitive to the local structure surrounding the Eu^{3+} ions.[173,174]

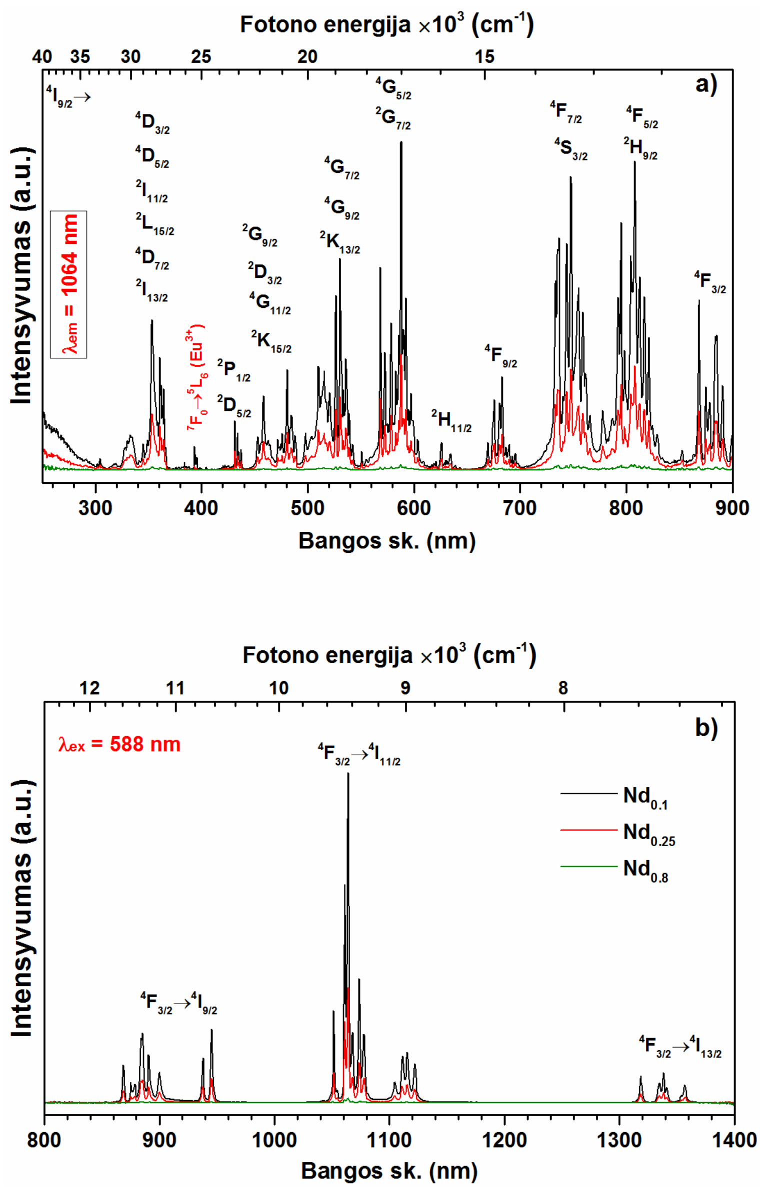

Fig. 39. Excitation (a) and emission (b) spectra of $Y_{3-x}Nd_xAl_5O_{12}$:0.5%Eu samples.

Asymmetry ratio defined as ($^5D_0 \rightarrow {}^7F_2$)/($^5D_0 \rightarrow {}^7F_1$) provides a measure of the degree of distortion of the inversion symmetry of the local Eu^{3+} ions in the lattice. If the asymmetry ratio value is low, the Eu^{3+} tends to localize at a high symmetry site or centrosymmetric site. In contrast when the ratio symmetry value is high, the Eu^{3+} tends to localize at a low symmetry site or non-centrosymmetric site[174,186,187]. The most intensive Eu^{3+} emission is with 1% europium and it decreases with decreasing the doping level of europium. The intensity of luminescence increases much faster when samples are doped with more than 0.5% europium (see Fig. 40). Fig. 41 represents luminescence of $Y_{3-x}Nd_xAl_5O_{12}$:0.5%Eu samples having a constant amount of Eu (0.5%) and different amount of neodymium. Emission spectra were recorded with excitation at 394 nm and excitation spectra with emission at 591 nm. Neodymium ion is strongly affected by luminescent ion distribution and as a result with increasing amount of Nd^{3+} the intensity of luminescence decreased, despite the same level of europium.

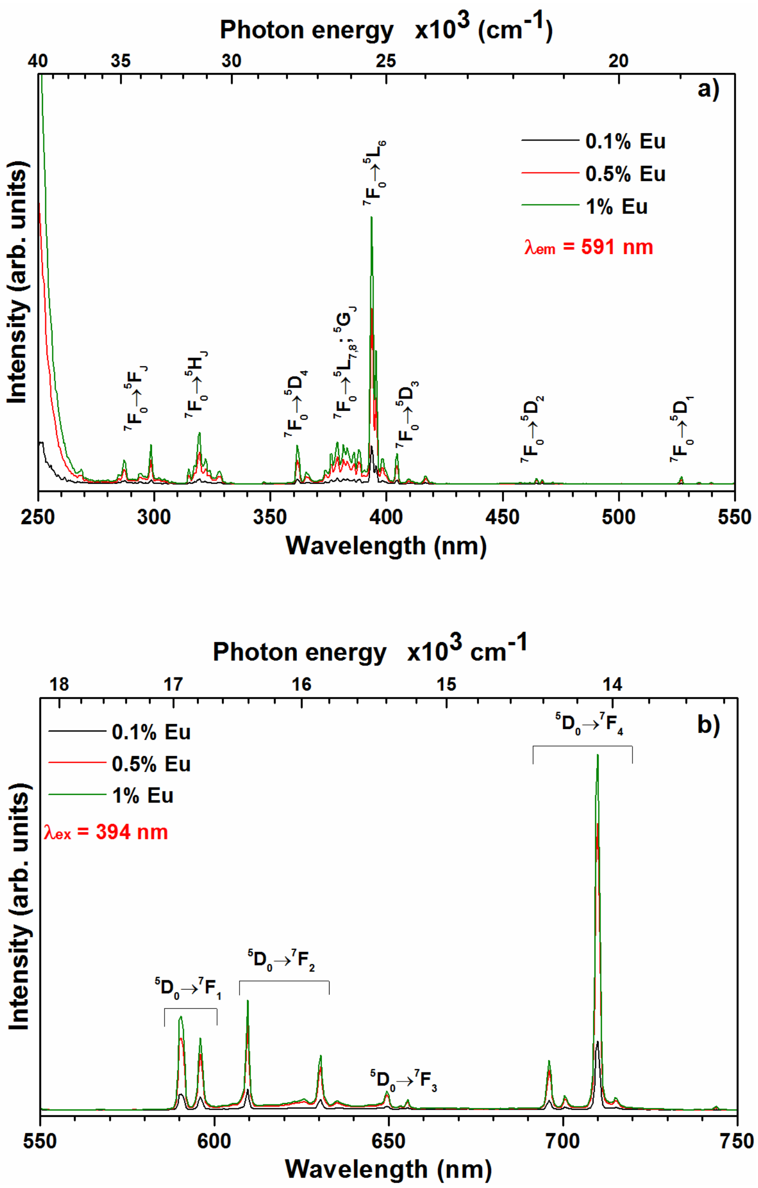

Fig. 40. Excitation (a) and emission (b) spectra of $Y_{2.9}Nd_{0.1}Al_5O_{12}$:Eu samples.

It is well known that energy transfer (ET) process between luminescent ions can only occur if the energy differences between the ground and excited states of sensitizer and activator are equal (resonance condition) and if a suitable interaction between both systems exists. According to Dieke's diagram this resonance condition is satisfied for the $^5D_0 \rightarrow {}^7F_1$ (Eu^{3+}) and $^4I_{9/2} \rightarrow ({}^2G_{7/2} + {}^4G_{5/2})$ (Nd^{3+}) transitions (Fig. 42).

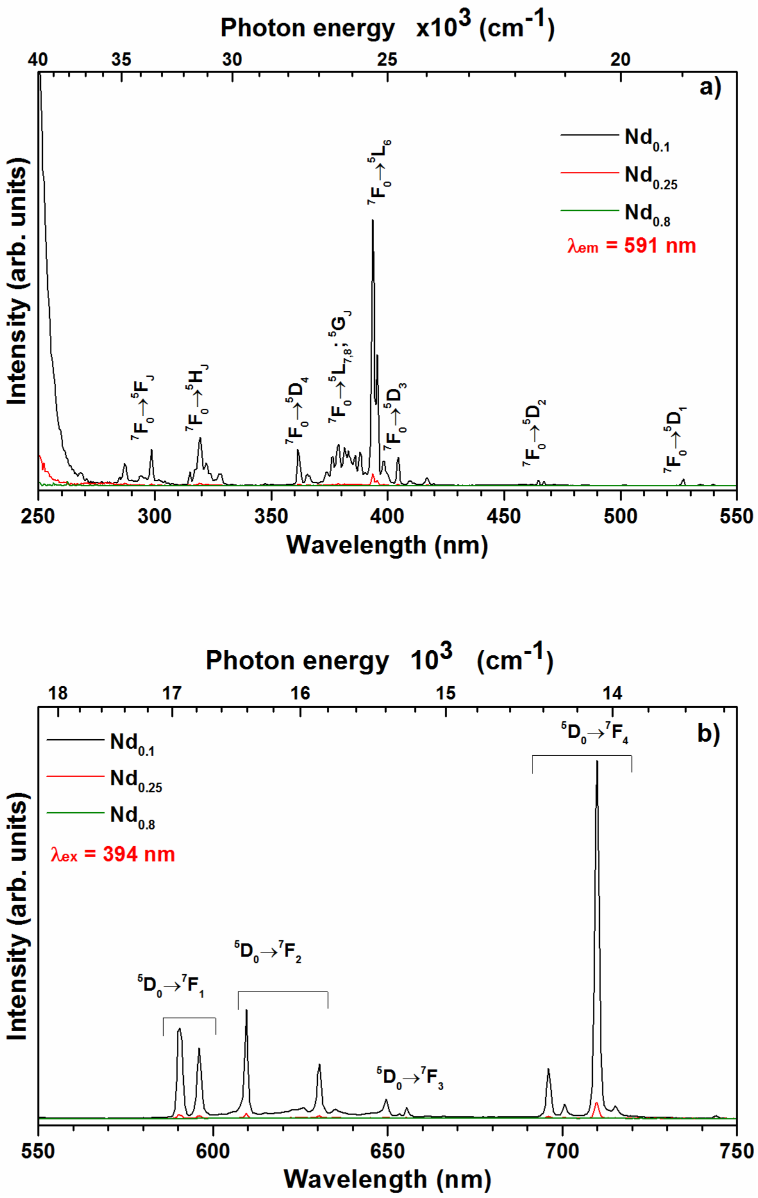

Fig. 41. Excitation (a) and emission (b) spectra of the $Y_{3-x}Nd_xAl_5O_{12}$:0.5%Eu samples.

PL spectrum (Fig. 38 and 39) consists of 3 main photoluminescence bands centered at 875, 1052 and 1324 nm, which are assigned to the $^4F_{3/2} \rightarrow {}^4I_{9/2}$, $^4I_{11/2}$ and $^4I_{13/2}$ transitions of Nd^{3+}, respectively. Although no distinct difference in peak position was observed. The enhancement of fluorescence intensity in ceramic is due to the incorporation of Nd^{3+} into crystalline phase with lower phonon energy. Moreover, it was observed that the intensity of Nd^{3+} emission decreased with increasing of Eu^{3+} concentration (Fig. 39). Eu^{3+} fluorescence decreased with the increasing of Nd^{3+} content due to the energy transfer between these ions.

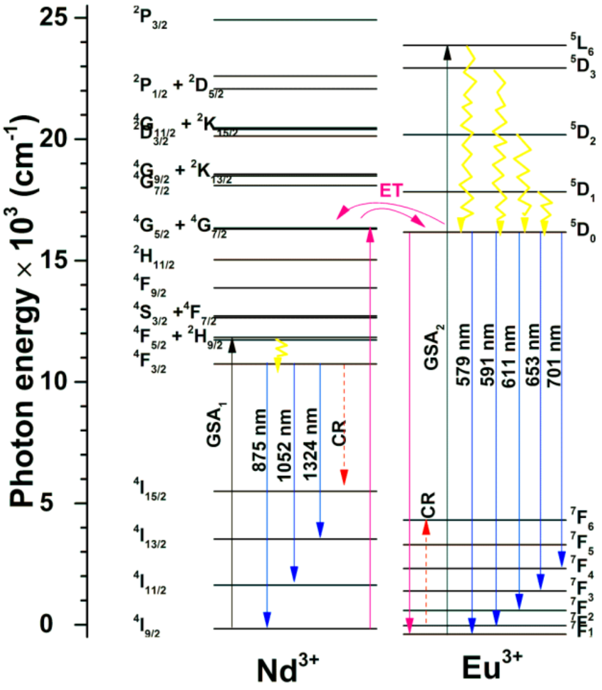

Fig. 42. Energy level diagram of Nd^{3+}and Eu^{3+} ions showing the ground state absorption (GSA), the cross-relaxation process (CR) and the energy transfer (ET) process

The decrease is higher for the peak at 591 nm compared to the one at 611 nm, due to the overlapping with the strong Nd^{3+} absorption band centered at this wavelength. Energy transfer between ions could occur between the levels Eu^{3+}: $^5D_0$ and Nd^{3+}: $^2G_{7/2}$, $^4G_{5/2}$ or between Eu^{3+}: $^5D_0$ and Nd^{3+}: $^4F_{5/2}$, $^2H_{9/2}$ (see Fig. 39). The variation of luminescence intensity of the transition centred at 1061 nm ($^4F_{3/2} \rightarrow {}^4I_{11/2}$) with Eu^{3+} ion concentration depicted in Fig. 40. The decrease of this band with the Eu^{3+} ion concentration may be attributed to the cross relaxation process ($^4F_{3/2}$ + $^7F_0$) → ($^4I_{15/2}$+ $^7F_6$) from Nd^{3+} to Eu^{3+} ions (Fig. 42) as already observed. [98,188,189,190]

3.5. Sol-Gel Synthesis and Characterization of Eu^{3+}-doped $Y_{3-x}Sm_xAl_3O_{12}$ Garnet

In this part, the YAG samples doped with different amount of Sm^{3+} and YAG:Sm garnets with various doping levels of europium were synthesized by sol-gel method and investigated.

3.5.1. XRD, FTIR, SEM, NMR and RAMAN analyses

The XRD patterns of $Y_{2.9}Sm_{0.1}Al_5O_{12}$, $Y_{3-x}Sm_xAl_5O_{12}$:0.5%Eu, $Y_{2.9}Sm_{0.1}Al_5O_{12}$:Eu samples are shown in Fig. 43.

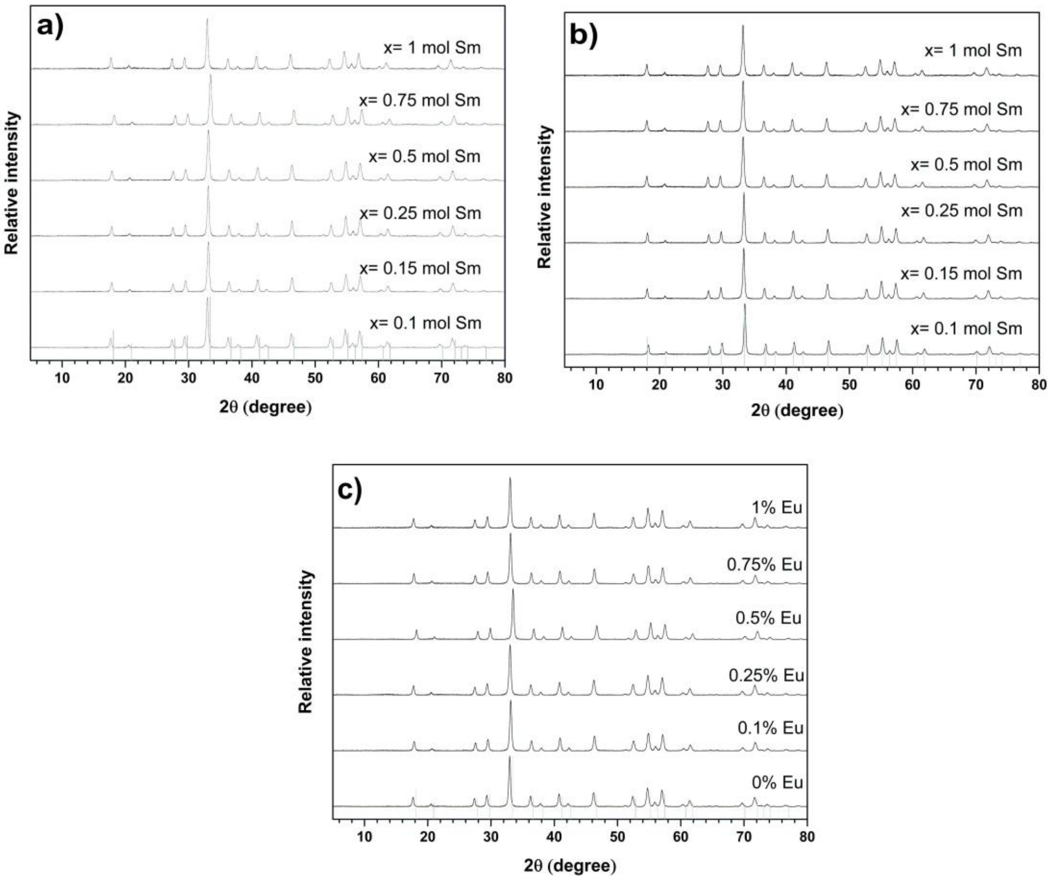

Fig. 43. XRD patterns of the $Y_{2.9}Sm_{0.1}Al_5O_{12}$ (a), $Y_{3-x}Sm_xAl_5O_{12}$:0.5%Eu (b), $Y_{2.9}Sm_{0.1}Al_5O_{12}$:Eu (c) samples annealed at 1000 °C for 10 h. Vertical lines represent the standard XRD pattern of YAG.

The XRD results revealed that samarium and europium co-doped garnet samples consist of a single YAG crystalline phase in the whole investigated substitutional range. Comparing with reference data, our synthesized garnets showed almost the same lattice parameters as standard $Y_3Al_5O_{12}$ [PDF 88-

2048]. The Sm^{3+} and Eu^{3+} ions incorporated in the lattice both substitute the Y^{3+} ions. The small increase in the lattice parameter for the Eu^{3+} doped samples compared to the undoped one has been attributed to the larger ionic radius of Eu^{3+} (1.095 Å)[180] compared to Y^{3+} ions (1.053 Å). Moreover, a small decrease in the lattice parameter should appear in garnet lattice doped with Sm^{3+} ion (ionic radius 0.958 Å)[180,191]. Therefore, the lattice parameter of garnets that are co-doped with both ions (Sm^{3+} and Eu^{3+}) perhaps should be similar for the undoped sample since the average of ionic radius is compensated by larger and smaller ionic radii of these lanthanides.

The FTIR spectra of the $Y_{2.9}Sm_{0.1}Al_5O_{12}$, $Y_{3-x}Sm_xAl_5O_{12}$:0.5%Eu and $Y_{2.9}Sm_{0.1}Al_5O_{12}$:Eu samples are shown in Fig. 44.

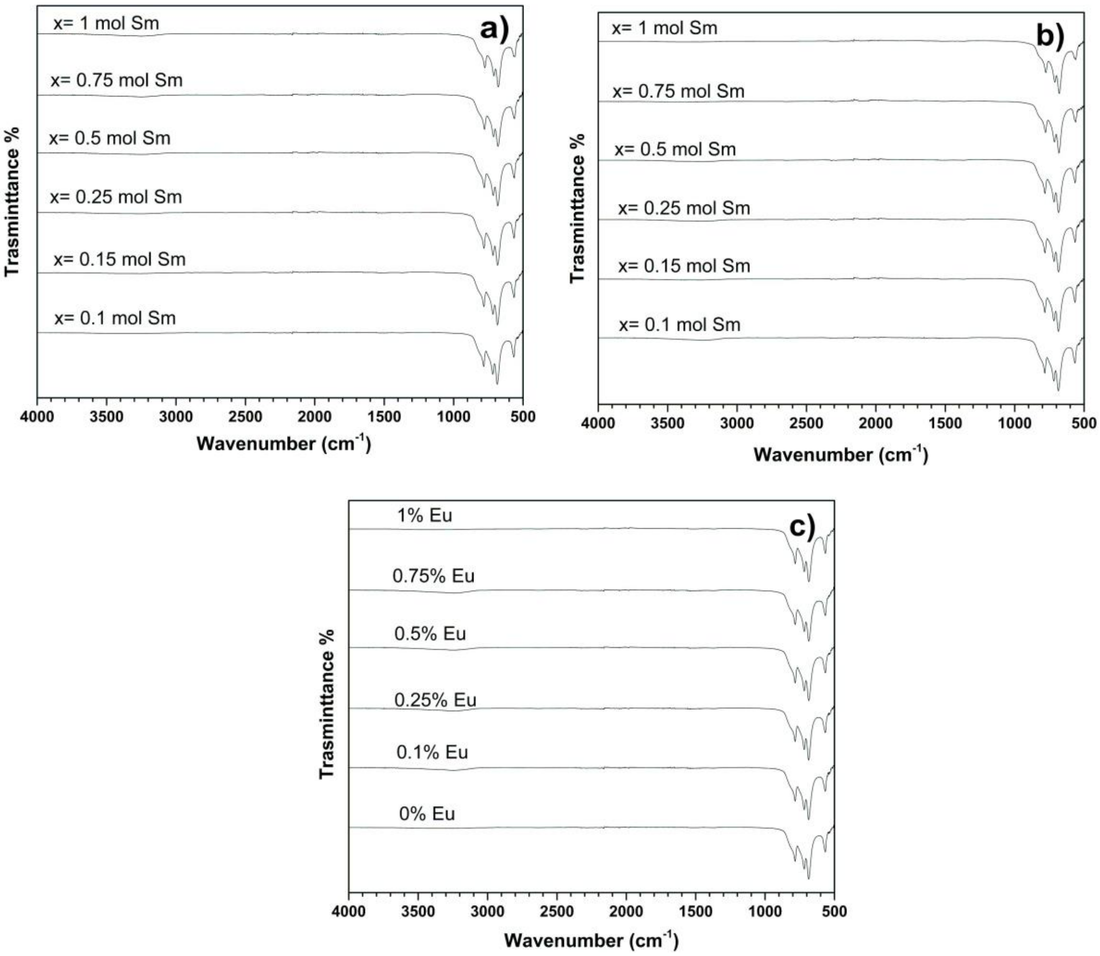

Fig. 44. FTIR spectra of the $Y_{2.9}Sm_{0.1}Al_5O_{12}$ (a), $Y_{3-x}Sm_xAl_5O_{12}$:0.5%Eu (b) and $Y_{2.9}Sm_{0.1}Al_5O_{12}$:Eu (c) samples.

As seen, all FTIR spectra are almost identical to previous ones supporting the results of XRD measurement.

The SEM micrographs of the $Y_{3-x}Sm_xAl_5O_{12}$, $Y_{2.9}Sm_{0.1}Al_5O_{12}$:Eu and $Y_{3-x}Sm_xAl_5O_{12}$:1%Eu powders are shown in Fig. 45-47, respectively. Fig. 45 shows the formation of very homogeneous mixed-metal garnets with nano-sized spherically shaped particles. The microstructures of $Y_{2.9}Sm_{0.1}Al_5O_{12}$:Eu and $Y_{3-x}Sm_xAl_5O_{12}$:1%Eu samples again are very similar.

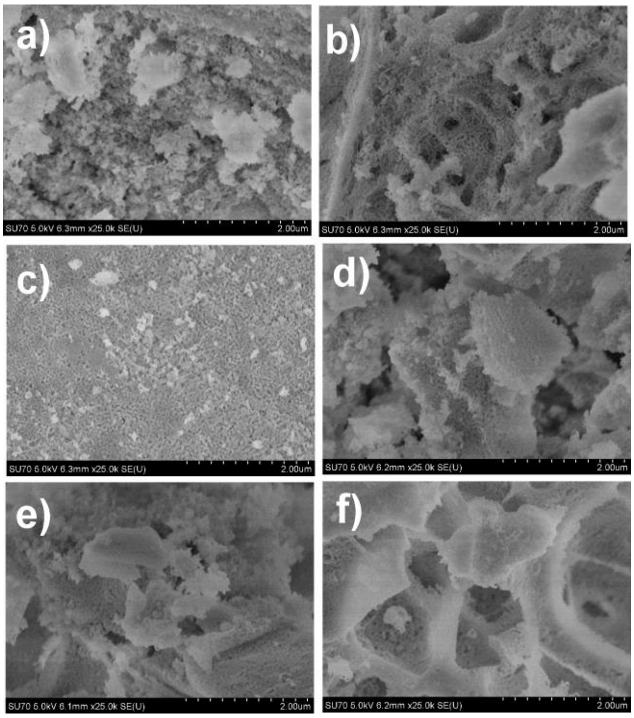

Fig. 45. SEM micrographs of $Y_{3-x}Sm_xAl_5O_{12}$ garnets (Sm: 0.1% (a); 0.15% (b); 0.25% (c); 0.5% (d); 0.75% (e); 1% (f)).

The resonance frequency of ^{27}Al nuclei that are close to the Sm^{3+} substituent ions is shifted to higher values compared to the resonance frequency of ^{27}Al nuclei that have only Y^{3+} ions nearby. This is a result of a through-bond hyperfine interaction and through-space anisotropic dipolar interaction between the unpaired Sm^{3+} 4*f* electronic spins and the ^{27}Al nuclear spins[184]. At low concentrations of Sm^{3+} in the samples, two major ^{27}Al signals at 68 ppm and 0 ppm can be observed (Fig. 48-50). The signals belong to four- and six-coordinated aluminium atoms surrounded by yttrium, respectively.

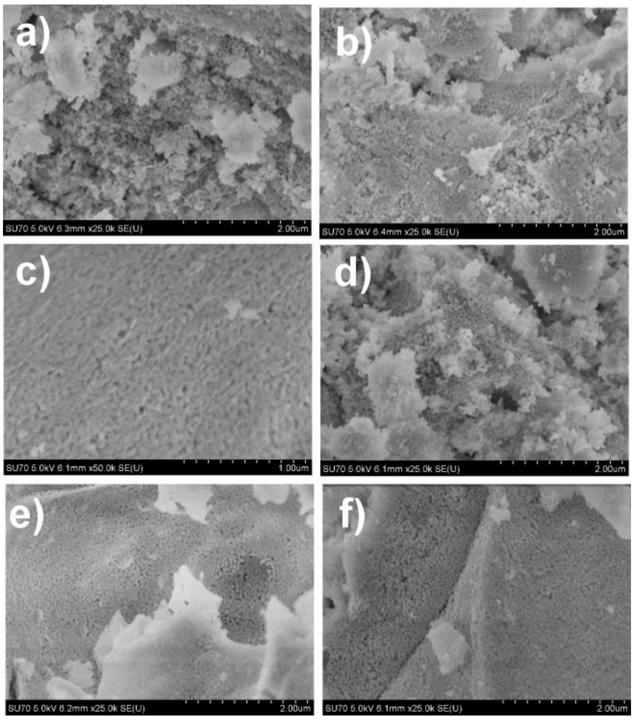

Fig. 46. SEM micrographs of $Y_{2.9}Sm_{0.1}Al_5O_{12}$:Eu garnets (Eu: 0% (a); 0.1% (b); 0.25% (c); 0.5% (d); 0.75% (e); 1% (f)).

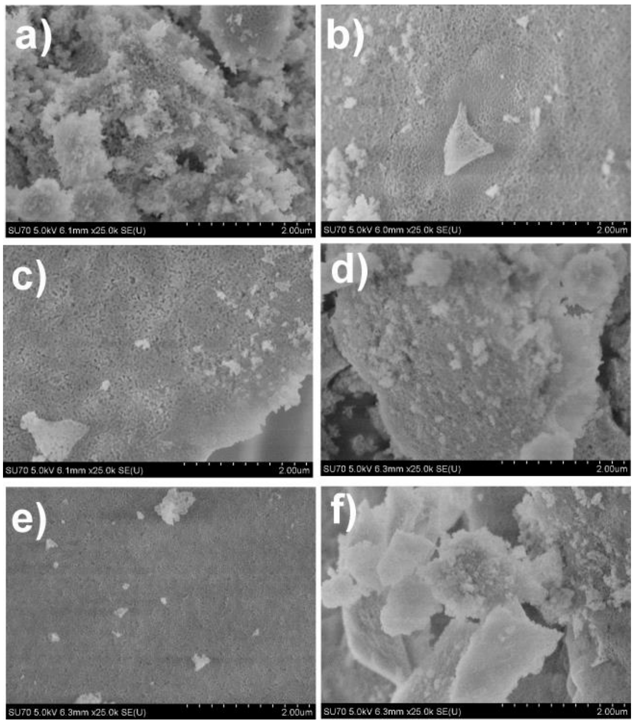

Fig. 47. SEM micrographs of $Y_{3-x}Sm_xAl_5O_{12}$:0.5%Eu garnets (Sm: 0.1% (a); 0.15% (b); 0.25% (c); 0.5% (d); 0.75% (e); 1% (f)).

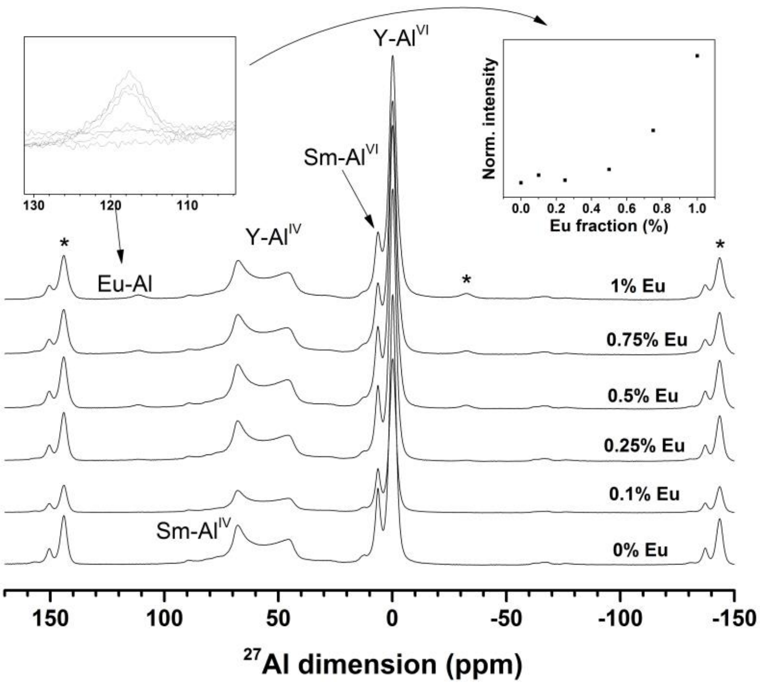

Fig. 48. ^{27}Al MAS NMR spectra of the $Y_{2.9}Sm_{0.1}Al_5O_{12}$:Eu samples.

In addition to the two strong signals (Fig. 48-50), peaks at 88 ppm and 6 ppm can be observed in the ^{27}Al MAS NMR spectra. The latter two peaks can be assigned respectively to Al^{IV} and Al^{VI} atoms with one samarium cation in their first cation coordination shells (Al^{IV}(1Sm) and Al^{VI}(1Sm)). These peaks already confirm the proximity of Al and Sm within the YAG:Sm,Eu materials. At high samarium concentrations peaks at 88 ppm and 6 ppm increase and become broader. Asterisks denote spinning sidebands.

In the group of samples with permanent amount of europium ion 0.5% and different amount of samarium (Fig. 49) we could observe the same tendency as in those without europium (Fig. 50). Peaks of Al^{IV} and Al^{VI} with samarium and yttrium in their vicinities increases with increasing doping element. Also at high Sm^{3+} concentration (e.g. x=0.8), additional peaks appear at 19 ppm and 25 ppm. The paramagnetic shifts are additive with the number of proximal Sm^{3+} ions, and therefore these peaks can be attributed to the Al^{VI} nuclei that have two and three Sm^{3+} ions in the first cation coordination shell, respectively; their intensities increased with increasing amount of samarium.

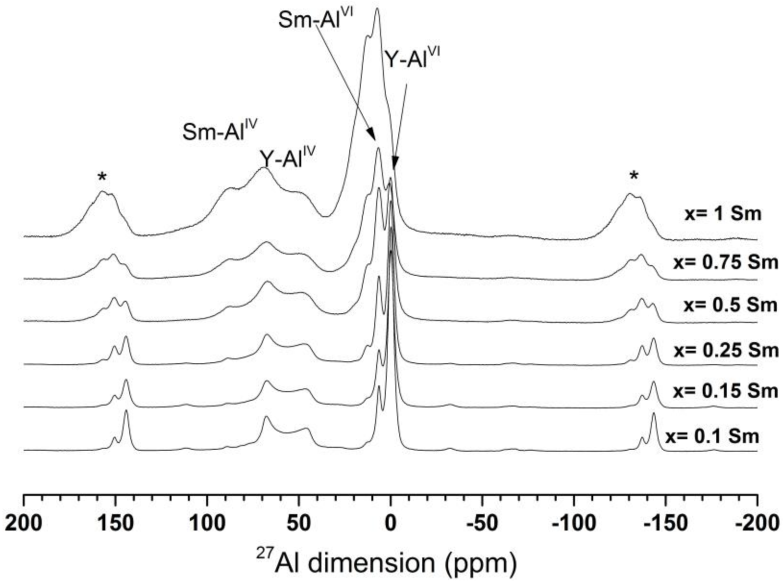

Fig. 49. ^{27}Al MAS NMR spectra of the $Y_{3-x}Sm_xAl_5O_{12}$:0.5%Eu samples.

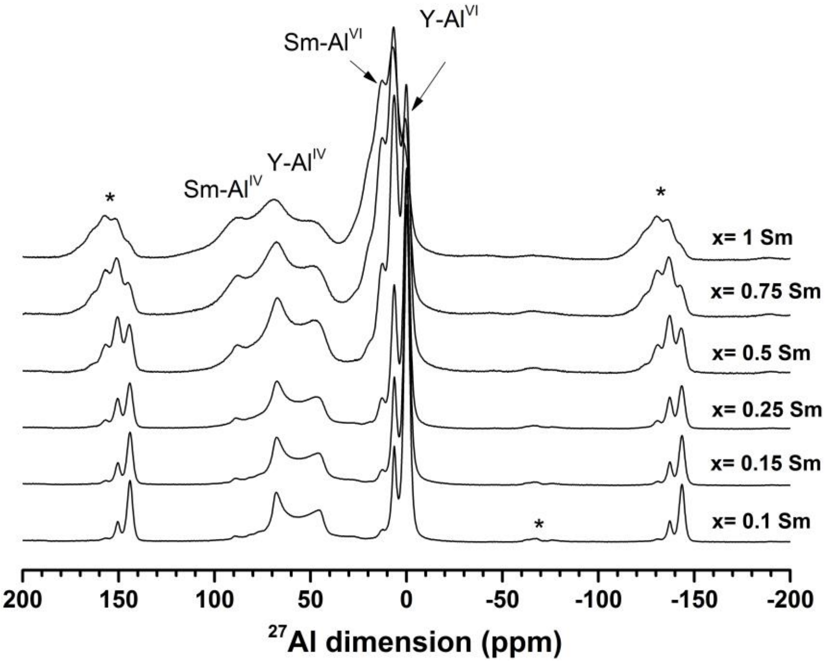

Fig. 50. ^{27}Al MAS NMR spectra of the $Y_{3-x}Sm_xAl_5O_{12}$ samples.

Intensities of different aluminium signals as a function of Sm^{3+} concentration in the samples are represented in Fig. 51. Solid lines represent the calculated integral intensities after fitting the overlapping contour using multiple Voigt profile for the random spatial distribution of Sm^{3+} ions along the crystal lattice. The discrepancy between the Al^{VI} data points for the corresponding calculated lines are the consequence of overlapping Al^{VI}, Al^{IV}(Sm), Al^{IV}(2Sm) and Al^{IV}(3Sm) signals. A simple calculation of expected aluminium intensities based on probabilities for a normal distribution that the Sm^{3+} ions are randomly dispersed throughout the crystal lattice of YAG:Sm,Eu (Fig. 48-52).

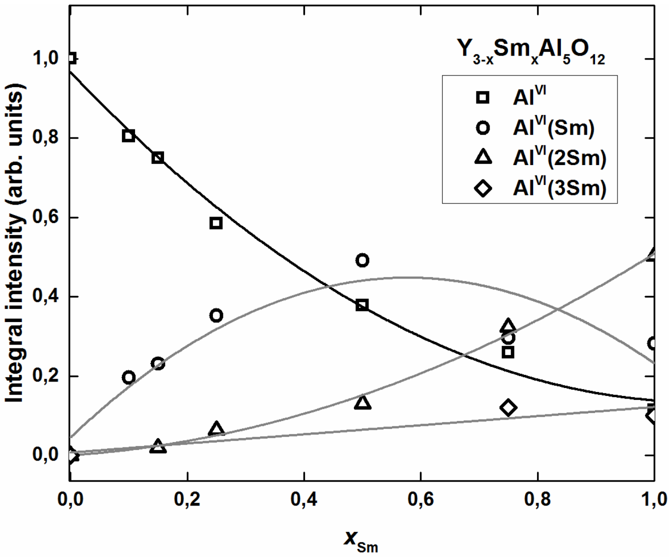

Fig. 51. Integral intensities of different aluminium sites as a function of concentration of Sm^{3+} in the samples.

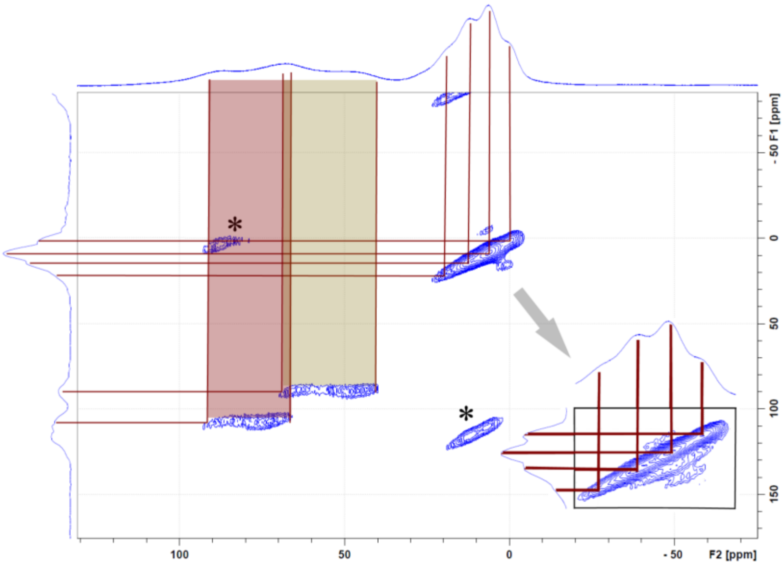

Fig. 52. 3Q MQMAS picture of $Y_2Sm_1Al_5O_{12}$ sample, an expansion of a spectral region from -10 ppm to 20 ppm indicated by an arrow.

^{27}Al MAS NMR also undoubtedly confirms the successful incorporation of europium ions into the crystalline lattice of YAG:Sm,Eu. As Eu^{3+} ion has six unpaired 4*f* electrons, large paramagnetic shift is expected for the closest ^{27}Al nuclei[192]. Indeed, the resonance frequency of Al^{VI} with one europium cation in the neighbourhood is shifted to substantially higher values, i.e. to 112 ppm. We analysed the ^{27}Al peak intensities of $Y_{2.9}Sm_{0.1}Al_5O_{12}$:Eu samples (Fig. 53), in which the content of europium varied. The linear relation between the Al(1Eu) line intensity and the Eu^{3+} indicates that, as for samarium, the spatial distribution of europium ions in these samples is also homogeneous.

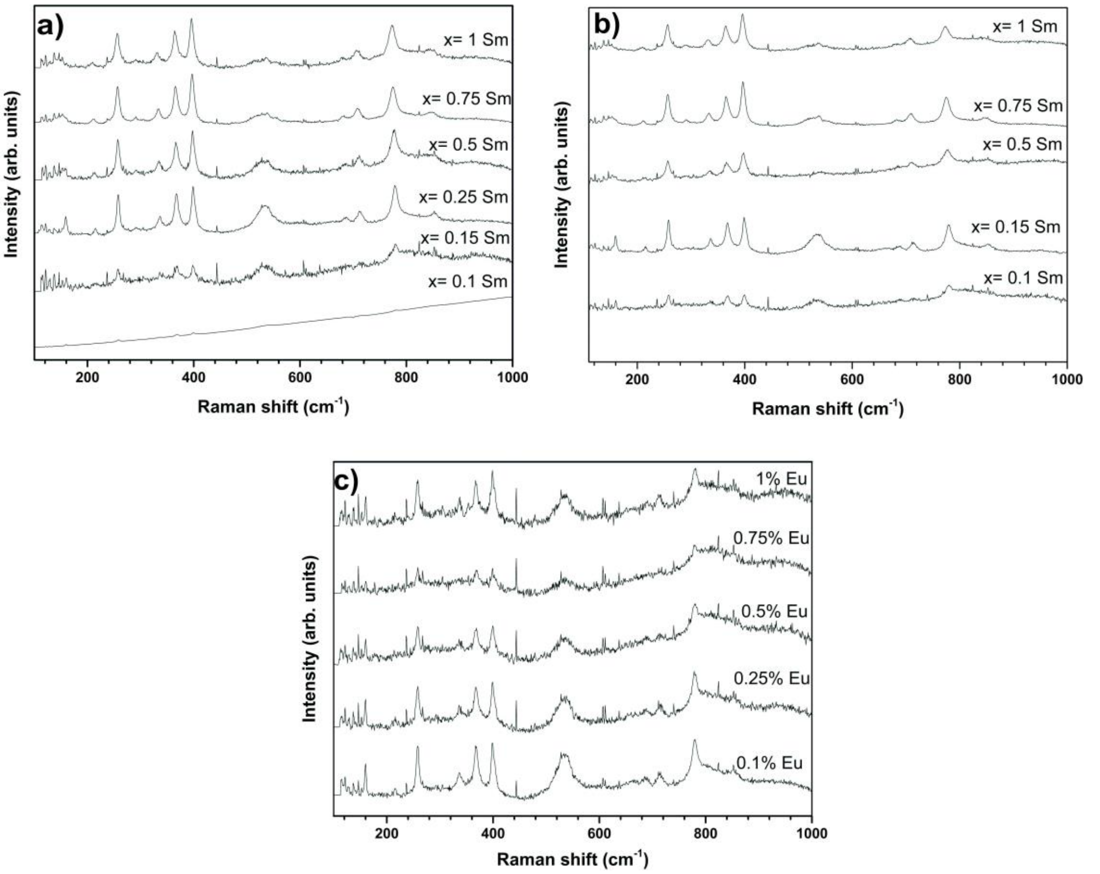

Fig. 53. Raman spectra of the $Y_{3-x}Sm_xAl_5O_{12}$ (a), $Y_{3-x}Sm_xAl_5O_{12}$:0.5%Eu (b) and $Y_{2.9}Sm_{0.1}Al_5O_{12}$:Eu (c) samples recorded using 488 nm excitation.

YAG crystallizes in the cubic structure Ia-3d (O^h_{10}) with eight formula units in the primitive cell. For the O^h_{10} structure of YAG, group theory predicts $3A_{1g} + 5A_{2g} + 8E_g + 14F_{1g} + 14F_{2g} + 5A_{1u} + 5A_{2u} + 10E_u + 17F_{1u} + 16F_{2u}$ Brillouin zone center optic modes. The A_{1g}, E_g and F_{2g} modes are Raman-active and F_{1u} modes are IR active[193,194]. Therefore, there should be 25 bands in Raman spectra and 17 in IR spectra for the Ia-3d structure. The Raman spectra of $Y_{3-x}Sm_xAl_5O_{12}$ samples are presented in Fig. 53 (a).

The spectrum of the YAG:Sm sample shows bands at 156, 215, 256, 289, 334, 367, 398, 443, 536, 681, 712, 778, 852 cm^{-1}. The bands at 536 and 443 cm^{-1} cannot be assigned to any Raman-active mode of YAG since single crystal data did not reveal any bands in the 440-530 cm^{-1} range. Therefore, the broad band at this area is not Raman but an emission band, probably arising from some Sm^{3+} ions present in the Y^{3+} sites. Other bands observed in Fig. 53 (a) correspond to the most intense Raman bands of bulk YAG, found at 156 (E_g), 215 (F_{2g}), 256 (F_{2g}), 334 (E_g), 367 (A_{1g}), 398 (E_g), 712 (F_{2g}), 778 (A_{1g}) and 852 cm^{-1} (F_{2g}). The bands indicated at 289 and 681 cm^{-1} arise from Sm^{3+} ions, which replaces Y^{3+} of the Y-O dodecahedron in Sm^{3+} doped YAG crystal, and new Raman peaks will be generated due to the symmetric bending vibration of the Sm-O bond. However, the intensity of Raman peaks is very weak due to the low concentration of Sm^{3+} in the garnets[195]. According to the data available from the literature, Raman bands in the range of 700-860 cm^{-1} correspond to the vibrations of Al-O in quasi-isolated AlO_4 tetrahedra. The A_{1g} mode at 367 cm^{-1} corresponds to the rotational vibration of the AlO_4 and AlO_6 units. The E_g bands at 398 and 334 cm^{-1} can also be assigned to vibrations of both AlO_4 and AlO_6 units whereas the bands below 300 cm^{-1} were assigned to lattice modes[20,193,196]. It is worth mentioning that Raman spectra do not show any clear bands that could be attributed to non-crystalline phase. There is a very strong fluorescence background occurring in the Raman spectra when the excitation wavelength is 488 nm, and it is attributed to the absorption of the optically active Sm^{3+} ions in this spectral range in YAG:Sm crystal. Generally, in the sample doped with 0.1 molar part of Sm^{3+} ions, the fluorescence intensity is larger than the Raman scattering intensity, which will decrease the intensity of observed Raman peaks[197]. This is the reason why in the spectrum of sample with 0.1 molar part of Sm^{3+} ions no peaks were observed. The similar tendency is observed for the sample doped with 0.15% of samarium.

As a result, according to the Raman spectra, whether the structure and the composition of the bonded interface are YAG or YAG:Sm could be determined.

Raman spectra of the $Y_{2.9}Sm_{0.1}Al_5O_{12}$:Eu and $Y_{3-x}Sm_xAl_5O_{12}$:0.5% Eu samples (Fig. 53 (b,c)) also show bands typical for YAG. Interestingly, apart from the bands typical for YAG phase, some other bands appear for these samples. The spectra of samples containing smallest amount of Eu^{3+} show also the presence of a very weak band near 676 cm^{-1}. Another clear Raman band appears at 825 cm^{-1} for the samples doped with europium. The absence of any band near 190 cm^{-1} and bands in the region of 550-660 cm^{-1} (just 607 cm^{-1}) indicates that samples do not contain any h-$YAlO_3$ or α-Al_2O_3 phases. Regarding $Y_4Al_2O_9$, most Raman bands are expected to appear close to Raman bands of YAG. However, the lack of any band near 580-590 cm^{-1} in the spectra suggests that the samples do not contain any $Y_4Al_2O_9$ impurity. The band near 378 cm^{-1} may indicate the presence of Y_2O_3 in the samples and the bands at 355 (just in sample doped with 1% of Eu (Fig. 53 (a)) and 676 cm^{-1} can be most likely attributed to γ-AlOOH[44,136,194,198]. Origin of the 825 cm^{-1} band is not clear but it appears just in the samples doped with Eu^{3+} ions. Raman bands become wider and Raman intensity increases, as evidenced by significant decrease of the signal-to noise ratio and it can be attributed to fluorescence of the samples doped with higher amount of europium.

3.5.2.Optical properties

Emission spectra were measured at room temperature under 405.5 nm excitation for samarium and under 393.5 nm excitation for europium. Excitation spectra were recorded monitoring emission at 617.5 nm and at 709.5 nm for samarium and europium, respectively. Excitation and emission spectra of $Y_3Al_5O_{12}$:Sm garnets are shown in Fig. 54. Excitation spectra consist of 12 sets of lines at around 346, 361, 375, 404, 417, 419, 463, 467, 479, 485 and 500 nm. These lines originate from intraconfigurational transitions of Sm^{3+} ions from ground state $^6H_{5/2}$ to the excited states, namely, ($^4D_{7/2}$), ($^4D_{3/2}$), ($^6P_{7/2}$), ($^6P_{3/2}$), ($^6P_{5/2}$ + $^4M_{19/2}$), ($^4I_{13/2}$ + $^4M_{15/2}$), ($^4I_{11/2}$), ($^4I_{9/2}$) and ($^4G_{7/2}$), respectively. The emission spectra comprises several peaks located at 559-576 nm; 592-617 nm; 651-666 nm and 711-732 nm, which arise due to the $^4G_{5/2} \rightarrow {^6H_{5/2}}$; $^4G_{5/2} \rightarrow {^6H_{7/2}}$; $^4G_{5/2} \rightarrow {^6H_{9/2}}$ and $^4G_{5/2} \rightarrow {^6H_{11/2}}$ transitions of Sm^{3+} [4,33,94,165,198]. As seen, the 0.1 mol Sm-doped sample shows the most intensive luminescence. It is clearly seen that intensity of all peaks increases proportionally with decreasing the doping level of samarium.

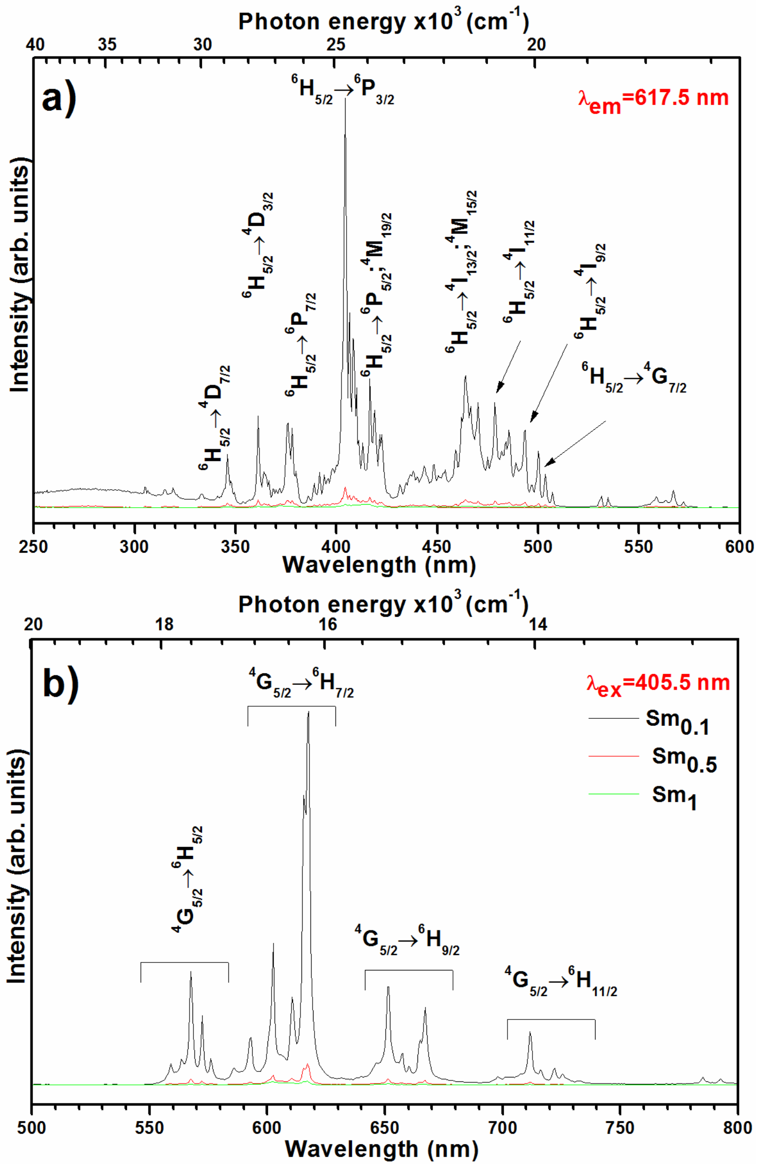

Fig. 54. Excitation (a) and emission (b) spectra of $Y_{3-x}Sm_xAl_5O_{12}$ samples.

The similar results are also observed for the $Y_{3-x}Sm_xAl_5O_{12}$:0.5%Eu samples (see Fig. 55). However, a new set of lines in excitation spectra at around 393 and 416 nm was observed. These lines are attributed to the $^7F_0 \rightarrow {}^5G_2$ and $^7F_0 \rightarrow {}^5D_2$ transition of Eu^{3+} ions. These transitions were not observed in the samples without europium. In emission spectra new lines appear at 588 and 596 nm attributable to $^5D_0 \rightarrow {}^7F_1$, also at 629 nm attributable to $^5D_0 \rightarrow {}^7F_2$. The line centred at 709 nm represents one of the strongest Eu^{3+} emission arising due to $^5D_0 \rightarrow {}^7F_4$ transition. This line is also attributed to Sm^{3+} transition at $^4G_{5/2} \rightarrow {}^6H_{9/2}$.

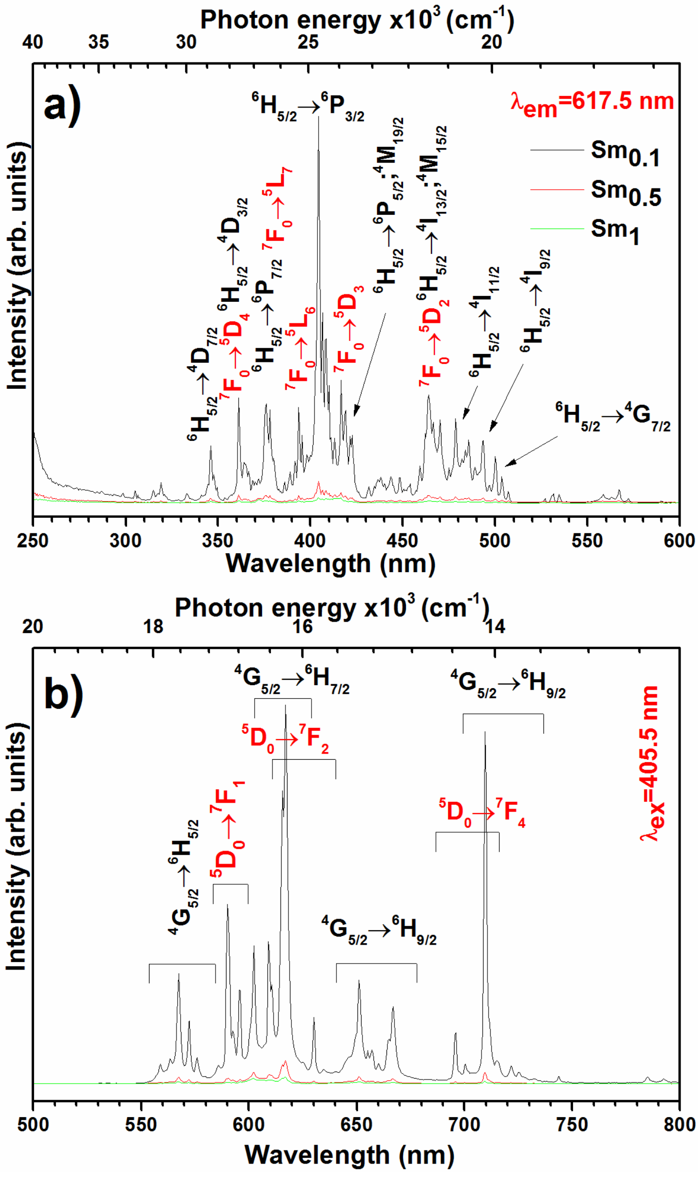

Fig. 55. Excitation (a) and emission (b) spectra of $Y_{3-x}Sm_xAl_5O_{12}$:0.5%Eu samples.

Upon excitation at 405.5 nm, the Sm^{3+} is promoted from the $^6H_{5/2}$ ground state to the $^6P_{3/2}$ excited state, and then it relaxes non-radiatively to the $^4G_{5/2}$ emitting state, which gives rise to the Sm^{3+} emission (Fig. 55-57).

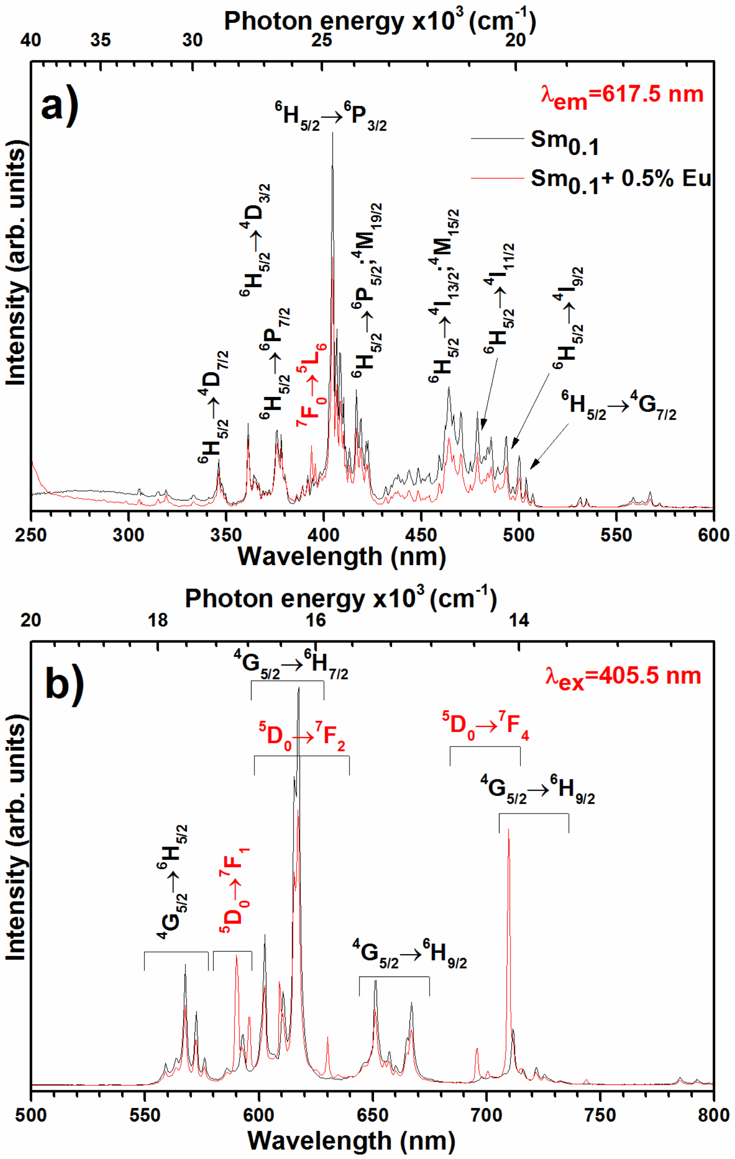

Fig. 56. Excitation (a) and emission (b) spectra of $Y_{2.9}Sm_{0.1}Al_5O_{12}$ and $Y_{2.9}Sm_{0.1}Al_5O_{12}$:0.5%Eu samples.

Due to the small energy mismatch between the samarium $^4G_{5/2}$ and europium $^5D_0$ states (404 cm^{-1}), the europium $^5D_0$ state is populated by an energy transfer process from the samarium $^4G_{5/2}$ state, which is responsible of the Eu^{3+} emission observed in the YAG:Sm;Eu upon Sm^{3+} excitation at 404.5 nm (Fig. 56 and 57). The small energy mismatch is compensated by the release of phonons to the lattice[36,109,110,111]. Fig. 58 shows excitation and emission spectra of $Y_{2.9}Sm_{0.1}Al_5O_{12}$:Eu. The obtained phosphor can be effectively excited with 394 nm near-UV radiation. Excitation was recorded with emission at 591 nm.

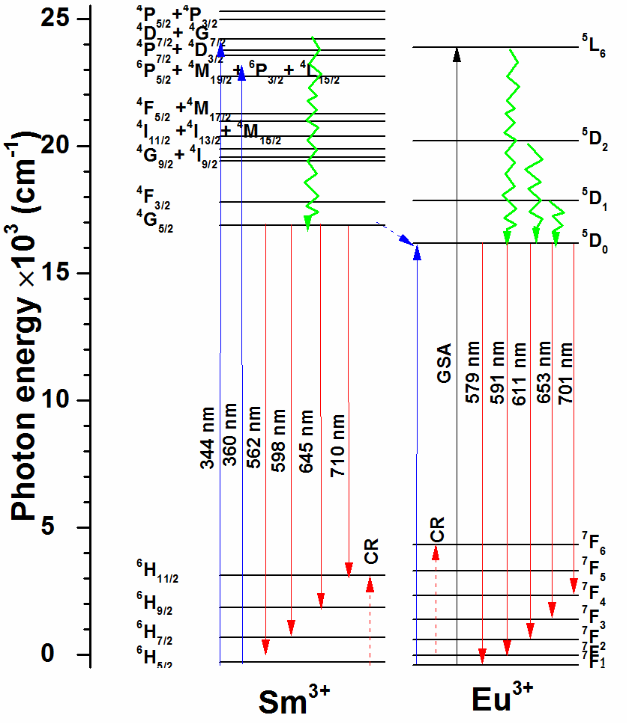

Fig. 57. Energy level diagram of Sm^{3+} and Eu^{3+} ions showing the ground state absorption (GSA), the cross-relaxation process (CR).

The emission peaks found between 550 and 800 nm in Fig. 58 are in a good agreement with the reported values of Eu^{3+} emission transitions[165,169,170]. The spectra show the characteristic emission of Eu^{3+} arising due to $^5D_0 \rightarrow {}^7F_1$ (591 nm), $^5D_0 \rightarrow {}^7F_2$ (611 nm) and $^5D_0 \rightarrow {}^7F_4$ (708 nm) transitions[50]. As expected for the Eu^{3+} ions a typical strong red emission was present with the line at 708 nm originated from the $^5D_0 \rightarrow {}^7F_4$ transition. The most intensive Eu^{3+} emission is obtained for the sample with 1% europium and it decreases with decreasing the doping level of europium. The intensity of luminescence increases much faster when samples are doped with more than 0.5% europium.

Fig. 59 represents luminescence of $Y_{3-x}Sm_xAl_5O_{12}$:0.5%Eu samples having a constant amount of Eu (0.5%) and different amount of samarium. Emission spectra were recorded with excitation at 394 nm and excitation spectra with emission at 591 nm. Samarium ion is strongly affected by luminescent ion distribution and as a result with increasing amount of Sm^{3+} the intensity of luminescence decreased, despite the same level of europium.

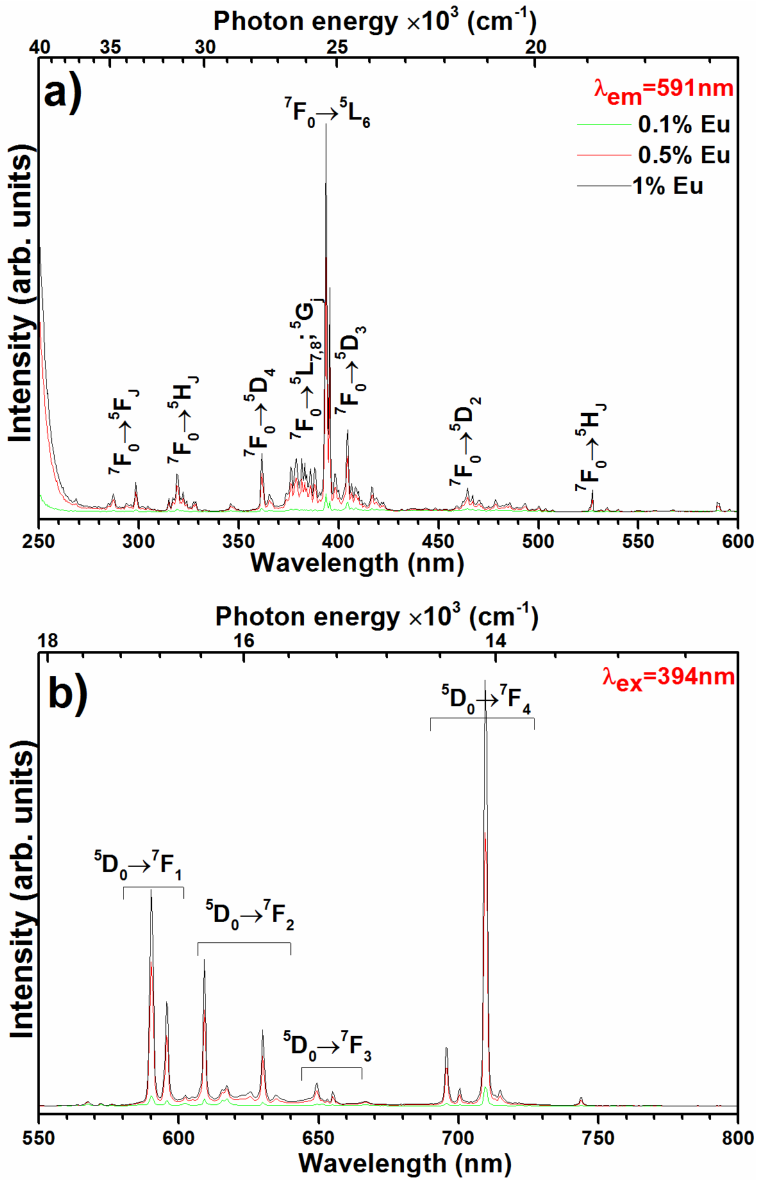

Fig. 58. Excitation (a) and emission (b) spectra of $Y_{2.9}Sm_{0.1}Al_5O_{12}$:Eu samples.

PL spectra (Fig. 58 and 59) consist of 3 main photoluminescence bands centred at 590 and 596 nm assigned to the $^5D_0 \rightarrow {}^7F_1$; 609 and 631 nm assigned to $^5D_0 \rightarrow {}^7F_2$ transition; ~650 nm - $^5D_0 \rightarrow {}^7F_3$ and 694 nm, 708 nm correspond to $^5D_0 \rightarrow {}^7F_4$ transition of Eu^{3+} ion.

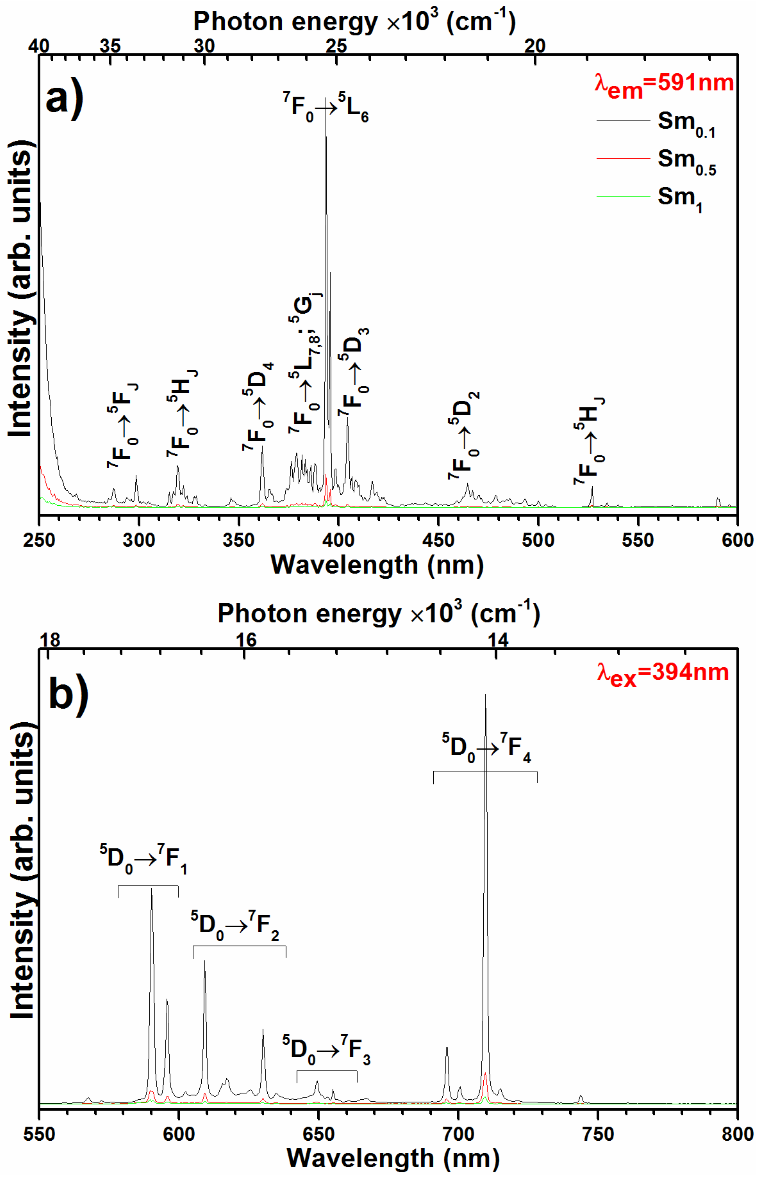

Fig. 59. Excitation (a) and emission (b) spectra of the $Y_{3-x}Sm_xAl_5O_{12}$:0.5%Eu samples.

CONCLUSIONS

1. The aqueous sol-gel process was developed to prepare monophasic $Tb_3Al_5O_{12}$:Eu, $Dy_3Al_5O_{12}$:Eu, $Ho_3Al_5O_{12}$:Eu, $Er_3Al_5O_{12}$:Eu, $Tm_3Al_5O_{12}$:Eu, $Yb_3Al_5O_{12}$:Eu, $Lu_3Al_5O_{12}$:Eu, $Y_3Al_5O_{12}$:Nd,Eu and $Y_3Al_5O_{12}$:Sm,Eu garnet structure materials at 1000 °C.
2. The individual particles of $Ln_3Al_5O_{12}$:Eu samples obtained by sol-gel method were submicro-sized plate-like crystals and they partially fused to form hard agglomerates, indicating good connectivity between the grains. It was also observed that agglomeration slightly increased with increasing the doping level of Eu^{3+}.
3. Monophasic $Ho_3Al_5O_{12}$:Eu was successfully synthesized for the first time by low temperature solvothermal method at 220 °C. SEM micrographs of $Ho_3Al_5O_{12}:Eu^{3+}$ synthesized by sovothermal method showed that crystallinity of garnets increased significantly by additional annealing of the specimens at 1000 °C and 1200 °C. The particle size of these samples monotonically increased from 100 nm (as-synthesized) to about 600 nm (annealed at 1200 ^oC).
4. The $Ho_3Al_5O_{12}$:0.5%Eu sample showed the most intensive europium emission at 591 nm in the series of $Ho_3Al_5O_{12}:Eu^{3+}$ garnets. The spectra of $Tb_3Al_5O_{12}$:Eu, $Dy_3Al_5O_{12}$:Eu and $Lu_3Al_5O_{12}$:Eu garnets showed the characteristic emission of Eu^{3+} arising due to $^5D_0 \rightarrow {}^7F_1$ (591-594 nm), $^5D_0 \rightarrow {}^7F_2$ (609-611 nm) and $^5D_0 \rightarrow {}^7F_4$ (708-709 nm) transitions. For the $Er_3Al_5O_{12}$, $Yb_3Al_5O_{12}$:Eu and $Tm_3Al_5O_{12}$ garnets doped with Eu^{3+}, however, no emission peaks in the luminescence spectra were observed.
5. Neodymium, samarium and europium substitution effects in $Y_{3-x}Ln_xAl_5O_{12}:Eu^{3+}$ (Ln – Nd^{3+} and Sm^{3+}) garnets synthesized by sol-gel method were investigated. The XRD results revealed that neodymium and samarium doped garnets were single phase materials in whole investigated substitutional range.
6. The $Y_{3-x}Ln_xAl_5O_{12}$, $Y_{2.9}Ln_{0.1}Al_5O_{12}:Eu^{3+}$ and $Y_{3-x}Ln_xAl_5O_{12}:Eu^{3+}$ (Ln – Nd^{3+} and Sm^{3+}) solids were composed of nano-sized spherical agglomerated

particles. Particle size and shape were not influenced by nature of lanthanides and their concentration.

7. ^{27}Al NMR spectroscopy showed for the first time the structural features of substituted garnets comparing the dependence of peaks intensity on the concentration of dopant in YAG:Nd,Eu and YAG:Sm,Eu. The results obtained revealed that the Nd^{3+} and Sm^{3+} ions are randomly dispersed throughout the crystal lattice of garnets and confirmed the successful incorporation of europium ions into the crystalline lattice of YAG:Ln,Eu.

8. Emision spectra for $Y_{3-x}Nd_xAl_5O_{12}:Eu^{3+}$ were obtained monitoring exitation at 588 nm for neodymium and at 394 nm for europium. The 0.1 mol Nd-doped sample showed the most intensive luminescence. For the Eu^{3+} ions a typical strong red emission was detected (611 nm originated from the $^5D_0 \rightarrow {}^7F_2$ transition). The most intensive Eu^{3+} emission was observed for the sample with 1% europium. Eu^{3+} fluorescence decreased with the increasing content of Nd^{3+} due to the energy transfer between these ions.

9. Emision spectra for $Y_{3-x}Sm_xAl_5O_{12}:Eu^{3+}$ were obtained monitoring exitation at 405.5 nm for samarium and at 393.5 nm for europium. The 0.1 mol Sm-doped sample showed the most intensive luminescence. For the Eu^{3+} ions a typical strong red emission was detected (708 nm originated from the $^5D_0 \rightarrow {}^7F_4$ transition). The most intensive Eu^{3+} emission was observed for the sample with 1% europium. Eu^{3+} fluorescence decreased also with the increasing content of Sm^{3+} due to the energy transfer between these ions.

LIST OF PUBLICATIONS

Articles in Journals and Proceedings

1. L. Pavasaryte, B. J. Lopez, A. Kareiva, Solvothermal synthesis of Eu^{3+}-doped holmium aluminum garnet. Mendeleev Communications, 25 (2015) 284-385.
2. L. Pavasaryte, B. J. Lopez, A. Kareiva, On the sol-gel preparation of selected lanthanide aluminium garnets doped with europium. International Conference on Photonics, Optics and Laser Technology, 2015 Berlin. Photoptics. Prtugal: Scitepress – Science and Technology Publications. ISBN: 978-989-758-093-2, Vol. 2 (2015) 165-171.
3. L. Pavasaryte, A. Katelnikovas, V. Klimavicius, V. Balevicius, A. Krajnc, G. Mali, J. Plavec, A. Kareiva, Eu^{3+} - doped $Y_{3-x}Nd_xAl_3O_{12}$ garnet: synthesis and structural investigation, Physical Chemistry Chemical Physics, 19 (2017) 3729-3737.

Published Contributions to Academic Conferences

1. L. Pavasaryte, B. J. Lopez, A. Kareiva, Sol-Gel Synthesis of Europium Doped $Tb_3Al_5O_{12}$, $Dy_3Al_5O_{12}$ and $Ho_3Al_5O_{12}$ Garnets. Chemistry and Chemical Technology 2015: international conference of Lithuanian Chemical Society, dedicated to Professor Vitas Daukšas on his 80th birth anniversary, Vilnius, Lithuania, 23 Januarry 2015, ISBN 978-609-459-461-8, p. 119-122.
2. L. Pavasaryte, B. J. Lopez, A. Kareiva, On the Sol-gel Preparation of Selected Lanthanide Aluminium Garnets Doped with Europium, Photooptics 2015: 3rd international conference on photonics, optics and laser technology, Berlin, Germany, 12-14 March 2015, ISBN: 978-989-758-093-2, (2015), p. 19-20.
3. L. Pavasaryte, V. Klimavicius, V. Balevicius, A. Krajnc, G. Mali, J. Plavec, A. Kareiva, Eu^{3+}- Doped $Y_{3-x}Nd_xAl_3O_{12}$:synthesis and structural investigation. Open Reading 2016: 59th Scientific Conference for Students of Physics and Natural Sciences, Vilnius, Lithuania. 15-18 March 2016, ISBN 2029-4425, p. 172.

4. L. Pavasaryte, A. Katelnikovas, A. Kareiva, Synthesis and Luminescence Propeerties Of Eu^{3+}-Doped $Y_{3-x}Nd_xAl_3O_{12}$, Chemistry and Chemical Technology: international conference of Lithuanian Society of Chemistry : Lithuanian Academy of Science, Vilnius, Lithuania, 28-29 April 2016, ISBN 978-609-95511-3-5, p. 201.

5. L. Pavasaryte, YAG:Nd,Eu Garnets: synthesis, luminescense and structural investigation, Inovatyvioji ir Tvarkioji Chemija, Puvočiai, Lietuva, 9-10 December 2016, ISBN 978-609-459-772-5, p. 15.

6. L. Pavasaryte, V. Klimavicius, V. Balevicius, A. Kareiva, Investigation Of Structural Properties Of Eu^{3+}-Doped $Y_{3-x}Sm_xAl_3O_{12}$ Garnets, Open Reading 2017: 60th International conference for students of physic and natural sciences, Vilnius, Lithuania. 14-17 March 2017, ISSN 2029-4425, p. 159.

7. L. Pavasarytė, V. Klimavicius, V. Balevicius, A. Katelnikovas, A. Kareiva, Investigation Of Structural ans Luminescence Properties Of Eu^{3+}-Doped $Y_{3-x}Sm_xAl_3O_{12}$ Garnets. International conference Functional materials and Nanotechnologies 2017: internatiponl conference, Tartu, Estonia. 24-27 april 2017, ISBN 978-9985-4-1030-1, p. 172.

8. L. Pavasaryte, A. Katelnikovas, A. Kareiva, Investigation of Luminescence Properties of Eu^{3+}-Doped $Y_{3-x}Sm_xAl_3O_{12}$ Garnet. The international conference dedicated to the 215th birth anniversary of Ignacy Domeyko, Vilnius, Lithuania 28-30 July 2017, ISBN 978-609-459-862-3, p. 85.

ACKNOWLEDGEMENTS

I would like to express my sincere gratitude to my supervisor Prof. Aivaras Kareiva for his guidance and support during my studies and especially during intership. Also for understanding and giving opportunity to combine studies with first steps in carreer.

Special thanks to Assoc. Prof. Artūras Katelnikovas from Faculty of Chemistry and Geosciences of Vilnius University for his guidance in luminescense measurements and data interpretation.

Moreover I would like to thank to Assoc. Prof. Ramūnas Skaudžius for introducing me with the basics of sol-gel chemistry.

I wish to thank all my colleagues from Faculty of Chemistry and Geosciences of Vilnius University, especially I would like to thank personnel of Department of Analytical and Environmental Chemistry and members of Sol-Gel Chemistry Group for their help and support.

Many thanks to my colleague Justina Gaidukevič for suporting and huge motivation.

Thanks to my colleague Danas Sakalauskas from Faculty of Chemistry and Geosciences of Vilnius University for performing SEM images and teaching how to use FTIR spectrometer and XRD difractometer.

I am thankful to Dr. Vytautas Klimavičius from Faculty of Physics of Vilnius University for performing NMR measurements and help in interpretation of obtained results.

I would also like to thank to my colleagues from Vilnius Gediminas Technical University, Department of Chemistry and Bioengineering for understanding.

Thank‘s to my co-supervisor Prof. Beatris Julian Lopez and colleagues during internship in Jaume I University, Spain.

Big gratitude to co-supervisor Dr. Janez Plavec and Dr. Gredor Mali from Slovenian NMR center. Also to colleagues, especially Andraž Krajnc.

I wish to thank to co-supervisors Prof. An Hardy and Prof. Marlies Van Bael from Hasselt University, Belgium, also to mentor Aleksandr Momot from the same institution.

Finally, I thank my family members for their love and support.

REFERENCES

1 Y. Zhou, Y. Zhou, J. Lin, J. Lin, M. Yu, M. Yu, S. Wang, S. Wang, H. Zhang and H. Zhang, Synthesis-dependent luminescence properties of $Y_3Al_5O_{12}$:Re^{3+} (Re=Ce, Sm, Tb) phosphors, *Mater. Lett.*, 2002, **56**, 628–636.

2 W. Q. Chen, D. S. Jo, Y. H. Song, T. Masaki and D. H. Yoon, Synthesis and photoluminescence properties of YAG:Ce^{3+} phosphor using a liquid-phase precursor method, *J. Lumin.*, 2014, **147**, 304–309.

3 Y. Pan, M. Wu and Q. Su, Tailored photoluminescence of YAG:Ce phosphor through various methods, *J. Phys. Chem. Solids*, 2004, **65**, 845–850.

4 M. S. Kurrey, A. Tiwari, M. S. K. Khokhar, R. S. Kher and S. J. Dhoble, Thermoluminescence investigations of sol–gel derived and γ-irradiated rare earth (Eu and Nd) doped YAG nanophosphors, *J. Lumin.*, 2015, **164**, 94–98.

5 A. Kareiva, Aqueous sol-gel synthesis methods for the preparation of garnet crystal structure compounds, *Medziagotyra*, 2011, **17**, 428–437.

6 Q. Liu, J. Liu, J. Li, M. Ivanov, A. Medvedev, Y. Zeng, G. Jin, X. Ba, W. Liu, B. Jiang, Y. Pan and J. Guo, Solid-state reactive sintering of YAG transparent ceramics for optical applications, *J. Alloys Compd.*, 2014, **616**, 81–88.

7 H. M. Lee, C. C. Cheng and C. Y. Huang, The synthesis and optical property of solid-state-prepared YAG:Ce phosphor by a spray-drying method, *Mater. Res. Bull.*, 2009, **44**, 1081–1085.

8 X. Li, H. Liu, J. Wang, H. Cui, F. Han and R. I. Boughton, Production of nanosized YAG powders with spherical morphology and nonaggregation via a solvothermal method, *J. Am. Ceram. Soc.*, 2004, **87**, 2288–2290.

9 Y. Iida, A. Towata, T. Tsugoshi and M. Furukawa, In situ Raman monitoring of low-temperature synthesis of YAG from different starting materials, *Vib. Spectrosc.*, 1999, **19**, 399–405.

10 M. J. G. Haohai Yu, K. Wu, B. Yao, H. Zhang, Z. Wang, J. Wang, Y. Zhang, Z. Wei, Z. Zhang, X. Zhang, Growth and characteristics of Yb-doped $Y_3Ga_5O_{12}$ laser crystal, *IEEE J. Quantum Electron.*, 2010, **46**, 1689–1695.

11 A. Golubović, S. Nikolic, R. Gajic, S. Duric and A. Valcic, The growth of Nd:YAG single crystals, *J. Serbian Chem. Soc.*, 2002, **67**, 291–300.

12 T. Vosegaard, D. Massiot, N. Gautier, H. J. Jakobsen, A. De, R. Scientifique and R. V January, ^{71}Ga chemical shielding and quadrupole coupling tensors of the garnet Y_3Ga5O_{12} from single-crystal ^{71}Ga NMR, *Inorg. Chem.*, 1997, **1669**, 2446–2450.

13 B. Ferrand, B. Chambaz and M. Couchaud, Liquid phase epitaxy: a versatile technique for the development of miniature optical components in single crystal dielectric media, *Opt. Mater. (Amst).*, 1999, **11**, 101–114.

14 R. Gaume, B. Viana, J. Derouet and D. Vivien, Spectroscopic properties of Yb-doped scandium based compounds Yb:$CaSc_2O_4$, Yb:$SrSc_2O_4$ and Yb:Sc_2SiO_5, *Opt. Mater. (Amst).*, 2003, **22**, 107–115.

15 I. Muliuoliene, S. Mathur, D. Jasaitis, H. Shen and V. Sivakov, Evidence of the formation of mixed-metal garnets via sol – gel synthesis, *Opt. Mater. (Amst).*, 2003, **22**, 241–250.

16 G. B. S. Chenais, F. Druon, F. Balembois, P. Georges, A. Brenier, Diode-pumped Yb:GGG laser: comparison with Yb:YAG, *Opt. Mater. (Amst).*, 2003, **22**, 99–106.

17 S. Mathur, H. Shen and A. Leleckaite, Low-temperature synthesis and characterization of yttrium – gallium garnet $Y_3Ga_5O_{12}$ (YGG), *Mater. Res. Bull. 40*, 2005, **40**, 439–446.

18 S. Sakirzanovas, L. Sun and A. Kareiva, Sol–gel synthesis of nanosized $Y_3Sc_{2.5}Ga_{2.5}O_{12}$ garnet, *Mendeleeev Commun.*, 2008, **18**, 251–252.

19 A. Katelnikovas and A. Kareiva, Low-temperature synthesis of lutetium gallium garnet (LGG) using sol – gel technique, *Mater. Lett.*, 2008, **62**, 1655–1658.

20 K. Papagelis, Vibrational properties of the rare earth aluminum garnets, *J. Appl. Phys*, 2003, **94**, 6491–6498.

21 J. Arvanitidis, K. Papagelis and S. Margadonna, Temperature-induced valence transition and associated lattice collapse in samarium fulleride, *Lett. to Nat.*, 2003, **425**, 599–602.

22 C. Milanese, V. Buscaglia, F. Maglia and U. Anselmi-Tamburini, Disorder and Nonstoichiometry in Synthetic Garnets $A_3B_5O_{12}$ (A = Y,Lu-La,B =Al, Fe, Ga). A Simulation Study, *Chem. Mater.*, 2004, **16**, 1232–1239.

23 X. Zhang, L. Zhou, Q. Pang, J. Shi and M. Gong, Tunable Luminescence and Ce3+ → Tb3+ → Eu3+ Energy Transfer of Broadband-Excited and Narrow Line Red Emitting Y2SiO5:Ce3+, Tb3+, Eu3+ Phosphor, J. Phys. Chem. C, 2014, **118**, 7591−7598.

24 K. N. Kumar, L. Vijayalakshmi and Y. C. Ratnakaram, Energy transfer based photoluminescence properties of (Sm^{3+} + Eu^{3+}): PEO + PVP polymer films for red luminescent display device applications, *Opt. Mater. (Amst).*, 2015, **45**, 148–155.

25 Y. Jia, W. Lu, N. Guo, W. Lu, Q. Zhao and H. You, Realization of color hue tuning via efficient Tb^{3+}-Mn^{2+} energy transfer in $Sr_3Tb(PO_4)_3$:Mn^{2+}, a potential near-UV excited phosphor for white LEDs, *Phys. Chem. Chem. Phys.*, 2013, **15**, 6057–6062.

26 L. Dobrzycki, E. Bulska, D. A. Pawlak, Z. Frukacz and K. Woz, Structure of YAG crystals doped/substituted with erbium and ytterbium, 2004, **43**, 7656–7664.

27 J. V Neel, Some Applications of the principles of genetics to the practice of medicine, *Med. Clin. North Am.*, 1951, **35**, 519–533.

28 A. V Belyakov and N. A. Kulikov, Methods for synthesizing yttrium-aluminum garnet nanopowders from solutions, *Refract. Ind. Ceram.*, 2011, **52**, 155–158.

29 D. Bersani, S. Ando, P. Vignola, G. Moltifiori, I. Marino, P. Paolo and V. Diella, Molecular and biomolecular spectroscopy micro-Raman spectroscopy as a routine tool for garnet analysis, *Spectrochim. Acta Part A*, 2009, **73**, 484–491.

30 D. F. Castro, C. Santos, J. K. M. F. Daguano, D. Rodrigues, P.A. Suzuki, Yttrium aluminum garnet (YAG) obtained by rare-earth mixed oxide (RE_2O_3), *C. Bras.*, 2010, **19**, 1195–1206.

31 R. Yavetskiy, M. G. Ivanov, B. Liu, J. Li, R. Yavetskiy, M. Ivanov, Y. Zeng and T. Xie, Fabrication of YAG transparent ceramics using carbonate precipitated yttria powder Fabrication of YAG transparent ceramics using carbonate precipitated yttria powder, *J. Eur. Ceram. Soc.*, 2015, **35**, 2379–2390.

32 J. Liu, X. Cheng, J. Li, T. Xie, M. Ivanov, X. Ba, H. Chen, Q. Liu, Y. Pan and J. Guo, Influence of non-stoichiometry on solid-state reactive sintering of YAG transparent ceramics, *J. Eur. Ceram. Soc.*, 2015, **35**, 3127–3136.

33 H. Haneda, I. Sakaguchi, N. Ohashi, N. Saito, K. Matsumoto, T. Nakagawa, T. Yanagitani and H. Yagi, Evaluation of oxide ion diffusivity in YAG ceramics, *Mater. Sci. Technol.*, 2009, **25**, 1341–1345.

34 D. Hreniak, W. Strek, P. Mazur, R. Pazik and M. Zabkowska-Waclawek, Luminescence properties of Tb^{3+}:$Y_3Al_5O_{12}$ nanocrystallites prepared by the sol-gel method, *Opt. Mater. (Amst).*, 2004, **26**, 117–121.

35 A. Katelnikovas, P. Vitta, P. Pobedinskas, G. Tamulaitis, A. Zukauskas, J. E. Jorgensen and A. Kareiva, Photoluminescence in sol-gel-derived YAG:Ce phosphors, *J. Cryst. Growth*, 2007, **304**, 361–368.

36 R. Skaudzius, A. Katelnikovas, D. Enseling, A. Kareiva and T. Justel, Dependence of the $^5D_0 \rightarrow {}^7F_4$ transitions of Eu^{3+} on the local environment in phosphates and garnets, *J. Lumin.*, 2014, **147**, 290–294.

37 A. Zabiliute-Karaliune, H. Dapkus, R. P. Petrauskas, S. Butkute, A. Zukauskas and A. Kareiva, Cr^{3+} doped yttrium gallium garnet for phosphor-conversion light emitting diodes, *Lith. J. Phys.*, 2015, **55**, 200–207.

38 W. Zhang, H. Liu, S. Yh, Q. Hm, J. Tan, Synthesis of nano-sized and highly sinterable Nd:YAG powders by the urea homogeneous precipitation method, *Powder Technol.*, 2012, **217**, 140–147.

39 H. Yang, X. Qin, J. Zhang, S. Wang, J. Ma, L. Wang and Q. Zhang, Fabrication of Nd:YAG transparent ceramics with both TEOS and MgO additives, *J. Alloys Compd.*, 2011, **509**, 5274–5279.

40 H. Yihua, J. Dongliang, Z. Jingxian and L. I. N. Qingling, Sintering of transparent Nd:YAG ceramics in oxygen atmosphere, *J. Rare Earths*, 2013, **31**, 153–157.

41 L. Ge, J. Li, Z. Zhou, H. Qu, M. Dong, Y. Zhu, W. Li, M. Chen, H. Kou, Y. Shi, Y. Pan and X. Feng, Fabrication of composite YAG/Nd:YAG/YAG transparent ceramics for planar waveguide laser, *Opt. Mater. Express*, 2014, **4**, 3586–3588.

42 L. An, A. Ito and T. Goto, Fabrication of transparent lutetium oxide by spark plasma sintering, *J. Am. Ceram. Soc.*, 2011, **698**, 695–698.

43 L. Z. Pan, B. Jiang, J. Fan, Q. Yang, C. Zhou, P. Zhang, X. Mao, L. Zhang, Preparation of LuAG powders with single phase and good dispersion for transparent ceramics using co-precipitation method, *Materials (Basel).*, 2015, **8**, 5363–5375.

44 W. Si, C. Ding and S. Ding, Synthesis and characterization of YAG nanoparticles by alkoxide hydrolysis precipitation methods, *J. Nanomater.*, 2014, **2014**, 1–8.

45 Y. C. Kang, I. W. Lenggoro, S. B. Park, K. Okuyama, YAG:Ce phosphor particles prepared by ultrasonic spray pyrolysis YAG:Ce phosphor particles prepared by ultrasonic spray pyrolysis, *Mater. Res. Bull.*, 2000, **35**, 789–798.

46 Y. C. Kang, Y. S. Chung and S. Bin Park, Preparation of YAG: europium red phosphors by spray pyrolysis using a filter-expansion aerosol generator, *J. Am. Ceram. Soc.*, 1999, **60**, 2056–2060.

47 J. Young, H. Chae, G. S. Rama, J. Hyun, B. Kee, J. Hwan and Y. Kuk, Solvothermal synthesis and luminescence properties of the novel aluminum garnet phosphors for WLED applications, *Curr. Appl. Phys.*, 2013, **13**, 441–447.

48 L. Xing, L. Peng, M. Gu and G. Tang, Solvothermal synthesis of lutetium aluminum garnet nanopowders: determination of the optimum synthesis conditions, *J. Alloys Compd.*, 2010, **491**, 599–604.

49 J. Young Park, H. Chae Jung, G. Seeta Rama Raju, B. Kee Moon, J. H. Jeong and J. Hwan Kim, Solvothermal synthesis and luminescence properties of Tb^{3+}-doped gadolinium aluminum garnet, *J. Lumin.*, 2010, **130**, 478–482.

50 Z. Fu and B. Liu, Solution combustion synthesis, photoluminescence and X-ray luminescence of Eu^{3+}-doped $LaAlO_3$ nanophosphors, *Ceram. Int.*, 2016, **42**, 2357–2363.

51 G. Xia, S. Zhou, J. Zhang and J. Xu, Structural and optical properties of $YAG:Ce^{3+}$ phosphors by sol-gel combustion method, *J. Cryst. Growth*, 2005, **279**, 357–362.

52 J. Li, F. Chen, W. Liu, W. Zhang, L. Wang, X. Ba, Y. Zhu, Y. Pan and J. Guo, Co-precipitation synthesis route to yttrium aluminum garnet (YAG) transparent ceramics, *Eur. Ceram. Soc.*, 2012, **32**, 2971–2979.

53 E. M. Loiko, L. Lipieska, J.Cz. Dobrowolski, A. Rzepka, Studies on sol-gel processes accompanying formation of the yttrium aluminum garnet, *Materyaly Elektron.*, 2006, **3**, 74–88.

54 J. M. Boulton, G. Teowee and D. R. Uhlmann, New optical materials by wet chemical processing, *J. Non. Cryst. Solids*, 1996, **3093**, 26–36.

55 A. Ikesue, Polycrystalline Nd :YAG ceramics lasers, 2002, **19**, 183–187.

56 R. Mann, K. Laishram, S. A. Ahmed, K. Zimik and N. Malhan, Sol freeze dry nd:YAG nanopowder synthesis and sinterability studies, *Def. Sci. J.*, 2015, **65**, 418–422.

57 T. Hussain, L. Zhong, M. Danesh, H. Ye, Z. Liang, D. Xiao, C.-W. Qiu, C. Lou, L. Chi and L. Jiang, Enabling low amounts of $YAG:Ce^{3+}$ to convert blue into white light with plasmonic Au nanoparticles, *Nanoscale*, 2015, **7**, 10350–10356.

58 X. Wu, Y. Tao, C. Song, C. Mao, L. Dong and J. Zhu, Morphological control and luminescent properties of YVO_4:Eu Nanocrystals, *J. Phys. Chem. B*, 2006, **110**, 15791–15796.

59 G. Yi, H. Lu, S. Zhao, Y. Ge and W. Yang, Synthesis, characterization, and biological application of size-controlled nanocrystalline $NaYF_4$:Yb,Er phosphors, *Nano Lett.*, 2004, **4 (11)**, 2191–2196.

60 G. Yi, B. Sun, F. Yang, D. Chen, Y. Zhou and J. Cheng, Synthesis and characterization of high-efficiency nanocrystal up-conversion phosphors: ytterbium and erbium codoped lanthanum molybdate, *Chem. Mater*, 2013, **14**, 2910–2914.

61 D. Guo, B. Ma, L. Zhao, J. Qiu, W. Liu, Y. Sang, J. Claverie and H. Liu, Bright YAG:Ce nanorod phosphors prepared via a partial wet chemical route and biolabeling applications, *ACS Appl. Mater. Interfaces*, 2016, **8**, 11990–11997.

62 Y. Zhang, M. Cai, B. Jiang, J. Fan, C. Zhou and L. Zhang, Micro-structure of grain boundary in post-annealed Sinter plus HIPed Nd:$Lu_3Al_5O_{12}$ ceramics, *Opt. Mater. Express*, 2014, **4**, 1927–1933.

63 J. Li, Y. Wu, Y. Pan, W. Liu, L. An, S. Wang and J. Guo, Solid-state-reaction fabrication and properties of a high-doping Nd:YAG transparent laser ceramic, *Front. Chem. Eng. China*, 2008, **2**, 248–252.

64 J. Li, W. Liu, B. Jiang, J. Zhou, W. Zhang, L. Wang, Y. Shen, Y. Pan and J. Guo, Synthesis of nanocrystalline yttria powder and fabrication of Cr,Nd:YAG transparent ceramics, *J. Alloys Compd.*, 2012, **515**, 49–56.

65 S. Kochawattana, A. Stevenson, S. Lee, M. Ramirez, V. Gopalan, J. Dumm, V. K. Castillo, G. J. Quarles and G. L. Messing, Sintering and grain growth in SiO_2 doped Nd :YAG, *J. Eur. Ceram. Soc.*, 2008, **28**, 1527–1534.

66 A. Ikesue, Optical scattering centers in polycrystalline Nd:YAG Laser, *J. Am. Ceram. Soc.*, 1997, **22**, 1517–1522.

67 H. Wang, H. Huang, P. Liu, L. Jin, D. Shen, J. Zhang and D. Tang, Diode-pumped continuous-wave and Q-switched Tm:Y_2O_3 ceramic laser around 2050 nm, *Opt. Mater. Express*, 2017, **7**, 597–600.

68 Y. Fu, J. Li, Y. Liu, L. Liu, H. Zhao and Y. Pan, Effect of air annealing on the optical properties and laser performance of Nd:YAG transparent ceramics, *Opt. Mater. Express*, 2014, **4**, 2108–2115.

69 T. Feng, J. Shi and D. Jiang, Optical properties of transparent Pr:YAG ceramic, *Cer. Inter*, 2009, **35**, 427–431.

70 L. Mancic, K. Marinkovic, B. A. Marinkovic, M. Dramicanin and O. Milosevic, YAG:Ce^{3+} nanostructured particles obtained via spray pyrolysis of polymeric precursor solution, *J. Eur. Ceram. Soc.*, 2010, **30**, 577–582.

71 T. Vanneste, A. Van Lantschoot, K. Van Boxem, J. Van Zundert, YAG:Ce^{3+} nanostructured particles obtained via spray pyrolysis of polymeric precursor solution, *J. Eur. Ceram. Soc.*, 2017, **30**, 577–582.

72 S. Gao, Y. Chen and R. Zeng, Synthesis of agglomerate-free YAG:Ce^{3+} phosphors by co-precipitation and low temperature spray pyrolysis, *Adv. Packag. Mater.*, 2011, **12**, 112–116.

73 S. Chawla, T. Roy, K. Majumder and A. Yadav, Red enhanced YAG:Ce,Pr nanophosphor for white LEDs, *J. Exp. Nanosci.*, 2017, **9**, 776–784.

74 M. Pechini, Barium Titanium Citrate, Barium titanate and processes for producing same, 1966, US Patent 3231328.

75 Z. Huashan, H. U. I. Han, S. U. Chunhui and Z. Hongbo, Effect of heat treatment on crystallization of Nd:YAG Ceramics, *J. Wuhan Univ. Technol. Sci. Ed.*, 2007, 333–336.

76 F. Qiu, X. Pu, J. Li, X. Liu, Y. Pan and J. Guo, Thermal behavior of the YAG precursor prepared by sol–gel combustion process, *Ceram. Int.*, 2005, **31**, 663–665.

77 J. Li, Y. Pan, F. Qiu and Y. Wu, Synthesis of nanosized Nd:YAG powders via gel combustion, *Ceram. Int.*, 2007, **33**, 1047–1052.

78 Y. Rabinovitch, C. Bogicevic, F. Karolak, D. Tetard and H. Dammak, Freeze-dried nanometric neodymium-doped YAG powders, *J. Mater. Process. Technol.*, 2008, **199**, 314–320.

79 D. N. Chung, D. N. Hieu, T. T. Thao, V. Truong and N. N. Dinh, Synthesis and characterization of Ce-doped $Y_3Al_5O_{12}$ (YAG:Ce) nanopowders used for solid-state lighting, *J. Nanomater.*, 2014, **2014**, 1–7.

80 S. S. Yattinahalli, S. B. Kapatkar and S. N. Mathad, Review of nanoscience materials and its applications, *Res. J. Eng. Tech.*, 2016, **7**, 121–127.

81 E. V Zharikov, D. A. Lis, K. A. Subbotin, V. B. Dudnikova and O. N. Zaitseva, Growth of oxide laser crystals by czochralski method, *Acta Phys. Pol. A*, 2013, **124**, 274–285.

82 E. V. Zharikov, Problems and recent advances in melt crystal growth technology, *J. Cryst. Growth*, 2012, **360**, 146–154.

83 W. Hairul and A. Kamaruddin, The growth of Nd:YAG single crystals by czochralski method with ADC-CGS – preliminary work, *Appl. Phys. Res.*, 2010, **2**, 135–138.

84 M. O. Ramirez, J. Wisdom, H. Li, Y. L. Aung, J. Stitt, L. Messing, V. Dierolf, Z. Liu, A. Ikesue and R. L. Byer, Three-dimensional grain boundary spectroscopy in transparent high power ceramic laser materials, *Opt. Express*, 2008, **16**, 5965–5973.

85 D. Kracht, D. Freiburg, R. Wilhelm and M. Frede, Core-doped ceramic Nd:YAG Laser, *Opt. Express*, 2010, **14**, 2690–2694.

86 G. Boulon, C. Bernard and G. Boulon, Fifty Years of Advances in solid-state laser materials fifty years of advances in solid-state laser materials, *Opt. Mater. (Amst).*, 2014, **34**, 499–512.

87 J. Dong, J. Ma, K. Kaminskii and A. A. Ueda, Optimization of Yb:YAG/Cr^{4+}:YAG composite ceramics passively Q-switched microchip lasers, *Appl. Phys. B*, 2011, **105**, 749–760.

88 L. Jaffres, A. Labruy, V. Couderc, J. Carreaud, A. Ma, A. Brenier, G. Boulon, Y. Guyot and C. Sall, Gain structuration in dual-wavelength Nd:YSAG ceramic lasers, *Opt. Express*, 2012, **20**, 25596–25602.

89 T. Saiki, M. Nakatsuka, K. Fujioka, S. Motokoshi and K. Imasaki, Cross-relaxation and spectral broadening of gain for Nd/Cr:YAG ceramic lasers with white-light pump source under high-temperature operation, *Opt. Commun.*, 2011, **284**, 2980–2984.

90 S. Ebrahim and G. Rezaei, Optik Shift and broadening of quasi three level emission lines in Nd^{3+}:YAG laser crystal influenced by input energy, *Opt. - Int. J. Light Electron Opt.*, 2015, **126**, 3939–3941.

91 H. Xu, D. Ying, A. Lu, X. Wang and J. Hu, Surfactant-assistant solvothermal synthesis of $CaWO_4$:Eu^{3+} phosphors and luminescence, *Superlattices Microstruct.*, 2015, **83**, 668–675.

92 H. Nakao, A. Shirakawa, K. Ueda, A. A. Kaminskii, S. Kuretake, N. Tanaka, Y. Kintaka, K. Kageyama, H. Yagi and T. Yanagitani, Investigation of the laser and optical properties of Nd^{3+}:Ba(Zr,Mg,Ta)O_3 ceramic, Nd^{3+}(Na^+):$Ca_2MgSi_2O_7$ single crystal, and Yb^{3+}:$Lu_3Al_5O_{12}$ ceramic, *Opt. Mater. (Amst).*, 2013, **35**, 700–703.

93 P. Samuel, G. A. Kumar, Y. Takagimi, Y. Hideki, I. U. Ken and S. Moorthy Babu, Efficient energy transfer between Ce^{3+}/Cr^{3+} and Nd^{3+} ions in transparent Nd/Ce/Cr:YAG ceramics, *Opt. Mater. (Amst).*, 2011, **34**, 303–307.

94 Y. Li, S. Zhou, H. Lin, X. Hou and W. Li, Intense 1064nm emission by the efficient energy transfer from Ce^{3+} to Nd^{3+} in Ce/Nd co-doped YAG transparent ceramics, *Opt. Mater. (Amst).*, 2010, **32**, 1223–1226.

95 M. Sokol, S. Kalabukhov, V. Kasiyan, A. Rothman, M. P. Dariel and N. Frage, Mechanical, thermal and optical properties of the SPS-processed polycrystalline Nd:YAG, *Opt. Mater. (Amst).*, 2014, **38**, 204–210.

96 V. Lupei, A. Lupei, C. Gheorghe and A. Ikesue, Emission sensitization processes involving Nd^{3+} in YAG, *J. Lumin.*, 2016, **170**, 594–601.

97 X. Li, Q. Li, J. Wang, S. Yang and H. Liu, Synthesis of Nd^{3+} doped nano-crystalline yttrium aluminum garnet (YAG) powders leading to transparent ceramic, *Opt. Mater. (Amst).*, 2007, **29**, 528–531.

98 T. Rao, A. R. Kumar, K. Neeraja, N. Veeraiah and M. Rami Reddy, Optical and structural investigation of Eu^{3+} ions in Nd^{3+} co-doped magnesium lead borosilicate glasses, *J. Alloys Compd.*, 2013, **557**, 209–217.

99 W. Zhang, T. Lu, B. Ma, N. Wei, Z. Lu, F. Li, Y. Guan, X. Chen, W. Liu and L. Qi, Improvement of optical properties of Nd:YAG transparent

ceramics by post-annealing and post hot isostatic pressing, *Opt. Mater. (Amst).*, 2013, **35**, 2405–2410.

100 W. Zhang, T. Lu, N. Wei, B. Ma, F. Li, Z. Lu and J. Qi, Effect of annealing on the optical properties of Nd:YAG transparent ceramics, *Opt. Mater. (Amst).*, 2012, **34**, 685–690.

101 B. Liu, J. Li, M. Ivanov, W. Liu, L. Ge, T. Xie, H. Kou, S. Zhuo, Y. Pan and J. Guo, Diffusion-controlled solid-state reactive sintering of Nd:YAG transparent ceramics, *Ceram. Int.*, 2015, **41**, 11293–11300.

102 J. Chen, J. Li, J. Xu, W. Liu, Y. Bo, X. Feng, Y. Xu, D. Jiang, Z. Chen, Y. Pan, Y. Guo, B. Yan, C. Guo, L. Yuan, H. Yuan, Y. Lin, Y. Xiao, Q. Peng, W. Lei, D. Cui and Z. Xu, 4350W quasi-continuous-wave operation of a diode face-pumped ceramic Nd:YAG slab laser, *Opt. Laser Technol.*, 2014, **63**, 50–53.

103 H. Yagi, T. Yanagitani, K. Takaichi, K. Ueda and A. A. Kaminskii, Characterizations and laser performances of highly transparent Nd^{3+}:$Y_3Al_5O_{12}$ laser ceramics, *Opt. Mater. (Amst).*, 2007, **29**, 1258–1262.

104 W. Guo, Y. Cao, Q. Huang, J. Li, J. Huang, Z. Huang and F. Tang, Fabrication and laser behaviors of Nd:YAG ceramic microchips, *J. Eur. Ceram. Soc.*, 2011, **31**, 2241–2246.

105 M. Zhang, R. Zhu, M. Zhang and S. Wang, Creation of an ethanol-tolerant saccharomyces cerevisiae strain by 266 nm laser radiation and repetitive cultivation., *J. Biosci. Bioeng.*, 2014, **118**, 508–513.

106 A. Kearns, C. Fischer, K. G. Watkins, M. Glasmacher, H. Kheyrandish, A. Brown, W. M. Steen and P. Beahan, Laser removal of oxides from a copper substrate using Q-switched Nd:YAG radiation at 1064 nm, 532 nm and 266 nm, *Appl. Surf. Sci.*, 1998, **127**–**129**, 773–780.

107 L. Tunna, A. Kearns, W. O'Neill and C. J. Sutcliffe, Micromachining of copper using Nd:YAG laser radiation at 1064, 532, and 355 nm wavelengths, *Opt. Laser Technol.*, 2001, **33**, 135–143.

108 S. K. Gupta, N. Pathak and R. M. Kadam, An efficient gel-combustion synthesis of visible light emitting barium zirconate perovskite nanoceramics:

probing the photoluminescence of Sm^{3+} and Eu^{3+} doped $BaZrO_3$, *J. Lumin.*, 2016, **169**, 106–114.

109 J. Hou, X. Yin, Y. Fang, F. Huang and W. Jiang, Novel red-emitting perovskite-type phosphor $CaLa_{1-x}MgMO_6$:xEu^{3+} (M= Nb,Ta) for white LED application, *Opt. Mater. (Amst).*, 2012, **34**, 1394–1397.

110 C. Sommer, P. Hartmann, P. Pachler, H. Hoschopf and F. P. Wenzl, White light quality of phosphor converted light-emitting diodes: A phosphor materials perspective of view, *J. Alloys Compd.*, 2012, **520**, 146–152.

111 Q. Y. Zhang and X. Y. Huang, Recent progress in quantum cutting phosphors, *Prog. Mater. Sci.*, 2010, **55**, 353–427.

112 S. R. Naik, T. Shripathi and A. V Salker, Preparation , characterization and photoluminescent studies of Cr and Nd co-doped Ce:YAG compounds, *J. Lumin.*, 2015, **161**, 335–342.

113 H. K. Yang, H. M. Noh and J. H. Jeong, Low temperature synthesis and luminescence investigations of YAG:Ce, Eu nanocomposite powder for warm white light-emitting diode, *Solid State Sci.*, 2014, **27**, 43–46.

114 F. A. S. Elim, A. K. Hamehchi, D. W. Inarski and S. A. Garwal, Synthesis and characterization of Ce:YAG nano-phosphors and ceramics, *Opt. Mater. Express*, 2016, **6**, 35–45.

115 H. H. Kwak, S. J. Kim, Y. S. Park, H. H. Yoon, S. J. Park and H. W. Choi, Photoluminescence characteristic of Ce^{3+}-Eu^{3+} Co-doped $Y_3Al_5O_{12}$ phosphor prepared by combustion method, *Mol. Cryst. Liq. Cryst.*, 2009, **513**, 106–113.

116 X. Qu, L. Cao, W. Liu, G. Su, P. Wang and I. Schultz, Sol-gel synthesis of long-lasting phosphors $CdSiO_3$:Mn^{2+}, RE^{3+} (RE=Tb,Eu,Nd) and luminescence mechanism research, *Mater. Res. Bull.*, 2012, **47**, 1598–1603.

117 R. S. Yadav, V. K. Shukla, P. Mishra, S. K. Pandey, K. Kumar, V. Baranwal, M. Kumar and A. C. Pandey, Enhanced blue luminescence in $BaMgAl_{10}O_{17}$:Eu, Er, Nd nanophosphor for PDPs and mercury free fluorescent lamps, *J. Alloys Compd.*, 2013, **547**, 1–4.

118 T. Samanta, S. Sarkar, V. N. K. B. Adusumalli, A. E. Praveen and V. Mahalingam, Enhanced visible and near infrared emissions via Ce^{3+} to Ln^{3+} energy transfer in Ln^{3+}-doped CeF_3 nanocrystals (Ln=Nd and Sm), *Dalt. Trans.*, 2016, **45**, 78–84.

119 D. Ghosh, P. Karmakar, K. Biswas, S. Balaji, A. D. Sontakke and K. Annapurna, Variance of energy transfer dynamics in Ce^{3+} sensitized Eu^{3+} and Tb^{3+} doped alkali free Ba-Al metaphosphate glass: role of the host matrix, *Phys. Chem. Glas. Eur. J. Glas. Sci. Technol. Part B.*

120 Y. Zhao, H. Xu, X. Zhang, G. Zhu, D. Yan, Q. Ling, M. Chen and A. Yu, Optical performances of YAG:Re^{3+} (Re=Ce, Eu) phosphor films with co- doping Tb^{3+} as energy- transfer sensitizer, *J. Am. Ceram. Soc.*, 2016, **99**, 756–759.

121 V. A. Pustovarov and I. N. Ogorodnikov, Ultraviolet-visible spectroscopic characterization of lanthanum beryllate crystals doped with Er, Nd, or Pr ions, *J. Surf. Investig. X-ray, Synchrotron Neutron Tech.*, 2016, **10**, 48–57.

122 A. Lupei, V. Lupei and C. Gheorghe, Electronic structure of Sm^{3+} ions in YAG and cubic sesquioxide ceramics, *Opt. Mater. (Amst).*, 2013, **36**, 419–424.

123 C. Gheorghe, A. Lupei, S. Hau, F. Voicu, L. Gheorghe and A. M. Vlaicu, Compositional dependence of optical properties of Sm^{3+}-doped $Y_3Sc_xAl_{5-x}O_{12}$ polycrystalline ceramics, *J. Alloys Compd.*, 2016, **683**, 547–553.

124 V. M. Longo, M. das G. S. Costa, A. Z. Simoes, I. L. V. Rosa, C. O. P. Santos, J. Andres, E. Longo and J. A. Varela, On the photoluminescence behavior of samarium-doped strontium titanate nanostructures under UV light. Structural and electronic understanding, *Phys. Chem. Chem. Phys.*, 2010, **12**, 7566–7579.

125 A. Lupei, V. Lupei and C. Gheorghe, Thermal shifts of Sm^{3+} lines in YAG and cubic sesquioxide ceramics, *Opt. Mater. Express*, 2013, **3**, 626–628.

126 K. Naveen Kumar, Enhanced photoluminescence spectra of Sm^{3+} co-doped with Tb^{3+} in PEO + PVP blended polymer films, *AIP Conf. Proc.*, 2015, **1665**, 3–7.

127 H. Shi, C. Zhu, J. Huang, J. Chen, D. Chen, W. Wang, F. Wang, Y. Cao and X. Yuan, Luminescence properties of YAG :Ce, Gd phosphors synthesized under vacuum condition and their white LED performances, *Opt. Mater. (Amst).*, 2014, **4**, 199–202.

128 D. Liu, T. Troczynski and W. J. Tseng, Water-based sol-gel synthesis of hydroxyapatite: process development, *Biomaterials*, 2001, **22**, 1721–1730.

129 S. Hosokawa, Y. Tanaka, S. Iwamoto and M. Inoue, Defect structure of rare earth aluminium garnets obtained by the glycothermal method, *J. Alloys Compd.*, 2008, **451**, 309–313.

130 D. A. Hora, A. B. Andrade, N. S. Ferreira, V. C. Teixeira and M. V. S. Rezende, X-ray excited optical luminescence of Eu-doped YAG nanophosphors produced via glucose sol–gel route, *Ceram. Int.*, 2016, **42**, 10516–10519.

131 R. Reisfeld, Prospects of sol–gel technology towards luminescent materials, *Opt. Mater. (Amst).*, 2001, **16**, 1–7.

132 T. Lopez, M. Alvarez, P. Ramirez, G. Jardon and M. Lopez, Sol-gel silica matrix as reservoir for controlled release of paracetamol: characterization and kinetic Analysis, *J. Encapsulation Adsorpt. Sci.*, 2016, **6**, 47–55.

133 J. Legendziewicz, W. Stre, J. Sokolnicki, D. Hreniak and V. Zolin, Optical properties of Nd^{3+} in silica ceramics obtained by the sol–gel method, *Opt. Mater. (Amst).*, 2002, **19**, 175–181.

134 S. Pfeifer, M. Bischoff, R. Niewac, B. Clausb and M. R. Buchmeiser, Structure formation in yttrium aluminum garnet (YAG) fibers, *J. Eur. Ceram. Soc.*, 2014, **34**, 1321–1328.

135 M. Zarzecka-Napierala and K. Haberko, Synthesis and characterization of yttrium aluminium garnet (YAG) powders, *Process. Appl. Ceram.*, 2007, **1**, 69–74.

136 P. S. Devi, Y. Lee, J. Margolis, J. B. Parise, S. Sampath, H. Herman and J. C. Hanson, Comparison of citrate–nitrate gel combustion and precursor plasma spray processes for the synthesis of yttrium aluminum garnet, *J. Mater. Res.*, 2002, **17**, 2846–2851.

137 Y. Dimitriev, Y. Ivanova and R. Iordanova, History of sol-gel sciense and technology (review), *J. Univ. Chem. Technol. Metall.*, 2008, **42**, 181–192.

138 T. Chudoba, E. Lester, W. Lojkowski, M. Poliakoff and J. Li, Synthesis of nano-sized yttrium-aluminum garnet in a continuous-flow reactor in supercritical fluids, *Zeitschrift fur Naturforsch. B*, 2008, **63**, 756–764.

139 A. M. Chinie, A. Stefan and S. Georgescu, Synthesis by a citrate sol-gel method and characterization of Eu3+ -doped ytrium aluminum garnet nanocrystals, *Rom. Reports Phys.*, 2005, **57**, 412–417.

140 A. E. Danks, S. R. Hall and Z. Schnepp, Materials Horizons technique for materials synthesis, *Mater. Horizons*, 2016, **3**, 91–112.

141 G. Zatryb, a. Podhorodecki, J. Serafinczuk, M. Motyka, M. Banski, J. Misiewicz and N. V. Gaponenko, Optical properties of Tb and Eu doped cubic $YAlO_3$ phosphors synthesized by sol–gel method, *Opt. Mater. (Amst).*, 2013, **35**, 2090–2094.

142 E. W. Barrera, M. C. Pujol, J. J. Carvajal, X. Mateos, R. Sole, J. Massons, A. Speghini, M. Bettinelli, C. Cascales, M. Aguilo and F. Diaz, White light upconversion in Yb-sensitized (Tm, Ho)-doped $KLu(WO_4)_2$ nanocrystals: the effect of Eu incorporation, *Phys. Chem. Chem. Phys.*, 2014, **16**, 1679–86.

143 G. Demazeau, Solvothermal reactions: an original route for the synthesis of novel materials, *J. Mater. Sci.*, 2008, **43**, 2104–2114.

144 H. Chen, S. M. Yu, D. W. Shin and J. B. Yoo, Solvothermal synthesis and characterization of chalcopyrite $CuInSe_2$ nanoparticles, *Nanoscale Res. Lett.*, 2010, **5**, 217–223.

145 M. Nazarov and D. Y. Noh, New generation of europium- and terbium-activated phosphors: from syntheses to applications, *Pan Stanford Publ.*, 2011, 1–300.

146 P. Palmero and R. Traverso, Co-precipitation of YAG powders for transparent materials: effect of the synthesis parameters on processing and microstructure, *Materials (Basel).*, 2014, **7**, 7145–7156.

147 Y. Liu, M. Sun, Y. Liu, G. Chen and X. Zhang, Effects of aging time on phase, morphology, and luminescence by two-photon processes of $BiPO_4:Er^{3+},Yb^{3+}$ in the solvothermal synthesis, *Opt. Mater. (Amst).*, 2015, **45**, 32–36.

148 G. Jia, Y. Song, M. Yang, Y. Huang, L. Zhang and H. You, Uniform $YVO_4:Ln^{3+}$(Ln=Eu, Dy and Sm) nanocrystals : solvothermal synthesis and luminescence properties, *Opt. Mater. (Amst).*, 2009, **31**, 1032–1037.

149 Z. Li, G. Wang, Q. Yang, Z. Shao and Y. Wang, Synthesis and electrical property of metal/ZnO coaxial nanocables, *Nanoscale Res. Lett.*, 2012, **7**, 1–9.

150 L. Liping, Z. Minglei, T. Wenming, G. Xiangfeng, L. Guangshe and Y. Liusai, Preparation of cereal-like $YVO_4:Ln^{3+}$ (Ln=Sm, Eu, Tb, Dy) for high quantum efficiency photoluminescence, *Nanotechnology*, 2010, **21**, 195601 (8pp)

151 S. Komarneni, Y. Dong, J. Young and S. Han, Solvothermal/hydrothermal synthesis of metal oxides and metal powders with and without microwaves, *Z. Naturforsch.*, 2010, **65b**, 1033–1037.

152 S. Li, T. Zhang, R. Tang, H. Qiu, C. Wang and Z. Zhou, Solvothermal synthesis and characterization of monodisperse superparamagnetic iron oxide nanoparticles, *J. Magn. Magn. Mater.*, 2015, **379**, 226–231.

153 S. Hosokawa, Synthesis of metal oxides with improved performance using a solvothermal method, *J. Ceram. Soc. Japan*, 2016, **124**, 870–874.

154 J. Lai, W. Niu, R. Luque and G. Xu, Solvothermal synthesis of metal nanocrystals and their applications, *Nano Today*, 2015, **10**, 240–267.

155 J. Yin, J. Jia, W. W. Lestari and M. Adreane, Synthesis of $AgInS_2$ semiconductor nano crystals by solvothermal method, 2015, **73**, 0–4.

156 G. Zou, H. Li, Y. Zhang, K. Xiong, Y. Qian, Solvothermal/hydrothermal route to semiconductor nanowires, *Nanotechnology*, 2006, **17**, 313–320.

157 N. Dubnikova, E. Garskaite, R. Raudonis and A. Kareiva, Neodymium substitution effects in sol e gel derived $Y_{3-x}Nd_xAl_5O_{12}$, *Mater. Chem. Phys.*, 2012, **137**, 660–664.

158 Y. Zorenko, V. Gorbenko, T. Zorenko, P. Popielarski, L. Mosinska and A. Fedorov, Luminescent and scintillation properties of the Ce^{3+} doped $Y_{3-x}Lu_xAl_5O_{12}$:Ce single crystalline films, *J. Lumin.*, 2016, **169**, 822–827.

159 Y. Sang, H. Liu, Y. Lv, J. Wang, T. Chen, D. Liu, X. Zhang, H. Qin, X. Wang and R. I. Boughton, Yttrium aluminum garnet nanoparticles synthesized by nitrate decomposition and their low temperature densification behavior, *J. Alloys Compd.*, 2010, **490**, 459–462.

160 X. Qin, H. Yang, G. Zhou, D. Luo, J. Zhang, S. Wang and J. Ma, Synthesis of submicron-sized spherical Y_2O_3 powder for transparent YAG ceramics, *Mater. Res. Bull.*, 2011, **46**, 170–174.

161 Y. Sang, H. Liu, X. Sun, X. Zhang, H. Qin, Y. Lv, D. Huo, D. Liu, J. Wang and R. I. Boughton, Formation and calcination temperature-dependent sintering activity of YAG precursor synthesized via reverse titration method, *J. Alloys Compd.*, 2011, **509**, 2407–2413.

162 N. Pradal, G. Chadeyron, A. Potdevin, J. Deschamps and R. Mahiou, Elaboration and optimization of Ce-doped $Y_3Al_5O_{12}$ nanopowder dispersions, *J. Eur. Ceram. Soc.*, 2013, **33**, 1935–1945.

163 R. Skaudzius, A. Selskis, J. Pinkas and A. Kareiva, Synthesis and evolution of crystalline garnet phases in $Y_3Al_{5-x}In_xO_{12}$, *J. Phys. Conf. Ser.*, 2007, **93**, 12003.

164 G. Raju, S. Rama and S. Buddhudu, Emission analysis of Tb^{3+}:$MgLaLiSi_2O_7$ powder phosphor, *Mater. Lett.*, 2008, **62**, 1259–1262.

165 R. Srinivasan, N. R. Yogamalar, J. Elanchezhiyan, R. J. Joseyphus and A. C. Bose, Structural and optical properties of europium doped yttrium oxide

nanoparticles for phosphor applications, *J. Alloys Compd.*, 2010, **496**, 472–477.

166 S. K. Singh, D. G. Lee, S. S. Yi, K. Jang and D. Shin, Probing dual mode emission of Eu^{3+} in garnet phosphor, *J. Appl. Phys.*, 2013, **113**, 173504–7.

167 R. E. Muenchausen, L. G. Jacobsohn, B. L. Bennett, E. A. McKigney, J. F. Smith, J. A. Valdez and D. W. Cooke, Effects of Tb doping on the photoluminescence of Y_2O_3:Tb nanophosphors, *J. Lumin.*, 2007, **126**, 838–842.

168 C. Santos, J. K. M. F. Daguano, D. Rodrigues, P. A. Suzuki, F. A. Santos and O. M. M. Silva, Synthesis of a mixed-rare-earth aluminum garnet solid solution, *Mater. Lett.*, 2013, **91**, 283–286.

169 D. Wang, S. Tie and X. Wan, White light emitting from $YVO_4/Y_2O_3:Eu^{3+},Bi^{3+}$ composite phosphors for UV light-emitting diodes, *Ceram. Int.*, 2015, **41**, 7766–7772.

170 A. N. Meza-Rocha, R. Lozada-Morales, A. Speghini, M. Bettinelli and U. Caldino, White light generation in $Tb^{3+}/Eu^{3+}/Dy^{3+}$ triply-doped $Zn(PO_3)_2$ glass, *Opt. Mater. (Amst).*, 2016, **51**, 128–132.

171 Z. Wang, M. Xu, W. Zhang and M. Yin, Synthesis and luminescent properties of nano-scale LuAG:RE^{3+}(Ce, Eu) phosphors prepared by co-precipitation method, *J. Lumin.*, 2007, 1–6.

172 J. Li, J. G. Li, Z. Zhang, X. Wu, S. Liu, X. Li, X. Sun and Y. Sakka, Effective lattice stabilization of gadolinium aluminate garnet (GdAG) via Lu^{3+} doping and development of highly efficient (Gd,Lu)AG:Eu^{3+} red phosphors, *Sci. Technol. Adv. Mater.*, 2012, **13**, 035007 (9pp).

173 S. Fuentes, N. Barraza, E. Veloso, R. Villarroel and J. Llanos, Effects of Eu substitution on luminescent and magnetic properties of $BaTiO_3$ nanomaterials, *J. Alloys Compd.*, 2013, **569**, 52–57.

174 R. Narro-Garcia, H. Desirena, T. Lopez-Luke, J. Guerrero-Contreras, C. K. Jayasankar, R. Quintero-Torres and E. De la Rosa, Spectroscopic properties

of Eu^{3+}/Nd^{3+} co-doped phosphate glasses and opaque glass–ceramics, *Opt. Mater. (Amst).*, 2015, **46**, 34–39.

175 G. Seeta, R. Raju, E. Pavitra and J. S. Yu, Cross-relaxation induced tunable emissions from the Tm^{3+}/Er^{3+}/Eu^{3+} ions activated $BaGd_2O_4$ nanoneedles, *Dalt. Trans.*, 2014, **43**, 9766–9776.

176 M. Ding, D. Chen, Z. Wan, Y. Zhou, J. Zhong, J. Xi and Z. Ji, Achieving efficient Tb^{3+} dual-mode luminescence via Gd-sublattice-mediated energy migration in a $NaGdF_4$ core-shell nanoarchitecture, *J. Mater. Chem. C*, 2015, **3**, 5372–5376.

177 L. Wang, X. Xue, H. Chen, D. Zhao and W. Qin, Unusual radiative transitions of Eu^{3+} ions in Yb/Er/Eu tri-doped $NaYF_4$ nanocrystals under infrared excitation, *Chem. Phys. Lett.*, 2010, **485**, 183–186.

178 Y. Wang, J. Li, Z. Zhu, Z. You, J. Xu and C. Tu, Impact of codopant ions on 2.5–3.0μm emission of Er^{3+}:$^4I_{11/2}\rightarrow{}^4I_{13/2}$ transition in Yb,Er,Eu:LaYSGG crystal, *J. Quant. Spectrosc. Radiat. Transf.*, 2015, **167**, 76–81.

179 A. Pandey, Sensitization Effect of Yb^{3+} in upconversion luminescence of Eu^{3+} codoped Y_2O_3 Phosphor, *J. Phys. Chem. Biophys.*, 2013, **3**, 3–5.

180 S. Mukherjee, V. Sudarsan, R. K. Vatsa and A. K. Tyagi, Luminescence studies on lanthanide ions (Eu^{3+}, Dy^{3+} and Tb^{3+}) doped YAG:Ce nano-phosphors, *J. Lumin.*, 2009, **129**, 69–72.

181 X. Li, Z. Yang, L. Guan, J. Guo, Y. Wang and Q. Guo, Synthesis and luminescent properties of $CaMoO_4$:Tb^3, R^+ (Li^+, Na^+, K^+), *J. Alloys Compd.*, 2009, **478**, 684–686.

182 S. Alahrach, J. Lambert, M. R. Suchomel, D. D. S. Meneses, G. Matzen, D. Massiot and V. Emmanuel, Crystallization of Y_2O_3–Al_2O_3 Rich Glasses: Synthesis of YAG Glass-Ceramics, *J. Phys. Chem. C*, 2011, **115**, 20499–20506.

183 R. S. Azis, D. Holland, M. E. Smith, A. Howes, M. Hashim, A. Zakaria, N. M. Saiden and M. K. Ikhwan, DTA / TG , XRD and ^{27}Al MAS NMR of

Yttrium Aluminium Garnet , $Y_3Al_5O_{12}$ by Sol-gel Synthesis, *J. Aust. Ceram. Soc. Vol.*, 2013, **49**, 74–80.

184 N. C. George, A. J. Pell, G. Dantelle, K. Page, A. Llobet, M. Balasubramanian, G. Pintacuda, B. F. Chmelka and R. Seshadri, Local environments of dilute activator ions in the solid-state lighting phosphor $Y_{3-x}Ce_xAl_5O_{12}$, *Chem. Mater.*, 2013, **25**, 3979–3995.

185 H. K. Dan, D. Zhou, Z. Yang, Z. Song, X. Yu and J. Qiu, Optimizing Nd/Er ratio for enhancement of broadband near-infrared emission and energy transfer in the Er^{3+}–Nd^{3+} co-doped transparent silicate glass-ceramics, *J. Non. Cryst. Solids*, 2015, **414**, 21–26.

186 C. Gaedtke, G. V. M. Williams, S. Janssens, S. Raymond and D. Clarke, Photoluminescence and radioluminescence study of Eu and Mn doped $RbMgF_3$ nanoparticles, *Radiat. Meas.*, 2013, **56**, 187–191.

187 F. Xin, S. Zhao, S. Xu, G. Jia, D. Deng, H. Wang and L. Huang, Preparation and photoluminescence of Eu-doped oxyfluoride borosilicate glass ceramics, *J. Rare Earths*, 2012, **30**, 6–9.

188 D. Chen, Y. Wang, Y. Yu and Z. Hu, Crystallization and fluorescence properties of Nd^{3+}-doped transparent oxyfluoride glass ceramics, *Mater. Sci. Eng. B Solid-State Mater. Adv. Technol.*, 2005, **123**, 1–6.

189 N. G. Boetti, D. Negro, J. Lousteau, F. S. Freyria, B. Bonelli, S. Abrate and D. Milanese, Spectroscopic investigation of Nd^{3+} single doped and Eu^{3+}/Nd^{3+} co-doped phosphate glass for solar pumped lasers, *J. Non. Cryst. Solids*, 2013, **377**, 100–104.

190 W. Y. Tian and B. R. Reddy, Energy transfer and upconversion studies in yttrium-aluminum-garnet crystal doped with thulium and holmium under near-infrared laser excitation, *J. Appl. Phys.*, 2000, **88**, 1221–1224.

191 B. Padlyak, W. Ryba-Romanowski, R. Lisiecki, V. Adamiv, Y. Burak, I. Teslyuk and A. Banaszak-Piechowska, Optical spectra and luminescence kinetics of the Sm^{3+} and Yb^{3+} centres in the lithium tetraborate glasses, *Opt. Appl.*, 2010, **40**, 427–438.

192 F. Johnson, H. Levanon, J. R. Norris and F. Johnson, Catalysis of the Cope and Claisen rearrangements, *Chem. Rev.*, 1970, **84**, 205–247.

193 J. P. Hurrell, S. P. S. Porto, I. F. Chang, S. S. Mitra and R. P. Bauman, Optical phonons of yttrium aluminum garnet, *Phys. Rev.*, 1968, **173**, 851–856.

194 M. Maczka, A. Bednarkiewicz, E. Mendoza-Mendoza, A. F. Fuentes and L. Kepinski, Low-temperature synthesis, phonon and luminescence properties of Eu doped $Y_3Al_5O_{12}$ (YAG) nanopowders, *Mater. Chem. Phys.*, 2014, **143**, 1039–1047.

195 D. Sun, Q. Zhang, S. Wan, H. Jiang and S. Yin, Study on the composite Nd:YAG crystal by laser micro-Raman spectroscopy, *Optoelectron. Lett.*, 2007, **3**, 441–443.

196 K. Papagelis, J. Arvanitidis, E. Vinga, D. Christofilos, G. A. Kourouklis, H. Kimura and S. Ves, Vibrational properties of $(Gd_{1-x}Y_x)_3Ga_5O_{12}$ solid solutions, *J. Appl. Phys.*, 2010, **107**, 1–8.

197 Q. Lu, Y. Wu, A. Li, Y. Wang, Y. Gao and H. Peng, Local thermal effect at luminescent spot on upconversion luminescence in Y2O3:Er^{3+}, Yb^{3+} nanoparticles, *Mater. Sci. Eng. B*, 2011, **176**, 1041–1046.

198 D. Dutczak, A. Kareiva and S. Sakirzanovas, Synthesis and Sm^{+}/Sm^{3+} doping effects on photoluminescence, *J. Lumin.*, 2011, **131**, 2255–2262.